The Pennsylvania State University

The Graduate School

Department of Engineering Science and Mechanics

COMPRESSION BEHAVIOR OF ULTRA-HIGH MODULUS CARBON/EPOXY COMPOSITES AND FRACTURE ENERGY CHARACTERIZATION OF INTERMEDIATE MODULUS CARBON/EPOXY COMPOSITES

A Thesis in

Engineering Mechanics

by

Michael Glath

Submitted in Partial Fulfillment
of the Requirements
for the Degree of

Master of Science

August 2014

The thesis of Michael Glath was reviewed and approved* by the following:

Kevin L. Koudela
Head of the Composite Materials Division, Applied Research Laboratory
Thesis Advisor

Charles E. Bakis
Distinguished Professor of Engineering Science and Mechanics

Judith A. Todd
P.B. Breneman Department Head of Engineering Science and Mechanics
Head of the Department of Engineering Science and Mechanics

*Signatures are on file in the Graduate School

ABSTRACT

Among compression test methods, ASTM D3410, SACMA SRM 1R-94, and ASTM D6641 are currently used to determine the compression modulus and compression strengths for ultra-high modulus (UHM, >350 GPa) composites. In this study, the compression modulus and compression strength of a proprietary ultra-high modulus carbon/epoxy composite were experimentally determined using SACMA SRM 1R-94 and ASTM D6641 for laminates with stacking sequences of $[(0/\pm60)_S]_2$ and $[(+60/0/-60)_S]_2$. The moduli of both laminates were experimentally shown to be statistically equivalent; the strength of the $[(0/\pm60)_S]_2$ laminate was shown to be significantly less than the $[(+60/0/-60)_S]_2$ laminate. A non-linear finite element model, using the commercial software package Abaqus, was developed for each compression test to predict the compression modulus and compression strength using the built-in damage progression algorithm in Abaqus. The models were used to identify failure modes for each compression test. Premature end-crushing was predicted at 2,200 με in the modeled modulus specimen of SACMA SRM 1R-94 for the $[(+60/0/-60)_S]_2$ laminate. End-crushing in the modeled SACMA SRM 1R-94 strength specimen was predicted to occur slightly after ultimate laminate failure for the $[(+60/0/-60)_S]_2$ laminate. End-crushing was predicted to be highly unlikely for both laminates in the ASTM D6641 model. The stress-strain response of both models matched relatively well with experimental data. The predicted strengths for both test methods were underpredicted for the $[(+60/0/-60)_S]_2$ laminate and overpredicted for the $[(0/\pm60)_S]_2$ laminate.

The fracture toughness of a proprietary intermediate modulus carbon/epoxy $[0]_{10}$ laminate was experimentally determined using ASTM D5528 and a U.S. Government provided end-notched flexure compliance calibration test method for modes I and II, respectively. Significant fiber bridging was noted for the ASTM D5528 experimental test specimens, especially at the crack tips. A finite element model was developed for each test method using the

virtual crack closure technique. A boundary was developed for the modeled load-displacement plot to encompass the experimental behavior of test specimens. This predicted boundary agreed well with mode I of ASTM D5528 experimental data. The predicted load-displacement response of mode II had a stiffer response than the experimental data, but the model did not consider potential stiffness degradation due to 5 preload calibrations used on each test specimen.

A statistical sensitivity analysis (ANOVA), based on the previously developed finite element model of ASTM D6641, was used to vary parameters assumed to influence the compression modulus, compression strength, and first ply failure of ASTM D6641. Of the chosen parameters, fiber misalignment was predicted to significantly affect the FEA-based results of the compression modulus, compression strength, and first ply failure for the chosen levels of variation. The laminate thickness, adhesive thickness, and enforced bolt displacement were predicted to not significantly affect the FEA-based results of the compression modulus, compression strength, and first ply failure for the chosen levels of variation.

TABLE OF CONTENTS

LIST OF FIGURES

LIST OF TABLES

ACKNOWLEDGEMENTS

I would like to thank my advisor, Dr. Kevin Koudela, for the opportunity to work on these projects and the assistance I received along the way. His practical approach to problem solving will help me to flourish throughout my career. His willingness to help me anytime his office door was open, even with his exceptionally busy schedule, made this work possible.

I would like to thank Mr. Eric Strauch for his exceptional feedback and detailed description of the experimental works presented throughout this investigation. Thank you to Dr. Al Segall for going out of his way to secure funding my first semester. Also, thank you to all the staff in the composite materials division of the Applied Research Lab at Penn State, especially Clark Moose, David Dreese, Dr. Thomas Juska, and Deborah Corl.

Finally, I would like to thank my mother, Sharon Glath, for her continuous support throughout graduate school and my career as well as my late father, James Glath Jr., for encouraging me to pursue engineering throughout my youth.

Chapter 1

Introduction

Background information is presented about standardized compression test methods and fracture toughness test methods in section 1.1. The objectives and scope of this investigation are defined in section 1.2. A literature review summarizing previously conducted studies on compression test methods, fracture toughness test methods, and design of experiments is presented in section 1.3.

1.1 Background

Section 1.1.1 introduces fiber classifications and material behavior described throughout this investigation. Section 1.1.2 presents lamina failure classifications and the criteria for failure types used in Chapters 2 and 4.

1.1.1 Material Characterization

Ultra-high modulus (UHM, > 600 GPa) carbon fibers and intermediate modulus (IM, ~300 GPa) carbon fibers have been developed to exploit the significant stiffness attributes they offer to polymer-matrix structural load bearing composites. The choice between fiber types for use in specific applications is based on a compromise between performance and cost [1]. Use of UHM carbon fibers has increased in a wide array of products such as sporting goods, marine, and aerospace applications [2]. Many of these applications are subject to in-plane compression loading as well as loading which induces delamination. As is widely known, the compression strength of carbon fiber composites can be considerably lower than the tensile strength. The

lower compression strength may be due in part to elastic microbuckling, fiber crushing, kink-band formation, and surface-ply buckling delamination, behaviors not manifest during tensile loading. Compression strength is also affected by matrix-related strengths that are dependent on initial defects which are dependent on the laminate stacking sequence. At the ply level, the thickness and the presence of neighboring plies can change the energy available for crack growth [3]. The presence of UHM or IM carbon fibers can amplify many of these effects due to both extreme differences in elastic properties between fibers and the surrounding polymer matrix as well as the increased anisotropy of the fiber itself. In addition, characterization test methods for UHM carbon fiber reinforced composites may need to be refined to assure accurate property determination. All lamina, laminate, and fracture energy data presented in this investigation were experimentally determined at the Applied Research Lab, unless otherwise specified.

1.1.2 Failure Theories

Macromechanical failure criteria are used in this investigation to capture various interactions of failure mechanisms. Daniel and Ishai [4] classify lamina failure theories into three groups:

1. *Limit or noninteractive theories*, in which specific failure modes are predicted by comparing individual lamina stresses or strains with corresponding strengths or ultimate strains, for example, maximum stress and maximum strain theories. No interaction among different stress components on failure is considered.
2. Interactive theories (e.g., the Tsai-Hill and Tsai-Wu theories), in which all stress components are included in one expression (failure criterion). Overall failure is predicted without reference to particular failure modes.
3. *Partially interactive or failure-mode-based theories* (e.g., the Hashin-Rotem and Puck theories), where separate criteria are given for fiber and interfiber (matrix or interface) failures.

Abaqus, the commercial finite element analysis (FEA) software package used throughout this investigation uses the two-dimensional (2-D) Hashin failure criteria in order to determine damage initiation and damage evolution in Chapter 2. The Hashin failure criteria are defined in equations (1-4):

Failure mode – fiber tension:

$$F_f^t = \left(\frac{\sigma_{11}}{S_{11}(T)}\right)^2 + \alpha\left(\frac{\tau_{12}}{S_{12}}\right)^2 \quad (1)$$

Failure mode – fiber compression:

$$F_f^c = \left(\frac{\sigma_{11}}{S_{11}(C)}\right)^2 \quad (2)$$

Failure mode – matrix tension:

$$F_m^t = \left(\frac{\sigma_{22}}{S_{22}(T)}\right)^2 + \left(\frac{\tau_{12}}{S_{12}}\right)^2 \quad (3)$$

Failure mode – matrix compression:

$$F_f^c = \left(\frac{\sigma_{22}}{S_{23}}\right)^2 + \left[\left(\frac{S_{22}(C)}{S_{23}}\right)^2 - 1\right]\frac{\sigma_{22}}{S_{22}(C)} + \left(\frac{\tau_{12}}{S_{12}}\right)^2 \quad (4)$$

where,

S_{11} *(T):*	longitudinal tensile strength
S_{11} *(C):*	longitudinal compressive strength
S_{22} *(T):*	transverse tensile strength
S_{22} *(C)*	transverse compressive strength
S_{12}*:*	longitudinal shear strength
S_{23}*:*	transverse shear strength
α*:*	Coefficient between 0 and 1
σ_{11}	stress along the 11 – direction
σ_{22}	stress along the 22 – direction
τ_{12}	stress along the 1-2 plane [5, 6]

The Tsai-Wu (An interactive theory) failure criteria are defined in equation (5) with sub-definitions listed in equations (6-11) [7]:

$$F = F_1\sigma_{11} + F_2\sigma_{22} + F_{11}\sigma_{11}^2 + F_{22}\sigma_{22}^2 + F_{66}\sigma_{12}^2 + 2F_{12}\sigma_{11}\sigma_{22} \quad (5)$$

where,

$$F_1 = \frac{1}{S_{11}(T)} + \frac{1}{S_{11}(C)} \tag{6}$$

$$F_2 = \frac{1}{S_{22}(T)} + \frac{1}{S_{22}(C)} \tag{7}$$

$$F_{11} = \frac{-1}{S_{11}(T)S_{11}(C)} \tag{8}$$

$$F_{22} = \frac{-1}{S_{22}(T)S_{22}(C)} \tag{9}$$

$$F_{66} = \frac{1}{S_{12}^2} \tag{10}$$

$$F_{12} = \dot{f}\sqrt{F_{11}F_{22}} \tag{11}$$

where -1.0 ≤ $\dot{f}$ ≤ 1.0.

"According to the maximum strain theory (A limit theory), failure occurs when at least one of the strain components along the principal material axes exceeds the corresponding ultimate material strain in that direction. This theory allows for some interaction of stress components due to Poisson's ratio effects. It is expressed in the form of the following subcriteria [4]":

$$\varepsilon_{11} = \begin{cases} \varepsilon_{11}^u(T)\ when\ \varepsilon_{11} > 0 \\ \varepsilon_{11}^u(C)\ when\ \varepsilon_{11} < 0 \end{cases} \tag{12}$$

$$\varepsilon_{22} = \begin{cases} \varepsilon_{22}^u(T)\ when\ \varepsilon_{22} > 0 \\ \varepsilon_{22}^u(C)\ when\ \varepsilon_{22} < 0 \end{cases} \tag{13}$$

$$\varepsilon_{33} = \begin{cases} \varepsilon_{33}^u(T)\ when\ \varepsilon_{33} > 0 \\ \varepsilon_{33}^u(C)\ when\ \varepsilon_{33} < 0 \end{cases} \tag{14}$$

$$|\gamma_{12}| = \gamma_{12}^u \tag{15}$$

$$|\gamma_{13}| = \gamma_{13}^u \tag{16}$$

$$|\gamma_{23}| = \gamma_{23}^u \tag{17}$$

where,

$\epsilon_{11}^{u}(T)$, $\epsilon_{22}^{u}(T)$, $\epsilon_{33}^{u}(T)$:	ultimate tensile strains along principal material axes
$\epsilon_{11}^{u}(C)$, $\epsilon_{22}^{u}(C)$, $\epsilon_{33}^{u}(C)$:	ultimate compressive strains along the principal material axes
γ_{12}^{u}, γ_{13}^{u}, γ_{23}^{u}	ultimate shear strains on principal material planes
ε_{11}, ε_{22}, ε_{33}, γ_{12}, γ_{13}, γ_{23}:	strain components along the principal material axes and planes

Further background information is provided in each chapter to adequately prepare the reader for the investigated topics.

1.2 Literature Review

A brief literature review summarizing previously performed studies on compression test methods, fracture toughness test methods, and design of experiments is presented in sections 1.2.1, 1.2.2, and 1.2.3, respectively.

1.2.1 Compression Test Methods

Currently, there exists no universally accepted compression testing method within the U.S. composites community [8]. Many researchers use the ASTM D3410, SACMA SRM 1R-94, or the newer ASTM D6641 method [9]. These test methods transfer compression load to the specimen via shear, end load or a combination of both. Using a finite element model, Xie and Adams found that shear loading has the greatest stress concentration at the tab end of the test specimen (at the gage section), while end loading has the greatest stress concentration at the loading end of the specimen. The combined loading method has been shown to reduce the stress concentration at both the tab end and the loading end of the specimen relative to the shear and end loading methods [10].

In regard to the Suppliers of Advanced Composite Materials Association (SACMA), Adams wrote [11]:

> While several consortia have been formed over the years, the Suppliers of Advanced Composite Materials Assn. (SACMA) gained particular prominence. SACMA issued its first set of SRMs (SACMA Recommended Methods) in 1988, written in a style similar to ASTM standards. SACMA deliberately called them Recommended Methods in the hope that ASTM would adopt them as ASTM standards. SACMA was relatively small, with perhaps only one or, at most, a few "experts" available to write a particular standard. Thus, the task could be done quickly.
>
> Although SACMA disbanded in 2000 (due, in part, to a particularly difficult downturn in the aerospace industry), other consortia remain.

SACMA SRM 1R-94's methods are not currently maintained. Therefore, referencing this specification should be done with care [12].

Joyce et al. [13] conducted a FEA study on ASTM D6641 and found thin, tapered tabs had the smallest stress concentrations at the tab tip and should output higher measured compressive strengths since premature failure at the tab tip is less likely to occur. Adams [14] examined fiber-reinforced composite compression specimens with and without tabs. Adams concluded:

> ...that the use of conventional tabs on compression specimens is not an acceptable approach to attaining design values for high axial compressive strength composites. The tabs always introduce detrimental stress concentrations. Correspondingly, the use of wedge grips is not desirable. They introduce through-thickness stresses, and local stress concentrations at the grip ends. End loading of an untabbed specimen cannot be performed because of end crushing.

ASTM D3410 is the test standard that uses wedge grips referenced in the previous quotation. ASTM D3410 is a compression test method used to determine in-plane compressive properties of polymer matrix composite materials reinforced by high-modulus fibers. The main characteristic that differentiates ASTM D3410 from SACMA SRM 1R-94 and ASTM D6641 is that a compressive force is applied through the specimen by way of shear at the wedge grip interfaces [15]. Figure 1-1 shows the ASTM D3410 test fixture with its respective tabbed specimen. A

variable gage length of 0.5-1.0 in is noted in the gage section of the ASTM D3410 tabbed specimen.

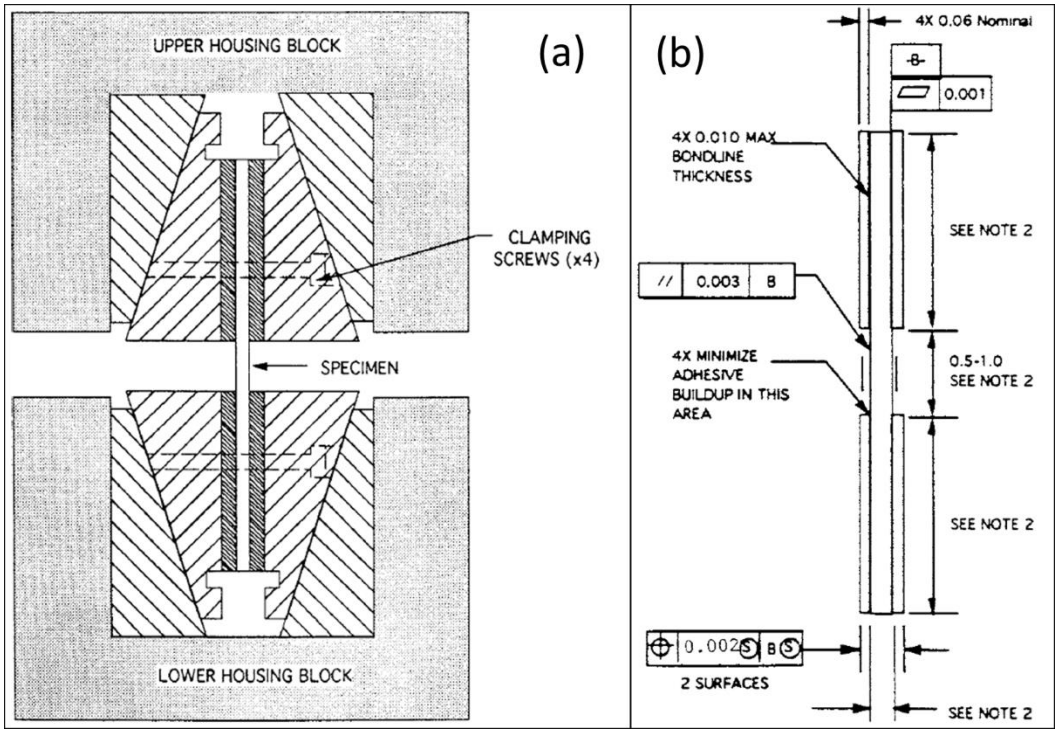

Figure 1-1: ASTM D3410 (a) test fixture and (b) tabbed test specimen [15]

On a comparative basis, measured compression strengths from SACMA SRM 1R-94 are typically higher than for the methods of ASTM D3410. This is believed to be due to the short and narrow gage length of the SACMA SRM 1R-94 specimen, and to the effect this geometry has in suppressing failure mechanisms that are present in longer, unsupported gage lengths such as in ASTM D3410 procedures A and B [12]. To the author's knowledge, limited studies exist which further use FEA to examine SACMA SRM 1R-94 and ASTM D6641.

1.2.2 Fracture Toughness Test Methods

Interlaminar fracture toughness can be used to develop delamination failure criteria for composite damage tolerance and durability analysis [16]. Fracture toughness, defined in Chapter 3, can be measured for modes I, II, and III. Mode I fracture toughness is most commonly measured by ASTM D5528. Mode II fracture toughness is most commonly measured by an end-notched flexure test making use of a three-point or four-point bending configuration. Mixed-mode fracture toughness, which examines modes I and II fracture toughness, can be determined using the standard test method ASTM D6671. Various test methods such as an edge-cracked torsion test or a doubly split cantilever beam test have been proposed to measure mode III fracture toughness [4].

The simulation of delamination using FEA is typically accomplished by using the virtual crack closure technique (VCCT) or cohesive finite elements [17]. VCCT requires the path of the modeled crack to be defined before the simulation whereas cohesive finite elements do not. However, the use of cohesive elements encounters numerical difficulties in properly defining the mesh-dependent stiffness and strength values. Turon et al. [17] developed a closed-form expression to define the stiffness of a cohesive layer, allowing the use of coarser meshes using cohesive elements; they also developed an expression to adjust the maximum interfacial strength such that the cohesive zone spans more elements.

A large amount of literature exists examining the delamination behavior of the VCCT and cohesive zone models. Xie and Waas modeled modes I and II delamination using a discrete cohesive zone model benchmarked against a VCCT model [18]. Camanho et al. [19] modeled mode I, mode II, and mixed mode fracture test methods using cohesive elements with relatively good agreement to experimental data. Bonhomme et al. [20] used the VCCT method to

determine the strain energy release rate for mode I compared to experimentally determined values.

1.2.3 Design of Experiments

"*Robust Design* is an engineering methodology for improving productivity during research and development so that high-quality products can be produced quickly and at low cost [21]." *Robust Design* makes use of orthogonal arrays in order to design physically-based or numerically-based experiments which study many design parameters simultaneously.

Grujicic et al. [22] used a physically-based experimental orthogonal array approach to determine the dependence of several parameters on the predicted electrical response of polymer electrolyte membrane fuel cells. In addition, Grujicic et al. [23] used a transient non-linear dynamics analysis (A numerically-based approach) to investigate the uncertainty of material model parameters for a hybrid carbon-nanotube/E-glass reinforced poly-vinyl-ester-epoxy-matrix composite armor. Dar et al. [24] used an orthogonal array approach to vary parameters in a FEA model to determine the sensitivity of input parameters on a model similar to an orthopaedic fixation plate. A collection of orthogonal array configurations used to carry out robust design experiments can be found in [21].

Other studies exist that use a combination of probabilistic and FEA approaches [25]; however, to the author's knowledge, no studies have exploited the orthogonal array approach to examine parameters of interest for compression test fixtures.

1.3 Research Objectives and Scope

The objectives of the current investigation are listed below:

- Experimentally determine the compression modulus and compression strength of two proprietary UHM laminates, $[(0/\pm60)_S]_2$ and $[(+60/0/-60)_S]_2$, using SACMA SRM 1R-94 and ASTM D6641. See Chapter 2.

- Construct a FEA model for each compression test method which accurately predicts the compression modulus and compression strength of the UHM laminates. The models are used to identify Hashin failure modes in each test standard. This is achieved by using Hashin failure criteria and damage evolution capabilities described in Section 2.2 of this investigation. See Chapter 2.

- Experimentally determine the fracture toughness for mode I and mode II of a proprietary $[0]_{10}$ IM carbon/epoxy laminate using ASTM D5528 and a U.S. Government provided end-notched flexure (ENF) compliance calibration test method. See Chapter 3.

- Construct a FEA model for each fracture toughness test method which accurately predicts the load-displacement plots of the experimental data. See Chapter 3.

- Create a computational design of experiments matrix populated with factors suspected to most influence the compression modulus, compression strength, and first ply failure of ASTM D6641. The finite element model developed for ASTM D6641 is used to carry out the numerical experiments. See Chapter 4.

Chapter 2

Experimental and Computational Procedures for Compression Test Methods

In this chapter experimental and computational procedures for compression testing are discussed in Sections 2.1 and 2.2, respectively. Section 2.1 summarizes SACMA SRM 1R-94 and ASTM D6641 test methods used to measure the compressive modulus and compressive strength of a laminate. Section 2.2 summarizes finite element analysis techniques used to model the compressive modulus and compressive strength of SACMA SRM 1R-94 and ASTM D6641. Section 2.3 compares and contrasts the experimental and computational results of the laminates investigated using SACMA SRM 1R-94 and ASTM D6641.

2.1 Test Methods – SACMA SRM 1R-94 and ASTM D6641

Test and data reduction methods are discussed in Sections 2.1.1 and 2.1.2, respectively.

2.1.1 Test Methods

Compression tests were conducted on an ultra-high-modulus (UHM) carbon fiber/epoxy composite. The modulus of the carbon fiber is reported by the manufacturer to be between 71-78 Msi (490 – 540 GPa). The fiber diameter is nominally 4.4 μm and the density is 1.92 g/cc. The specific material system investigated for this research is proprietary so resin formulations and UHM fiber type are not presented. The laminates investigated in this study were fabricated from uni-directional plies with the following ply orientations: $[(0/\pm60)_S]_2$ and $[(+60/0/-60)_S]_2$. The

rationale for the different quasi-isotropic layups is to assess the effects of laminate outer ply orientation on compression behavior.

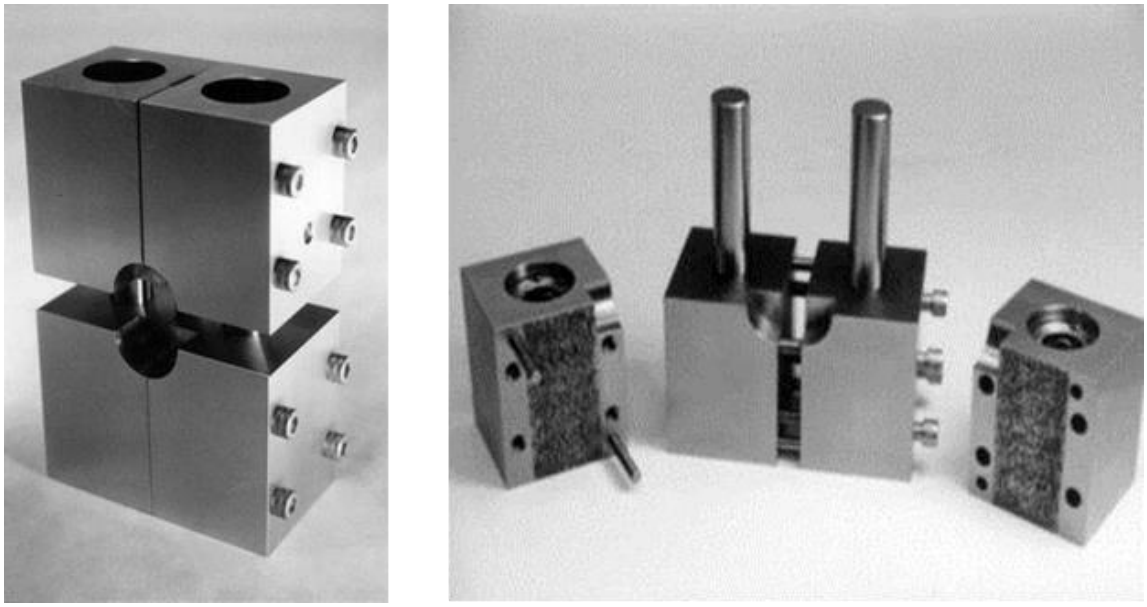

Figure 2-1: ASTM D6641 combined loading compression test fixture [26]

Figure 2-2: SACMA SRM 1R-94 end-loaded compression test fixture [26]

The compression test methods employed include ASTM D6641, Figure 2-1, and SACMA SRM 1R-94, Figure 2-2. The former method includes a fixture that allows for a combination of both shear loading along the sides of the test specimen (with or without bonded tabs) as well as end loading on the specimen. The percentage of shear loading is controlled to some degree by the fixture bolt torque. The bolts are shown holding the fixture blocks together in Figure 2-1. Increasing the bolt torque imparts a higher pressure load on the faces of the specimen which results in an increased level of the shear load contribution to the total in-plane compressive load in the specimen's gage section.

For all ASTM D6641 specimens tested herein, a fixture bolt torque of 25 in-lb (2.82 N-m) is used. The specification suggests a torque range of 22.1 – 26.6 in-lb (2.5 – 3.0 N-m). The typical ASTM D6641 specimen length is 5.5 in (14 cm). The width is variable provided an

acceptable failure mode is produced. For this study, a specimen width of 0.5 in (1.3 cm) is utilized.

Through past work, it was found that acceptable failure modes were consistently generated for tabbed carbon composite specimens [27]. Acceptable and unacceptable failure modes for ASTM D6641 are presented in Figure 2-3. The three letter failure mode description for both acceptable and unacceptable failures can be extracted using the three-part identification codes and schematics shown in Figure 2-3. An example of an acceptable failure mode is a through-thickness failure starting at the top of the gage section near the tab; the third specimen to the right in Figure 2-3 exhibits this failure mode. An example of an unacceptable failure mode is end-crushing at the top of the laminate; the seventh specimen to the right in Figure 2-3 exhibits this failure mode. Tabs used herein are fabricated from a $[0/45]_S$ standard-modulus 5HS carbon fabric and epoxy resin. Tab thickness is nominally 0.09 – 0.10 in (2.3 – 2.5 mm). The tabs are bonded to the specimens using Hysol EA 9394 two-part epoxy paste adhesive which is allowed to cure for a minimum of 48 hours at room temperature prior to testing.

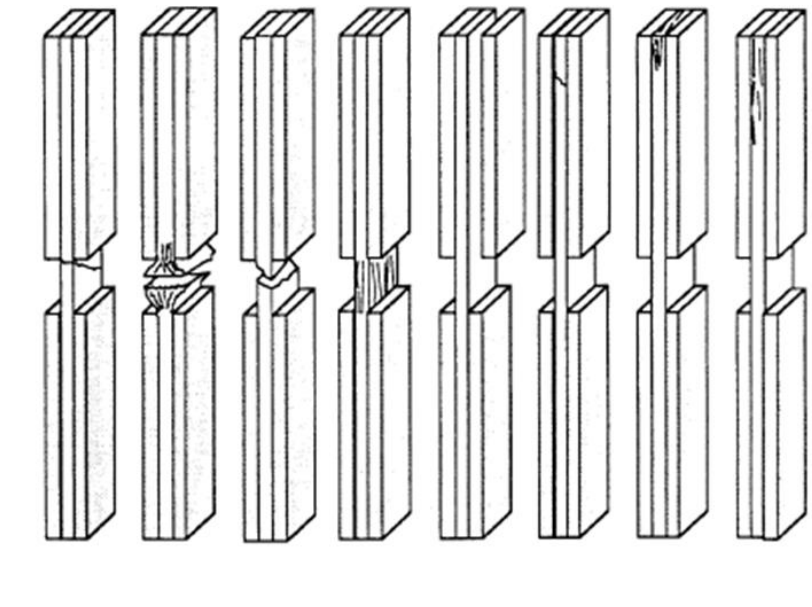

First Character

Failure Mode	Code
Angled	A
Brooming	B
end-Crushing	C
Delamination	D
Euler buckling	E
tHrough-thickness	H
Kink bands	K
Lateral	L
Multi-mode	M(xyz)
long.-Splitting	S
Transverse shear	T
eXplosive	X
Other	O

Second Character

Failure Area	Code
Inside grip/tab	I
At grip/tab	A
Gage	G
Multiple Areas	M
Tab adhesive	T
Various	V
Unknown	U

Third Character

Failure Location	Code
Bottom	B
Top	T
Left	L
Right	R
Middle	M
Various	V
Unknown	U

Figure 2-3: Compression test specimen three-part failure identification codes and overall specimen failure schematics [28]

The SACMA SRM 1R-94 method utilizes a fixture, as shown in Figure 2-2, which supports the faces of the specimen and restricts buckling and out-of-plane deformation [29]. The bolt torque is kept to a minimum 5 in-lb (0.56 N-m) and side support plates are grooved to help keep frictional contact at a minimum. This fixture is designed for end-load application only. As such, the method requires two specimens, one for strength which includes a small open gage section of 0.18 in (4.8 mm), and another specimen for modulus measurement, which includes no tabs and incorporates support faces with a "cut-out" allowing room for strain gages and wiring.

Test specimen dimensions for both SACMA SRM 1R-94 and ASTM D6641 methods are shown in Figure 2-4. The modulus specimen for SACMA SRM 1R-94 is identical to the strength specimen shown in Figure 2-4 (a) but without tabs, where the locations of the tabs are shown as the hatched area of the specimens in Figure 2-4. The effective gage section of the SACMA modulus specimen is 0.5 in (12.7 mm) as defined by the 12.7 mm "cut-out" in the modulus support faces.

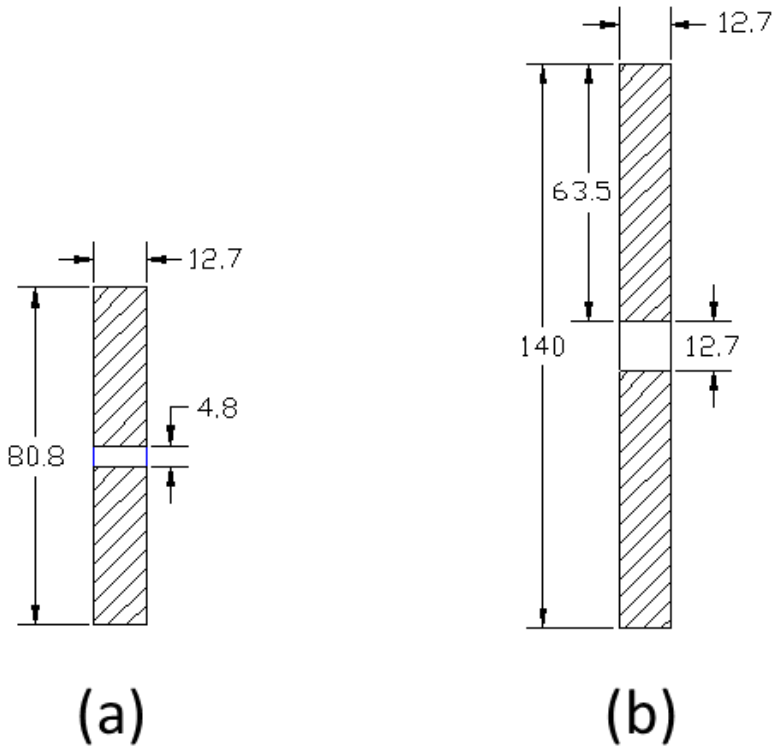

Figure 2-4: (a) SACMA SRM 1R-94 compressive strength specimen [29], (b) ASTM D6641 specimen [28]. Dimensions shown have units in mm

For the SACMA SRM 1R-94 compressive strength specimen, the strain at failure is not available because the gage region of the strength specimen is not large enough for a strain gage, and the modulus specimen geometry is not suitable for loading to failure. Consequently, stress-

strain response, including monitoring of coupon bending strains as commonly done to assess proper gage section loading, cannot be observed over most of the stress-strain curve [12].

Strain gages are used to measure gage section strains for subsequent elastic modulus calculations. Vishay MicroMeasurements' CEA-06-062UW-350 strain gages with a gage factor of 2.06 are used for all specimens tested herein. All specimens are instrumented with these gages on gage section front and back faces to monitor gage section bending. The compressive strain used in subsequent moduli calculations is the average of the front and back face strain at the given stress. Specimens are tested in an Instron 5584 electromechanical test frame utilizing Instron's Bluehill control and data acquisition software. All tests are conducted at a cross-head speed of 0.05 in/min. Due to the low strain capability of the material coupled with the propensity for the SACMA modulus specimen to crack at the loading ends, elastic moduli are calculated via a linear least squares fit, as opposed to the commonly used secant method for calculating the moduli, of the stress versus strain data between strain limits of 0.025% – 0.2% (250 – 2000 με) instead of the more commonly used limits of 0.1% - 0.3% (1000 – 3000 με).

2.1.2 Data Reduction Method for Analysis Comparison

Test results for the two angle-ply laminates are presented in Table 2-1. Moduli measured from both tests are statistically equivalent for the two angle ply lamina. Measured strengths are significantly less for the $[(0/\pm60)_s]_2$ laminate than the $[(+60/0/-60)_s]_2$ laminate. All failure modes of the tested laminates were determined to be acceptable. Using the failure identification codes shown in Figure 2-3, for the $[(0/\pm60)_s]_2$ laminate, several specimens incurred visible cracking in the gage section and another specimen incurred TAT. For the ASTM D6641 $[(+60/0/60)_s]_2$ laminates, specimens incurred failure combinations of BAB and HAB, HGM and BGM, TGM and HAB, and a case of HAT in the 0° plies. Six $[(0/\pm60)_s]_2$ and six $[(0/\pm60)_s]_2$ laminates were

tested using ASTM D6641 and SACMA SRM 1R-94. For the SACMA SRM 1R-94 $[(+60/0/60)_s]_2$ laminates, a specimen incurred a combination of HAM and TIB.

Table 2-1: Compression test results with average and standard deviation results

UHM Laminate	Test Method	Average Compression Strength (ksi), Standard Deviation (ksi)	Average Compression Modulus from 0.025-0.2% ε (Msi), Standard Deviation (Msi)	Average Strain at Max Stress (%), Standard Deviation (%)
$[(0/\pm60)_s]_2$	SACMA SRM 1R-94	-----	14.3, 0.9	-----
	ASTM D6641	39.8, 3.5	13.8, 0.4	0.29, 0.03
$[(+60/0/-60)_s]_2$	SACMA SRM 1R-94	60.4, 2.6	14.7, 0.6	0.44, 0.02
	ASTM D6641	54.0, 1.04	14.2, 0.3	0.42, 0.02

2.2 Computational Procedures – Finite Element Analysis

Finite element analyses are performed for both SACMA SRM 1R-94 and ASTM D6641 to examine the differences between predicted and measured compression moduli and strength. Residual stresses were neglected since the cure cycle was not available. Constructing an accurate finite element model offers the ability to vary parameters within the model to determine the controlling features (e.g. bolt torque or adhesive thickness [30]) of a test method without costly testing so the experimental processes can be improved by focusing on the governing test method features. Governing test method features are further investigated in Chapter 4 that describes a design of experiments approach for numerical simulations. Section 2.2.1 defines the material properties used for all finite element analyses. Section 2.2.2 provides a brief overview of the

Hashin failure initiation and damage evolution methodology. Section 2.2.3 describes the SACMA SRM 1R-94 compression modulus modeling methodology and results. Section 2.2.4 describes the modeling methodology and results of ASTM D6641. Section 2.2.5 applies the same techniques from Section 2.2.4 to the strength specimen of SACMA SRM 1R-94. Section 2.2.6 discusses classical laminate theory and its application and limitations to the two laminates defined in Table 2-2.

2.2.1 Material Properties

Two laminates, $[(0/\pm60)_s]_2$ and $[(+60/0/60)_s]_2$, were investigated using Abaqus. A one-eighth symmetry model, analogous to a model developed by Lapczyk and Hurtado [31], was constructed in order to minimize required computational resources. The average elastic lamina properties and strengths of the UHM carbon/epoxy system used in the analyses are listed in Table 2-2:

Table 2-2: Material properties of test specimen parts

Laminate Stacking Sequences: $[(0/\pm60)_s]_2$ and $[(+60/0/60)_s]_2$		
Average Elastic Properties		
UHM Carbon/Epoxy Lamina Properties	**Carbon Tab Lamina Properties**	**Hysol EA 9394 Isotropic Properties**
E_{11} = 40.39 Msi	E_{11} = 5 Msi	$E\ (T)$ = 0.426 Msi
E_{22} = 0.922 Msi	E_{22} = 5 Msi	G = 0.151 Msi
E_{33} = 0.922 Msi	E_{33} = 1 Msi	v = 0.41
v_{12} = 0.303	v_{12} = 0.09	
v_{13} = 0.303	v_{13} = 0.09	
v_{23} = 0.303	v_{23} = 0.09	
G_{12} = 0.818 Msi	G_{12} = 0.8 Msi	
G_{13} = 0.764 Msi	G_{13} = 0.8 Msi	
G_{23} = 0.295 Msi	G_{23} = 0.5 Msi	
Failure Strength Properties		**Strength Properties**
$S_{11}\ (T)$ = 268 ksi		$S\ (T)$ = 7.5 ksi
$S_{11}\ (C)$ = 131.8 ksi		$S\ (G)$ = 4.4 ksi
$S_{22}\ (T)$ = 2.8 ksi		
$S_{22}\ (C)$ = 30.02 ksi		
S_{12} = 10.99 ksi		
S_{23} = 2.8 ksi		
Failure Strain Properties		
$\varepsilon_{11}^{u}(T)$ = 6.64 x 10^{-3} in/in		
$\varepsilon_{11}^{u}(C)$ = 3.26 x 10^{-3} in/in		
$\varepsilon_{22}^{u}(T)$ = 3.04 x 10^{-3} in/in		
$\varepsilon_{22}^{u}(C)$= 3.26 x 10^{-2} in/in		
γ_{12}^{u} = 1.34 x 10^{-2} in/in		

where,

E_{11}, E_{22}, E_{33}:	young's moduli along the principal material axes
v_{12}, v_{13}, v_{23}:	Poisson's ratios along the principal material planes
G_{12}, G_{13}, G_{23}:	shear moduli along the principal material planes
E (T):	isotropic tensile modulus
G:	isotropic shear modulus
S (T):	isotropic tensile strength

S (G): isotropic shear strength

The average of G_{12} and G_{13} (0.791 Msi) were used for both G_{12} and G_{13} in the finite element models.

2.2.2 Hashin Failure Modeling and Viscous Regularization Methodology

Abaqus' built-in algorithms for Hashin failure and damage evolution modes were used for SACMA SRM 1R-94 and ASTM D6641 coupon strength predictions. In Section 2.2.2.1, a brief description of the Abaqus failure model is provided. Section 2.2.2.2 discusses the viscous regularization strategy adopted to ensure adequate solution convergence.

2.2.2.1 Hashin 2-D Failure Modeling

For this investigation, the correlation coefficient alpha for fiber tension failure calculation was set equal to one, which uses Hashin's 1980 failure model [5] as opposed to the 1973 model, in which case alpha would be set equal to zero [6]; however, the fibers are in compression, making the selection of alpha extraneous to this investigation. The UHM failure strains were extrapolated from the failure strengths using the formula:

$$\varepsilon^u = \frac{S}{E} \tag{18}$$

where,

ε^u: respective ultimate tensile or compressive strains along 11 and 22 axes and 12 plane

S: respective ultimate tensile or compressive strengths along 11 and 22 axes and 12 plane

E: respective elastic moduli along 11 and 22 axes and 12 plane

Hashin 2-D failure criteria with damage evolution was utilized in Abaqus. Damage initiation refers to the onset of degradation at a material point. In Abaqus, the damage initiation criteria for fiber-reinforced composites are based on Hashin's theory. A value of 1.0 or greater indicates initiation criteria have been met [32]. See equations (1-4) for initiation criteria.

A stress tensor is used to evaluate damage initiation criteria:

$$\hat{\sigma} = M\sigma \tag{19}$$

where,

$\hat{\sigma}$: effective (i.e. at the current damage state) stress tensor with components $\hat{\sigma}_{11}$, $\hat{\sigma}_{22}$, and $\hat{\tau}_{12}$

σ: true stress

M: damage operator:

$$M = \begin{bmatrix} \frac{1}{(1-d_f)} & 0 & 0 \\ 0 & \frac{1}{(1-d_m)} & 0 \\ 0 & 0 & \frac{1}{(1-d_s)} \end{bmatrix} \tag{20}$$

d_f, d_m, d_s: internal damage variables that characterize fiber, matrix, and shear damage, which are derived from damage variables d_f^t, d_f^c, d_m^t, and d_m^c, corresponding to the four failure modes in equations (1-4)

where,

$$d_f = \begin{cases} d_f^t \; if \; \hat{\sigma}_{11} \geq 0 \\ d_f^c \; if \; \hat{\sigma}_{11} < 0 \end{cases} \tag{21}$$

$$d_m = \begin{cases} d_m^t \; if \; \hat{\sigma}_{22} \geq 0 \\ d_m^c \; if \; \hat{\sigma}_{22} < 0 \end{cases} \tag{22}$$

$$d_s = 1 - \left(1 - d_f^t\right)\left(1 - d_f^c\right)(1 - d_m^t)(1 - d_m^c) \tag{23}$$

Prior to any damage initiation and evolution, the damage operator, M, is equal to the identity matrix [32].

The use of the damage evolution feature within Abaqus requires specific fracture energy types. Camanho [33] explains that a test standard exists for the matrix tension input, ASTM D5528. The values for tensile and compressive fiber fracture can be obtained from compact tension (CT) and compact compression (CC) tests as proposed by Pinho et al. [34]. Matrix compression fracture energy can be obtained from mode II end-notched flexure tests (ENF) and a formulation for $G_{mc,c}$ specified in [35]. $G_{mc,c}$ is the transverse compressive fracture energy and according to this formulation, the value depends on the laminate stacking configuration.

Furthermore, Camanho's formulation defined in [35] is given as:

$$G_{mc,c} \approx \frac{G_{II}}{\cos\alpha_0} + at\eta^T S_{22}(C)\cos\alpha_0 \qquad (24)$$

where,

G_{II}: interlaminar fracture toughness for mode II
α_0: fracture angle, where $\alpha_0 = 53 \pm 3^o$
a: adjustment parameter between 0 (in an unidirectional laminate) and 1 (in a strongly confined lamina)
η^T: term accounting for friction between the crack faces

The mean of α_0 was used to calculate $G_{mc,c}$. The fracture energies for standard double-cantilever beam and end-notched flexure test specimens were experimentally determined for the UHM carbon/epoxy system. The value of "a" in equation (24) was set equal to zero, since a unidirectional laminate was used to determine G_{II}. The damage evolution properties used for the two laminates investigated are listed in Table 2-3:

Table 2-3: Damage evolution properties

Damage Evolution Properties			
$\boldsymbol{G_{ft,c}}\left(\frac{in\ lb}{in^2}\right)$	$\boldsymbol{G_{fc,c}}\left(\frac{in\ lb}{in^2}\right)$	$\boldsymbol{G_{mt,c}}\left(\frac{in\ lb}{in^2}\right)$	$\boldsymbol{G_{mc,c}}\left(\frac{in\ lb}{in^2}\right)$
523	456	0.850	4.199

where,

$G_{ft,c}$: longitudinal tensile fracture energy ($\frac{in\ lb}{in^2}$)
$G_{fc,c}$: longitudinal compressive fracture energy ($\frac{in\ lb}{in^2}$)
$G_{mt,c}$: transverse tensile fracture energy ($\frac{in\ lb}{in^2}$)
$G_{mc,c}$: transverse compressive fracture energy ($\frac{in\ lb}{in^2}$).

To the author's knowledge, there is no reference data for $G_{ft,c}$ and $G_{fc,c}$ for the UHM carbon/epoxy system available in open literature. However, Pinho et al. [36] determined values for $G_{ft,c}$ and $G_{fc,c}$ for a T300/913 carbon-epoxy laminated composite using compact tension and compact compression tests. $G_{ft,c}$ and $G_{fc,c}$ from the T300/913 carbon-epoxy laminated composite were assumed equal to the UHM carbon/epoxy composite for these computations.

After damage initiation, the damage evolution material softening response is given by:

$$\sigma = C_d \varepsilon \tag{25}$$

where ε is the strain and C_d is the damaged elasticity matrix given by:

$$C_d = \frac{1}{D}\begin{bmatrix} (1-d_f)E_1 & (1-d_f)(1-d_m)\nu_{21}E_1 & 0 \\ (1-d_f)(1-d_m)\nu_{12}E_2 & (1-d_m)E_2 & 0 \\ 0 & 0 & (1-d_s)GD \end{bmatrix} \tag{26}$$

where,

$$D = 1-(1-d_f)(1-d_m)\nu_{12}\nu_{21} \tag{27}$$

The damage variable will evolve such that the stress-displacement behaves as shown in Figure 2-5 for each of the four failure modes listed in equations (1-4). The positive slope of the stress-displacement curve prior to damage initiation corresponds to linear elastic material behavior; the negative slope after damage is achieved by evolution of the respective damage variables according to the equations (28-35) [32].

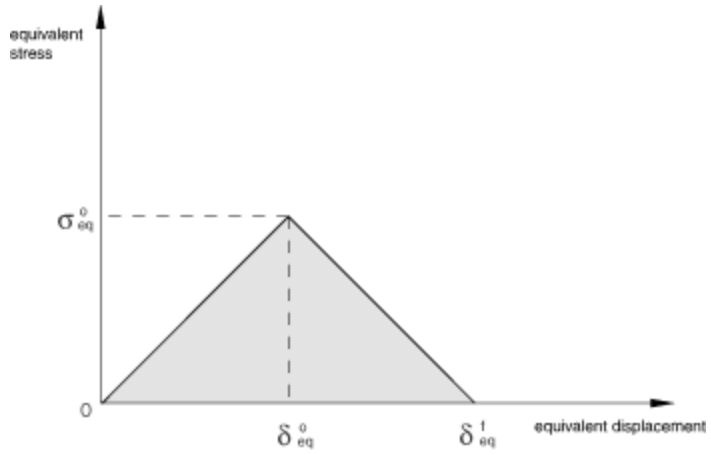

Figure 2-5: Generalized equivalent stress versus equivalent displacement [32]

The equivalent damage using the Hashin failure model for each of the four damage modes are defined as follows:

Fiber tension ($\hat{\sigma}_{11} \geq 0$):

$$\delta_{eq}^{ft} = L^c \sqrt{\langle \varepsilon_{11} \rangle + \alpha \varepsilon_{12}^2} \tag{28}$$

$$\sigma_{eq}^{ft} = \frac{\langle \sigma_{11} \rangle \langle \varepsilon_{11} + \alpha \tau_{12} \varepsilon_{12} \rangle}{\frac{\delta_{eq}^{ft}}{L^c}} \tag{29}$$

Fiber compression ($\hat{\sigma}_{11} < 0$):

$$\delta_{eq}^{fc} = L^c \langle -\varepsilon_{11} \rangle \tag{30}$$

$$\sigma_{eq}^{fc} = \frac{\langle -\sigma_{11} \rangle \langle -\varepsilon_{11} \rangle}{\frac{\delta_{eq}^{fc}}{L^c}} \tag{31}$$

Matrix tension ($\hat{\sigma}_{22} \geq 0$):

$$\delta_{eq}^{mt} = L^c \sqrt{\langle \varepsilon_{22} \rangle + \varepsilon_{12}^2} \tag{32}$$

$$\sigma_{eq}^{mt} = \frac{\langle \sigma_{22} \rangle \langle \varepsilon_{22} + \tau_{12} \varepsilon_{12} \rangle}{\frac{\delta_{eq}^{mt}}{L^c}} \tag{33}$$

Matrix compression ($\hat{\sigma}_{22} < 0$):

$$\delta_{eq}^{mc} = L^c \sqrt{\langle -\varepsilon_{22} \rangle + \varepsilon_{12}^2} \tag{34}$$

$$\sigma_{eq}^{mc} = \frac{\langle -\sigma_{22} \rangle \langle -\varepsilon_{22} + \tau_{12} \varepsilon_{12} \rangle}{\frac{\delta_{eq}^{mc}}{L^c}} \tag{35}$$

where L_c is the characteristic length, based on the element geometry and formulation. For a first order element, it is the length of a line across that element and is half of the same length for a second order element. For membranes and shells, with shells being the main element of choice in this investigation, it is a characteristic length in the reference surface, computed as the square root of the area. The symbol $\langle \quad \rangle$ in equations (28-35) represents the Macaulay bracket operator, which is defined for every $n \in \mathbb{R}$:

$$\langle n \rangle = \frac{(n + |n|)}{2} \tag{36}$$

After damage initiation (i.e., $\delta_{eq} \geq \delta_{eq}^0$), the damage variable for a particular mode is given by the following expression:

$$d = \frac{\delta_{eq}^f (\delta_{eq} - \delta_{eq}^0)}{\delta_{eq} (\delta_{eq}^f - \delta_{eq}^0)} \tag{37}$$

where δ_{eq}^0 is the initial equivalent displacement at which the initiation criterion for that mode was met and δ_{eq}^f is the displacement at which the material is completely damaged in this failure mode [32]. Figure 2-6 shows the damage variable, equation (37), as a function of the equivalent displacement; the damage variable is equal to one when the material is completely damaged in this failure mode.

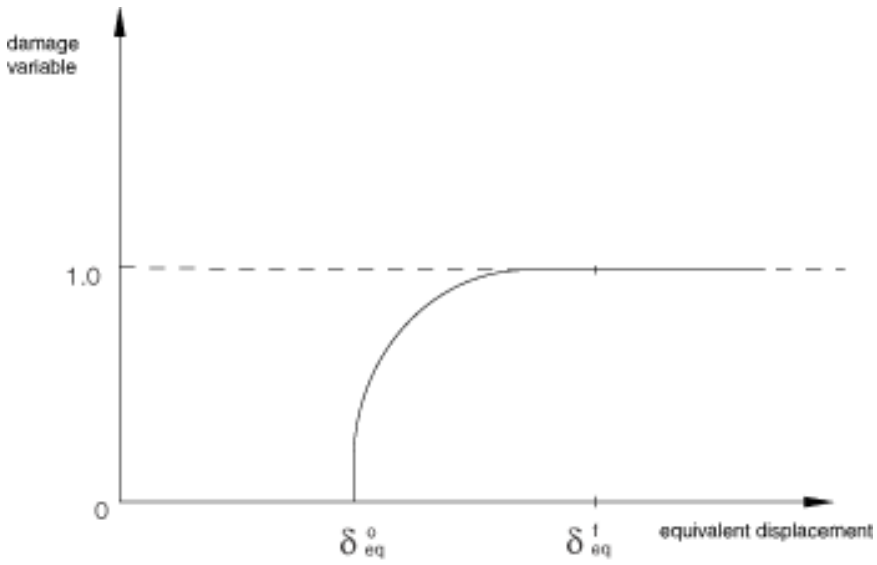

Figure 2-6: Generalized damage variable as function of equivalent displacement [32]

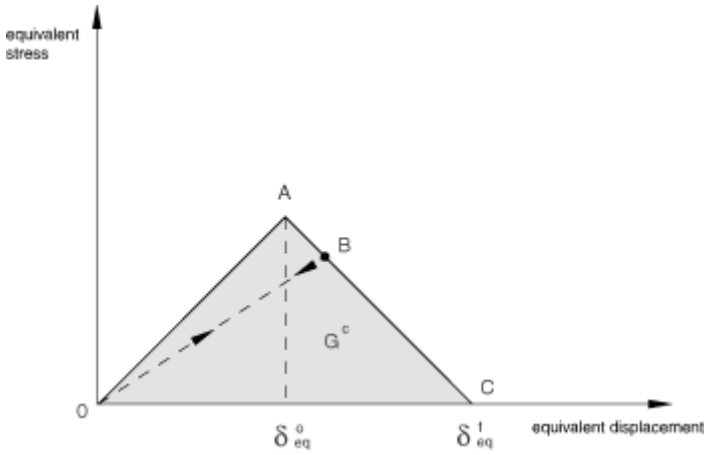

Figure 2-7: Generalized linear damage evolution [32]

Each failure mode has an associated energy dissipated due to failure, G^c, which corresponds to the area of the triangle OAC in Figure 2-7. The values of δ_{eq}^{f} for the various modes depend on the respective G^c values. Unloading from a partially damaged state, such as point B in Figure 2-7, occurs along a linear path toward the origin in the plot of the equivalent stress vs equivalent

displacement; this same path is followed back to point B upon reloading as shown in Figure 2-7 [32].

2.2.2.2 Viscous Regularization Scheme

Lapczyk and Hurtado state that material models exhibiting softening behavior and stiffness degradation often show severe convergence difficulties in implicit analysis programs, such as Abaqus/Standard [31]. This is alleviated by using a viscous regularization scheme.

Abaqus makes use of a regularization scheme in which a viscous damage variable is defined by the evolution equation:

$$\dot{d}_v = \frac{1}{\eta}(d - d_v) \tag{38}$$

where η is the viscosity coefficient representing the relaxation time of the viscous system and d is the damage variable evaluated in the inviscid backbone model. The damaged response of the viscous material is given as equation (25), where the damaged elasticity matrix, C_d, is computed using viscous values of damage variables for each failure mode. Using viscous regularization with a small value of the viscosity parameter (small compared to the characteristic time increment) usually helps improve the rate of convergence of the model in the softening regime, without compromising results. The solution of the viscous system relaxes to that of the inviscid case as:

$$\frac{t}{\eta} \to \infty \tag{39}$$

where t represents time [32]. Viscous regularization parameters were not used for the compressive modulus simulations.

2.2.3 SACMA SRM 1R-94 Compressive Modulus Specimen Modeling

A displacement convergence study for the SACMA SMR 1R-94 compressive modulus specimen is presented in Section 2.2.3.1. Section 2.2.3.2 discusses the results of SACMA SRM 1R-94 coupon modulus predictions and the techniques used to extrapolate relevant data from the modeled compressive modulus specimen.

A one-eighth symmetry model for SACMA SRM 1R-94 was developed for the compressive modulus specimen (Untabbed) with boundary conditions shown in Figure 2-8 and half of the layup for each laminate (i.e. $(0/\pm60)_s$ and $(+60/0/60)_s$). The load is introduced into the specimen by applying an enforced displacement in the 1-direction. All four sides of the labeled region "partitioned unconstrained sections" in Figure 2-8 have no constraints, since the test fixture support plates do not make contact with this region. A gage section is partitioned on the outer face of the specimen, allowing expansion in the 3-direction. The lengths of the partitioned gage section and partitioned unconstrained sections are 0.25 in and 0.1525 in, respectively.

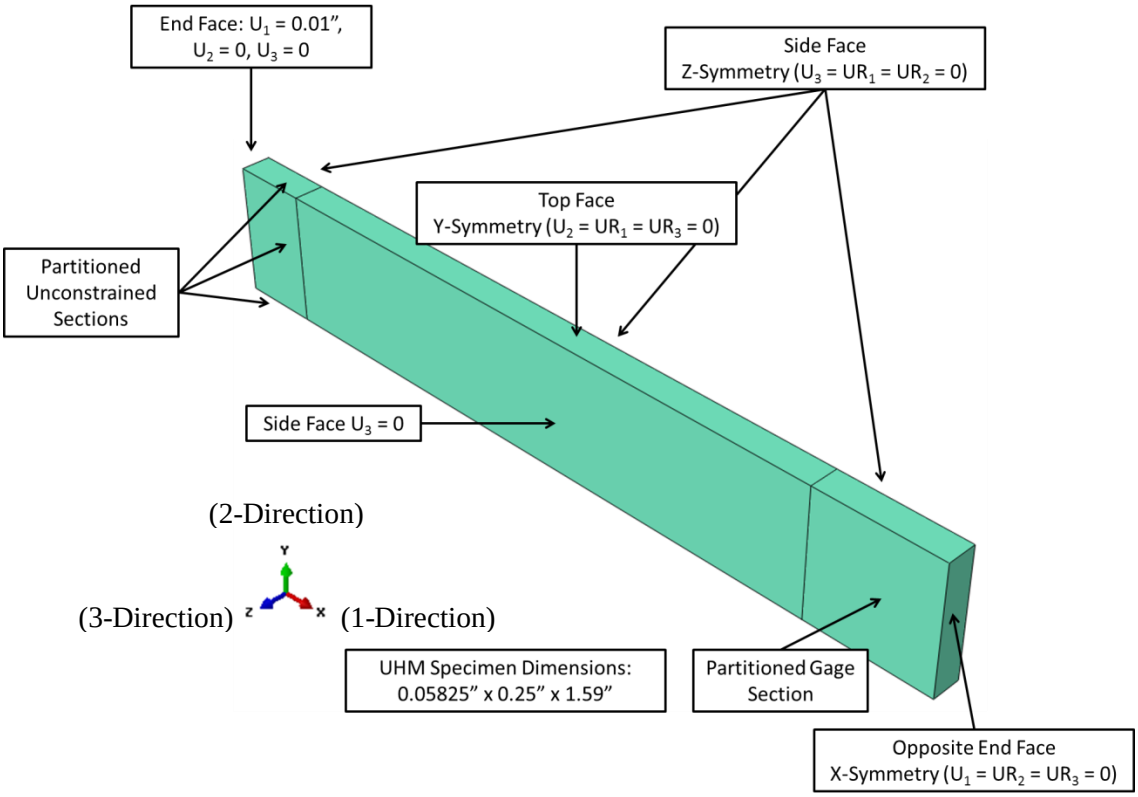

Figure 2-8: Isometric view of one-eighth symmetry model of SACMA SRM 1R-94 compressive modulus specimen with boundary conditions

2.2.3.1 SACMA SRM 1R-94 Compressive Modulus Specimen Convergence Study

In Abaqus, a step is defined as any phase of the problem history. In non-linear problems the objective is to obtain a convergent solution using minimal resources. When using automatic control, the user defines the step and specifies the initial, minimum, and maximum time step. Abaqus then selects the increments as it develops the response in the step. This approach is often more efficient than controlling the increment size because the user cannot predict the response ahead of time [32].

An automatic increment for the step module with an initial time step of 10^{-3} s, minimum time step of 10^{-8} s, maximum time step of 10^{-3} s, and with a total time period of 1.0 s is used throughout the investigations presented in Chapter 2.

The SACMA SRM 1R-94 finite element models were constructed with SC8R elements and the SC8R is an element with an 8-node quadrilateral in-plane general-purpose reduced integration continuum shell element, integration with hourglass control, and can accommodate finite membrane strains [32]. A convergence study was performed to determine a minimum number of continuum shell elements of type SC8R that provide displacement convergence. Increasing the mesh density, with respect to the minimum number of elements, will not result in changes to the displacement for a converged solution.

Shell elements are the only Abaqus built-in element type that can be used for the Hashin failure criteria and damage evolution. When using the composite layup feature within Abaqus with continuum shells, a single element is prescribed for the entire thickness of the composite. The single element contains multiple plies defined using the Abaqus ply input table. If more than one element is used to model the laminate, each element would contain all of the plies from the plies table input [32]. Therefore, only one element is used through the thickness of the SACMA SRM 1R-94 test specimen symmetry model. When using solid elements and the composite layup feature within Abaqus, only one element is prescribed for the entire thickness of the composite, since that element also contains multiple plies. However, a separate layup can be defined for each ply, allowing multiple elements through the thickness of a modeled laminate. Defining a section for each layer of a laminate can become cumbersome. A program called Composite Modeler for Abaqus offers the capability to assign a section corresponding to each ply so that multiple elements span through the laminate thickness.

Although using a smaller number of elements may still produce a converged solution, the objective of this type of convergence study is to find a relatively small number of elements that

can produce a converged solution, such that the computing time required to complete a simulation does not become cumbersome. The cost-benefit relation between finding the optimized converged solution vs. a non-optimized converged solution with reasonable computing time is often not justifiable unless such a simulation needs to be ran hundreds of times. Figure 2-9 shows a graphical representation of an increase in required computing time versus an increase in the number of elements used in a model. The number of elements for a converged solution with the least amount of computing time is often not chosen since once a converged solution is proven, many simulations do not need to be replicated. However, when using a design of experiments approach (Chapter 4), finding the optimized converged solution may be desired for examining all combinations of factors suspected to influence a parameter or set of parameters.

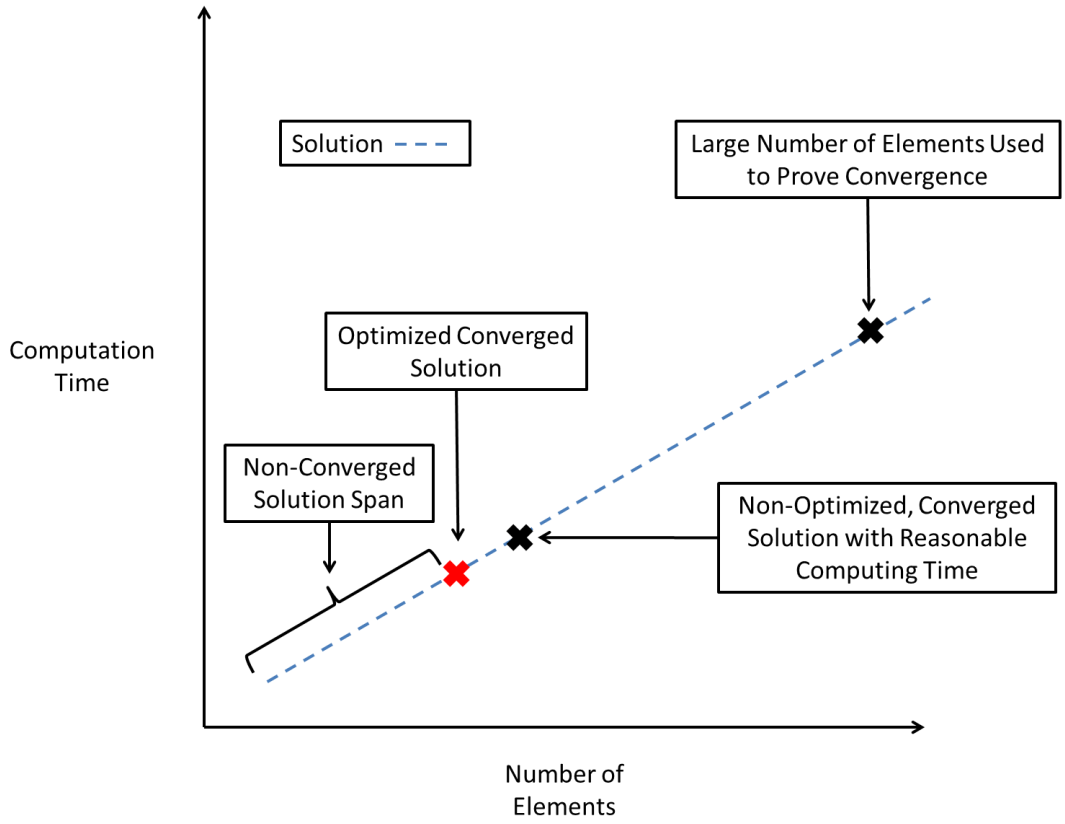

Figure 2-9: Convergence technique

It was determined that the displacement convergence occurred with a minimum of 2,880 elements for the one-eighth symmetry SACMA SRM 1R-94 compressive modulus model for both laminates defined in Table 2-2. See Figures 2-10 (a) for the displacement contour plot with 2,880 (36 x 80) elements. See Figure 2-10 (b) for the displacement contour plot with 5,760 (48 x 120) elements. See Table 2-4 for a displacement comparison at a specific node at the increment when end-crushing occurred. As shown in Table 2-4, the solution has converged with 2,880 elements as no change in displacement was manifest for the more refined mesh. Both Figures 2-10 (a) and (b) highlight the nodal locations used for the displacement comparison listed in Table 2-4.

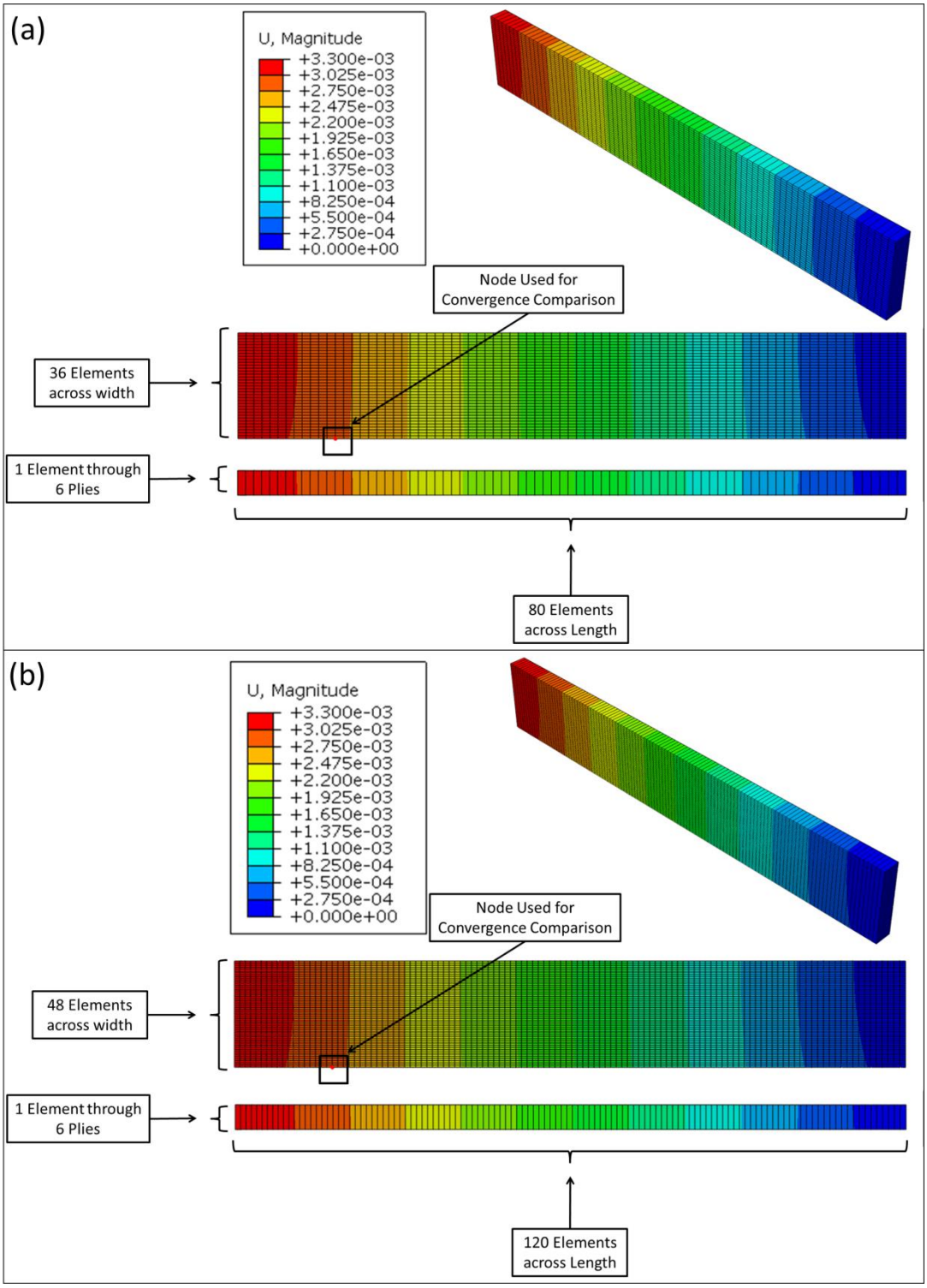

Figure 2-10: Convergence displacement contour plot with of one-eighth symmetry SACMA SRM 1R-94 for enforced end displacement at end-crushing, with (a) 2,880 and (b) 5,760 elements for $[(0/\pm60)_s]_2$ laminate

Table 2-4: SACMA SRM 1R-94 compressive modulus specimen convergence comparison for $[(0/\pm60)_s]_2$ laminate at the same nodal location at the increment when end-crushing occurred

Models Shown in Figure 2-10	Number of Elements in x-direction	Number of Elements in y-direction	Number of Elements in z-direction	Total Elements	Nodal Displacement, u_1 (in)	Difference Between Displacements (Percent)
2,880 Elements Model	80	36	1	2,880	2.81×10^{-3}	0
5,760 Elements Model	120	48	1	5,760	2.81×10^{-3}	0

2.2.3.2 SACMA SRM 1R-94 Compressive Modulus Specimen Modeling Results

The stress-strain curves for both laminates defined in Table 2-2 were predicted by calculating the stress and strain as a function of applied displacement. The stress was calculated by multiplying the summation of nodal forces at the specimen end of the enforced displacement by four and dividing that quantity by the product of the width plus its change in width times the product of the thickness times its change in thickness. The constant thickness used for these two laminates was 0.1165 in. The change in length, width, and thickness were measured at the gage section. The strain was calculated by multiplying the enforced end displacement at each time step by two and dividing that quantity by the original specimen length. Figure 2-21 shows that the reaction forces in the 1-direction of the specimen are homogenous across the entire specimen's length. See equations (40-41):

$$\sigma = \frac{4\sum RF_1}{(\Delta Width + Width)*(\Delta Thickness + Thickness)} \tag{40}$$

$$\varepsilon = \frac{2u_1}{Original\ Length} \tag{41}$$

where,

RF_1: nodal reaction force in the 1-direction
u_1: nodal displacement in the 1-direction

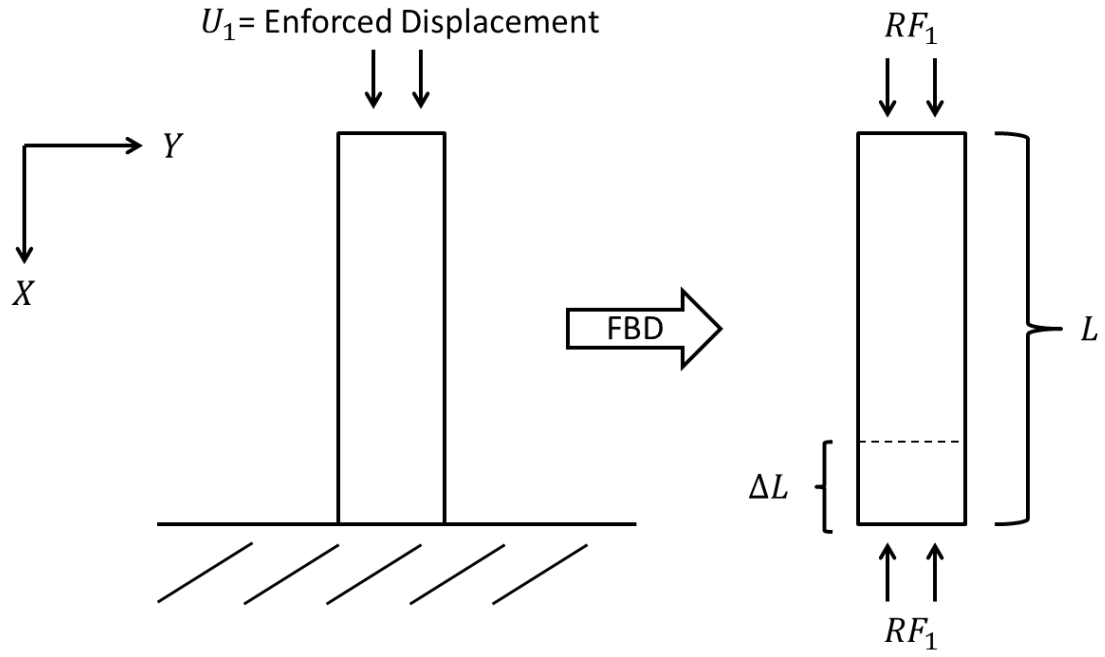

Figure 2-11: SACMA SRM 1R-94 compressive modulus specimen free body diagram with homogenous reaction forces in the 1-direction across entire specimen length

Figures 2-12 and 2-13 show the $[(0/\pm60)_s]_2$ and $[(60/0/\text{-}60)_s]_2$ laminates predicted stress-strain data plotted with the experimental mean, ± two standard deviations, the finite element solution, and an experimental data set. Using Microsoft Excel, with a linear trend and the intercept set equal to zero, the compression modulus, E_{xx} *(C)*, of the Abaqus simulations were found to be 14.38 Msi for both laminates. The predicted moduli based on the finite element solution in Figures 2-12 and 2-13 show a non-linearity due to Poisson's effects. That is to say that the modulus decreases as the compressive load increases, since the gage section is free to expand based on the boundary conditions. The simulations conducted for both laminates had an

enforced displacement of 0.01 in. This was done in order to cover the entire span of what a test specimen might undergo during SACMA modulus testing up to, and beyond end-crushing. Hashin fiber compression failure initiation was produced at 2,210 με for both laminates.

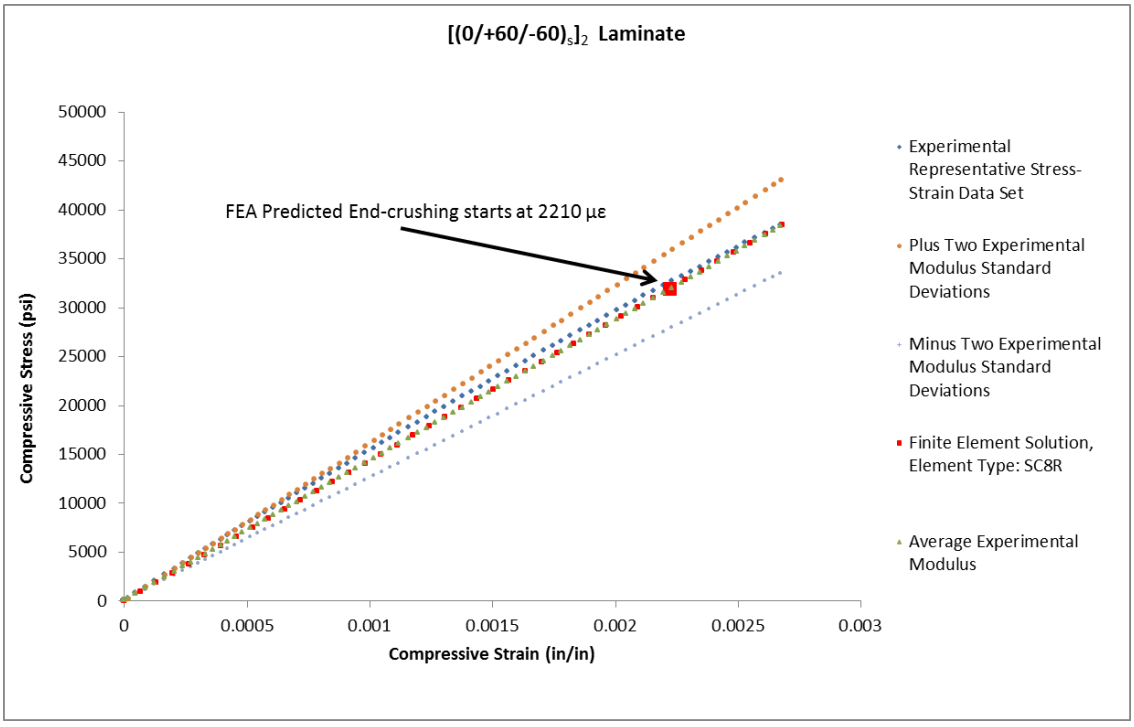

Figure 2-12: SACMA SRM 1R-94 compressive modulus specimen stress versus strain response of $[(0/\pm60)_S]_2$ laminate

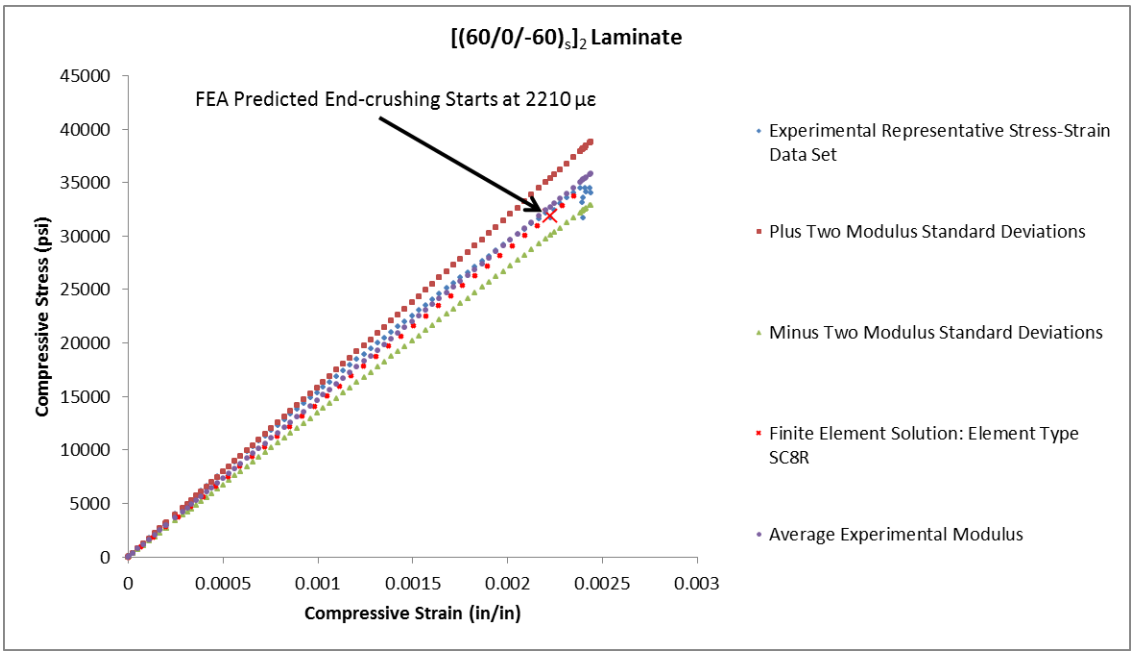

Figure 2-13: SACMA SRM 1R-94 compressive modulus specimen stress versus strain response of $[(60/0/-60)_S]_2$ laminate

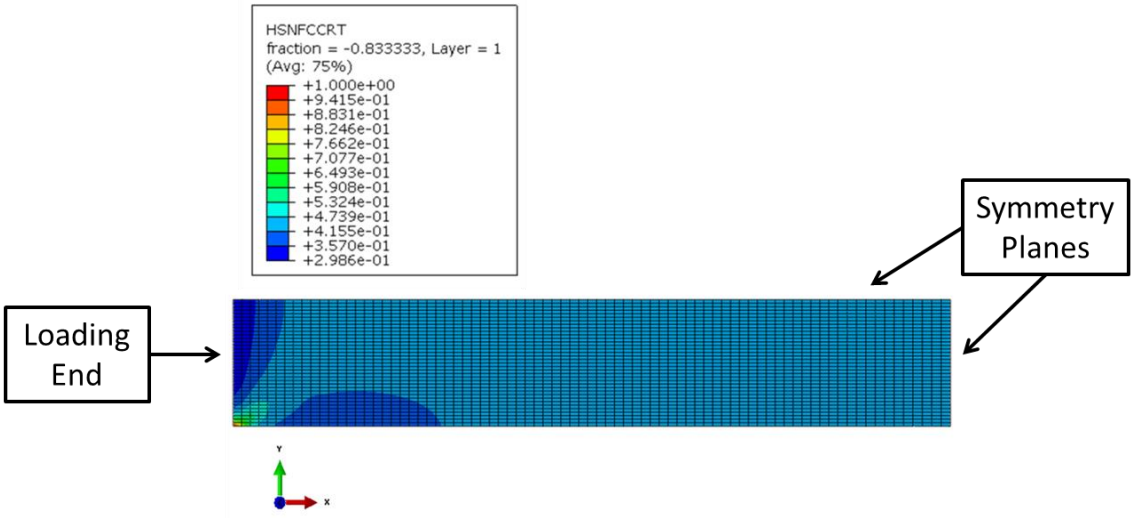

Figure 2-14: Hashin fiber compression failure initiation with failure index listed in the legend. The strain at failure initiation was 2,210 με for the one-eighth symmetry model of SACMA SRM 1R-94 modulus specimen on outer ply of $[(0/\pm60)_S]_2$ laminate

Figure 2-14 shows the damage initiation for the $[(0/\pm60)_S]_2$ laminate on the outer ply at the corner due to end-crushing with the failure index listed in the legend. Predicted end-crushing started at 2,210 με; experimentally, the modulus was calculated from 250 – 2000 με as opposed to the more commonly used limits of 1000 – 3000 με.

2.2.4 Tabbed ASTM D6641 Test Specimen Modeling

An ASTM D6641 test fixture bolt torque relation and respective boundary conditions are presented in Section 2.2.4.1. The basis for the use of cohesive elements is discussed in Section 2.2.4.2. The rationale for examining a continuum response of ASTM D6641's adhesive layer is discussed in Section 2.2.4.3. Section 2.2.4.4 provides a brief overview of the traction separation failure initiation and damage evolution methodology used to model the adhesive layer. Section 2.2.4.5 lists cohesive layer stiffness, failure initiation, and damage evolution values used to model the traction separation response of the adhesive. A displacement convergence study for ASTM D6641 is presented in section 2.2.4.6. Section 2.2.4.7 discusses the results of ASTM D6641 coupon modulus predictions and the techniques used to extrapolate relevant data from the modeled specimen.

Since no strain gages are used for the SACMA SRM 1R-94 compressive strength specimen, modeling techniques are developed for the interfacial behavior of the specimen, tab, and adhesive layers of ASTM D6641 and validated against the corresponding experimental data. The same techniques are then applied to the tabbed SACMA SRM 1R-94 compressive strength specimen (Discussed in Section 2.2.5). This approach allows a numerical determination of the modulus of the compressive strength specimen, which can be compared to the compressive modulus specimen.

2.2.4.1 ASTM D6641 Test Fixture Bolt Torque and Boundary Conditions

The bolts used in the ASTM D6641 test fixture are 0.25 in.-28 UNF socket-head cap screws, for which the relation between the clamping force, *F*, per bolt (lb) and the applied torque *T* (in.-lb) is [37]:

$$F = 38.47\,T \tag{42}$$

Using equation (42), and an applied torque of 25 in.-lb, the force on each bolt is 962 lb. The displacement at the interface between the bolt head and test fixture is calculated using the relation:

$$\delta = \frac{FL}{AE} \tag{43}$$

where,

L:	L = 2.2325 in. Figure 2-15 defines the length from the bolt head to threading of the opposing ASTM D6641 test fixture block.
A:	cross-sectional area of bolt, $A = 4.91 \times 10^{-2}$ in^2
E:	Elastic modulus of bolt, E = 28.4 Msi

Using the listed values for the bolt, the displacement is found to be 1.54×10^{-3} in; however, since a one-eighth symmetry model is investigated, the displacement is divided by two, resulting in 7.71×10^{-4} in. Since dimensioned drawings are not available to the author's knowledge, a dial caliper was used to determine the test fixture dimensions. The recess within the test fixture for an extensometer was omitted for simplicity. Figure 2-16 shows the test fixture block dimensions and defines the interfacial bolt regions used for bolt-displacement. Figure 2-17 shows the bolt hole locations referenced from the test fixture block edges. Bolt load determination techniques utilizing more widely used criteria are investigated in Chapter 4. For the scope of Chapter 2, ultimate laminate failure (ULF) is defined as failure across the width for all 0° plies in the investigated laminates.

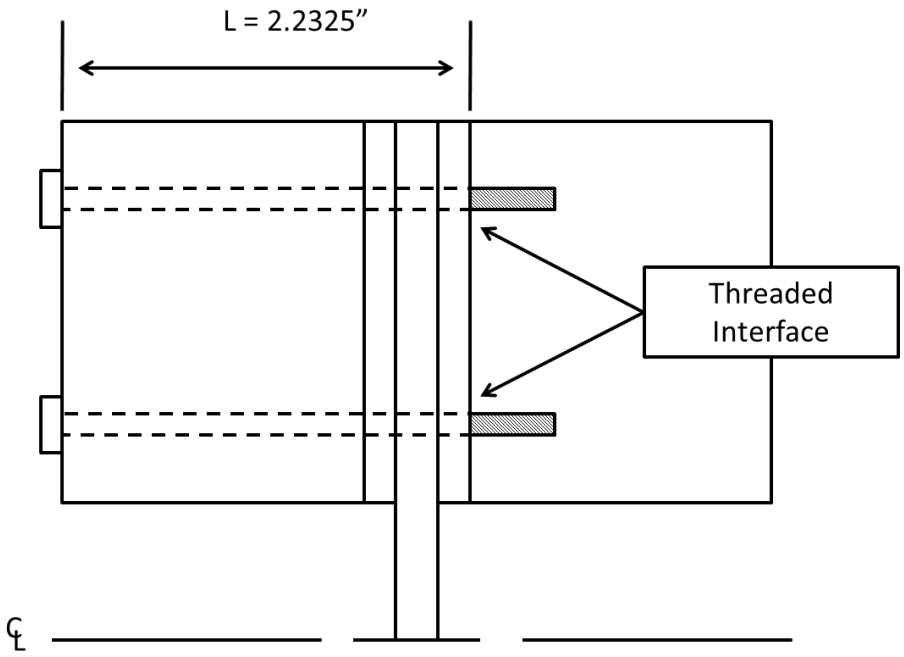

Figure 2-15: Length used to determine bolt displacement spanning test fixture block and test specimen thickness

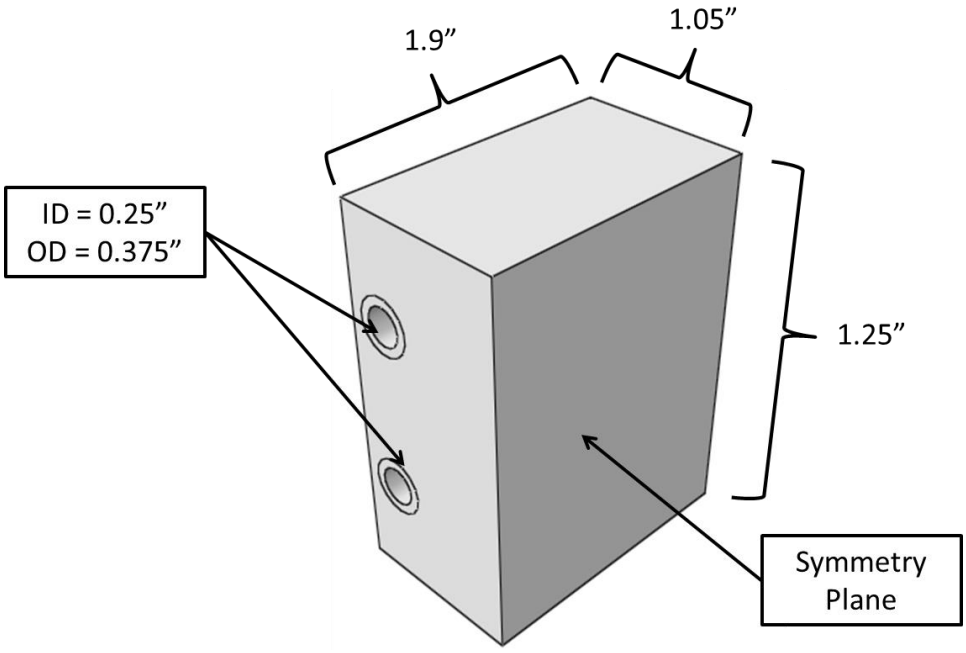

Figure 2-16: ASTM D6641one-eighth symmetry model of test fixture block dimensions and bolt interfacial region

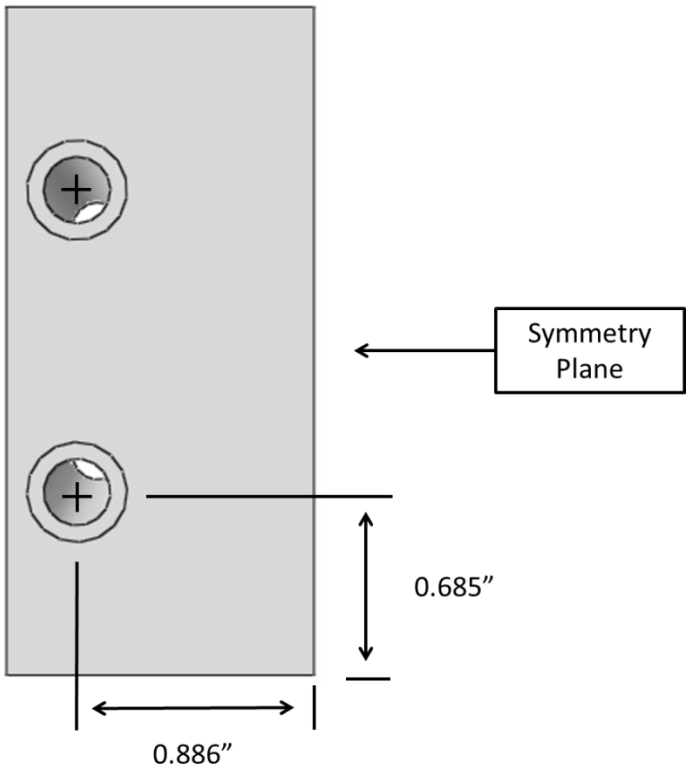

Figure 2-17: ASTM D6641 one-eighth symmetry model of test fixture bolt-hole locations

A one-eighth symmetry model was developed for the ASTM D6641 specimen with boundary conditions shown in Figures 2-18 and 2-19. The tabs modeled had a $[0/45]_S$ layup made of 5HS carbon fabric and epoxy resin; the modeled thickness was set equal to 0.095 in. The partitioned lines shown in Figure 2-18 were used in order to align the nodes of the cohesive elements of the adhesive layer with the nodes of the continuum shell elements of the tab and the UHM laminate. Figure 2-19 lists the bolt-displacement used for the ASTM D6641 models in Chapter 2.

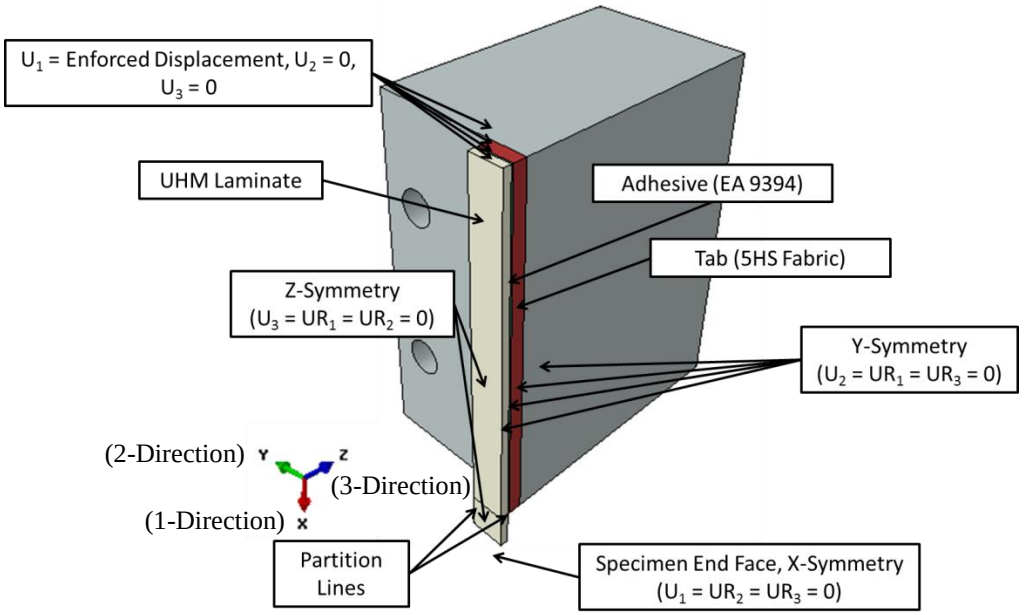

Figure 2-18: View of one-eighth symmetry model of ASTM D6641 test specimen with test fixture and boundary conditions

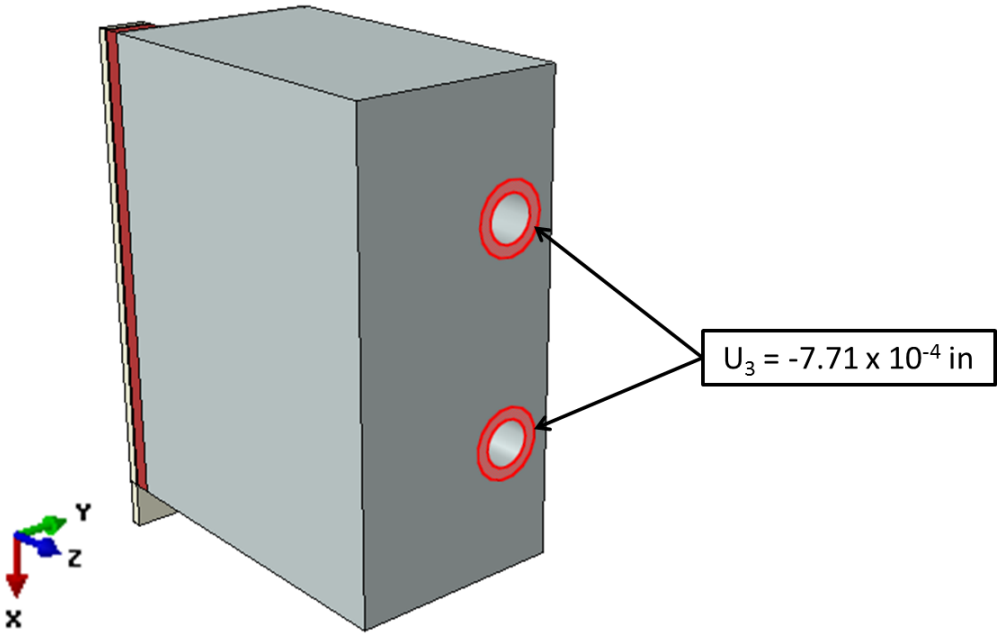

Figure 2-19: View of one-eighth symmetry model of ASTM D6641 enforced boundary conditions on bolt contact region

A tie constraint numerically welds two separate surfaces together so that there is no relative motion between them. This type of constraint allows you to fuse together two regions even though the meshes created on the surfaces of the regions may be dissimilar [32]. Figure 2-20 shows the tie constraint defined between the test fixture which is the master surface, and the partitioned test specimen which is the slave surface. In Abaqus, a slave surface cannot penetrate a master surface; however, a master surface can penetrate a slave surface.

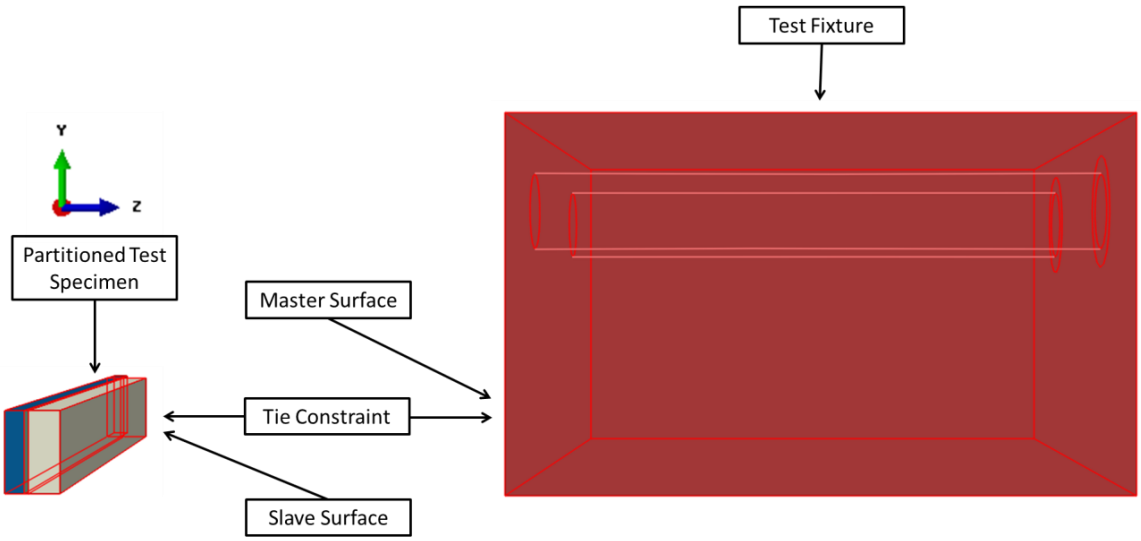

Figure 2-20: Exploded view of one-eighth symmetry model of ASTM D6641 interaction constraints

2.2.4.2 ASTM D6641 Adhesive Modeling

Cohesive elements are advantageous to model the behavior of adhesive joints, interfaces in composites, and other situations where the integrity and strength of interfaces may be of interest. If an interface has a finite thickness and macroscopic properties, it may be more appropriate to model the response using a conventional material model, particularly a continuum

approach [32]. For the entire specimen thickness, the two adhesive layers account for 7.77% of the total thickness. Therefore, a finite thickness is apparent and a continuum response is investigated.

2.2.4.3 ASTM D6641 Continuum Response of Adhesive Layer

For adhesive layers with finite thickness it is assumed that the cohesive layer is subjected to only one normal component of strain, which is the through-thickness strain, and to two transverse shear strain components. The other two direct components of the strain (in-plane membrane strains) and the in-plane (membrane) shear strains are assumed to be zero for the constitutive calculations [32]. A set of simulations is also conducted to examine the adhesive strains using element type C3D8I.

For the continuum adhesive response approach, an isotropic tensile modulus of 0.426 Msi with a Poisson's Ratio of 0.41 was used for EA 9394 under the conditions prescribed in Section 2.2.4.1 with an enforced end-displacement of 3.5×10^{-3} in for the $[(0/\pm 60)_S]_2$ laminate. Material properties came from tests previously conducted at Penn State's Applied Research Lab.

2.2.4.4 ASTM D6641 Traction Separation Response of Adhesive Layer

In order to accurately model the behavior of an adhesive under the loading conditions of ASTM D6641, the adhesive must be defined in terms of a traction-separation law, which can be used to model the delamination at interfaces in composites directly in terms of traction versus separation [32].

The traction separation model used in Abaqus assumes initially linear elastic behavior followed by the initiation and evolution of damage. The nominal stresses are the force components divided by the original area at each integration point, while the nominal strains are the separations divided by the original thickness at each integration point. The nominal strains can be defined as:

$$\varepsilon_n = \frac{\delta_n}{T_0} \tag{44}$$

$$\varepsilon_s = \frac{\delta_s}{T_0} \tag{45}$$

$$\varepsilon_t = \frac{\delta_t}{T_0} \tag{46}$$

where,

T_0:	the original thickness of the cohesive element
t_n, t_s, t_t:	normal and two shear tractions along the local 3-, 1-, and 2-directions
δ_n, δ_s, δ_t:	separations along the local 3-, 1-, and 2-directions

The coordinate system for the traction vectors is defined in Figure 2-21.

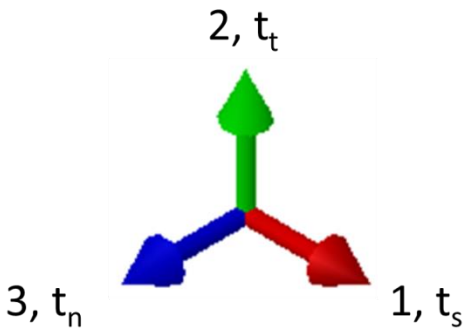

Figure 2-21: Coordinate system for traction vectors

The elastic behavior is written as:

$$t = \begin{Bmatrix} t_n \\ t_s \\ t_t \end{Bmatrix} = \begin{bmatrix} K_{nn} & K_{ns} & K_{nt} \\ K_{ns} & K_{ss} & K_{st} \\ K_{nt} & K_{st} & K_{tt} \end{bmatrix} \begin{Bmatrix} \varepsilon_n \\ \varepsilon_s \\ \varepsilon_t \end{Bmatrix} = K\varepsilon \tag{47}$$

where *t* is the nominal traction stress vector. In this study, uncoupled behavior is assumed and the relation in equation (48) is used. For uncoupled behavior each traction component depends only on its conjugate nominal strain [32].

$$t = \begin{Bmatrix} t_n \\ t_s \\ t_t \end{Bmatrix} = \begin{bmatrix} K_{nn} & 0 & 0 \\ 0 & K_{ss} & 0 \\ 0 & 0 & K_{tt} \end{bmatrix} \begin{Bmatrix} \varepsilon_n \\ \varepsilon_s \\ \varepsilon_t \end{Bmatrix} = K\varepsilon \tag{48}$$

Damage of the traction-separation response is defined within the same general framework used for conventional materials within Abaqus. For the scope of this investigation, the quadratic nominal stress criterion is used for damage initiation and is defined as:

$$\left\{\frac{t_n}{t_n^0}\right\}^2 + \left\{\frac{t_s}{t_s^0}\right\}^2 + \left\{\frac{t_t}{t_t^0}\right\}^2 = 1 \tag{49}$$

where,

t_n^0, t_s^0, t_t^0 — peak values of the nominal stress when the deformation is either purely normal to the interface or purely in the first or the second shear direction [32]

Damage evolution for the traction-separation response is defined with a scalar damage variable, *D*, which represents the overall damage in the material and captures the combined effects of all the active damage mechanisms. The damage variable initially has a value of zero. The stress components of the traction-separation model are affected by the damage using these relations:

$$t_n = \begin{cases} (1-D)\bar{t}_{n,} & \bar{t}_n \geq 0 \\ \bar{t}_{n,}\ otherwise\ (no\ damage\ to\ compressive\ stiffness) \end{cases} \tag{50}$$

$$t_s = (1-D)\bar{t}_s \tag{51}$$

$$t_t = (1 - D)\bar{t}_t \quad (52)$$

where,

D:	Varies from 0 to 1. See equation (60)
$\bar{t}_n, \bar{t}_s, \bar{t}_t$:	stress components predicted by the elastic traction-separation behavior for the current strains without damage [32]

For this investigation, damage evolution was chosen based on energy, meaning that energy is dissipated as a result of the damage process, also called fracture energy. Figure 2-22 shows an example of linear damage evolution after point A in the triangle OAB. The fracture energy, designated G^C in Figure 2-22, is equal to the area under the traction-separation curve.

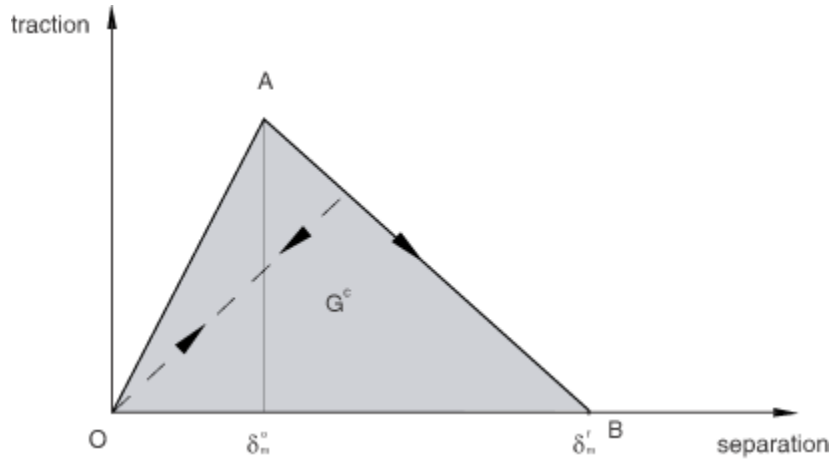

Figure 2-22: Linear damage evolution of traction separation response [32]

The dependence of the fracture energy on the mode mix can be defined based on a power law fracture criterion, and is used in this investigation. The mode mix defines the work done by the tractions and their conjugate relative displacements as:

G_n:	work done by normal direction
G_s:	work done by first shear direction
G_t:	work done by second shear direction

The total energy of the work done by the normal, first shear, and second shear directions are given as:

$$G_T = G_n + G_s + G_t \tag{53}$$

The mode mix definitions based on energies are:

$$m_1 = \frac{G_n}{G_T} \tag{54}$$

$$m_2 = \frac{G_s}{G_T} \tag{55}$$

$$m_3 = \frac{G_t}{G_T} \tag{56}$$

The power law criterion states that failure under mixed-mode conditions is governed by a power law interaction of the energies required to cause failure in the individual modes [32]. It is given by:

$$\left\{\frac{G_n}{G_n^C}\right\}^\alpha + \left\{\frac{G_s}{G_s^C}\right\}^\alpha + \left\{\frac{G_t}{G_t^C}\right\}^\alpha = 1 \tag{57}$$

where,

G_n^C, G_s^C, G_t^C: critical strain energy release rates required to cause failure in the normal, first, and second shear directions

When equation (57) has been satisfied, $G^C = G_T$, which is rewritten as:

$$G^C = \frac{1}{\left(\left\{\frac{m_1}{G_n^C}\right\}^\alpha + \left\{\frac{m_2}{G_s^C}\right\}^\alpha + \left\{\frac{m_3}{G_t^C}\right\}^\alpha\right)^{\frac{1}{\alpha}}} \tag{58}$$

Camanho and Davila [38] define evolution of damage under a combination of normal and shear deformation across the interface with an effective displacement:

$$\delta_m = \sqrt{\langle\delta_n\rangle^2 + \delta_s^2 + \delta_t^2} \tag{59}$$

In this investigation, exponential damage evolution was implemented in the model. The EA 9394 adhesive's traction separation response more closely resembles a step function drop after damage initiation. This technique uses a damage variable, *D*, that is defined as:

$$D = \int_{\delta_m^o}^{\delta_m^f} \frac{T_{eff} d\delta}{G^C - G_o} \tag{60}$$

where,

T_{eff}:	effective traction
δ:	effective displacement
δ_m^f:	effective displacement at complete failure
δ_m^o:	effective displacement at the initiation of damage. See Figure 2-22
G_o:	elastic energy at damage initiation

A viscous regularization scheme was implemented analogous to equation (38), in which the solution of the viscous system relaxes to that of the inviscid case.

2.2.4.5 ASTM D6641 Traction Separation Properties

The stiffness of the cohesive layer is estimated using the relation:

$$K_{nn} = K_{ss} = K_{tt} = \frac{\alpha E_{33}}{t} \tag{61}$$

where,

α:	parameter much larger than 1
t:	thickness of adhesive
E_{33}:	E_{33} = E (T) of EA 9394

For values of α greater than 50, the loss of stiffness due to the presence of the interface is less than 2%, which is sufficiently accurate for most problems [17]. The calculated stiffness estimate used for this investigation is 1.64 x $10^9 \frac{psi}{in}$. The strength values, listed in Table 2-5 are estimated

using the associated strengths for EA 9394 and the damage evolution properties, from mode I and II interlaminar fracture toughness tests of EA 9394, are listed in Table 2-6. A viscosity coefficient, η, for viscous regularization was chosen as 10^{-4} s.

Table 2-5: EA 9394 failure criteria for damage initiation

Nominal Stress Normal-only Mode (psi)	Nominal Stress First Direction (psi)	Nominal Stress Second Direction (psi)
7500	4400	4400

*Nominal stress first direction and nominal stress second direction are shear directions

Table 2-6: EA 9394 damage evolution properties

$G_I \left(\frac{in\ lb}{in^2}\right)$	$G_{II} \left(\frac{in\ lb}{in^2}\right)$
2.22	4.88

2.2.4.6 ASTM D6641 Test Specimen Convergence Study

A localized mesh-refinement was used in part of the adhesive section, labeled Region 1 in Figure 2-23 (a), and the gage section of the model, labeled region 2 in Figure 2-23 (b). Region 1 has a length along the x-direction of 0.15 in. Using a localized mesh-refinement allows for large mesh densities in regions of interest and small mesh densities in regions that are not relevant. Using a localized mesh-refinement reduces required computational resources.

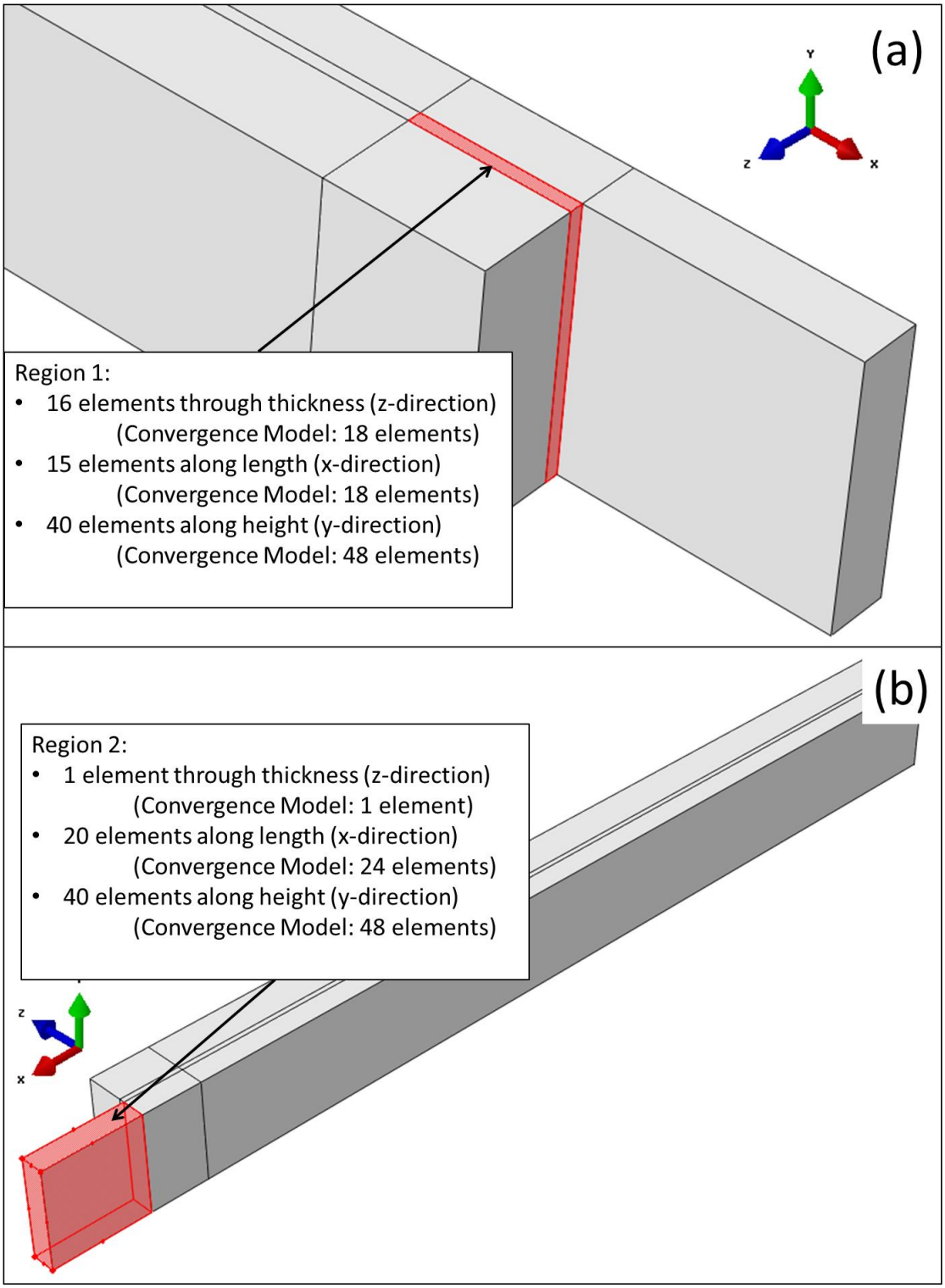

Figure 2-23: ASTM D6641 test specimen with partitioned regions to utilize a localized mesh-refinement approach with 9,600 elements in region 1 (a) and 800 elements in region 2 (b) (Test fixture and mesh not shown)

The element type C3D8I, an 8-node linear brick with incompatible modes, was used for the steel test fixture and the adhesive region for the convergence study. A total of 1,107 elements were created to fill the volume of the test fixture's geometry. In this instance, the test fixture mesh density is not relevant to the strength and modulus predictions extrapolated from the gage section, which is why the relatively small number elements are assigned. It was determined that the displacement convergence occurred with a minimum of 9,600 (15 x 40 x 16) elements in region 1 and 800 (20 x 40 x 1) elements in region 2. In total, the model consisted of 14,147 elements. The model used for a convergence comparison contained a total of 21,459 elements; Figure 2-23 (a) and (b) list the respective meshing dimensions used for the convergence model.

Figure 2-24 (a) shows the convergence displacement contour plot for the 14,147 element model and Figure 2-24 (b) shows the 21,459 element model's displacement contour plot. Table 2-7 shows the convergence comparison at the same nodal location within each specified region; the nodal locations used are labeled in Figure 2-24 (a) and (b). As shown in Table 2-7, the solution has converged with 14,147 elements as no change in displacement was manifest for the more refined mesh.

Table 2-7: ASTM D6641 specimen convergence comparison for $[(0/\pm60)_s]_2$ laminate at same nodes at ULF

14,147 Element Model		21,459 Element Model		
Region	Displacement, u_1 (in)	Region	Displacement, u_1 (in)	Difference between Displacements (%)
1	1.40×10^{-3}	1	1.40×10^{-3}	0.00
2	2.07×10^{-4}	2	2.07×10^{-4}	0.00

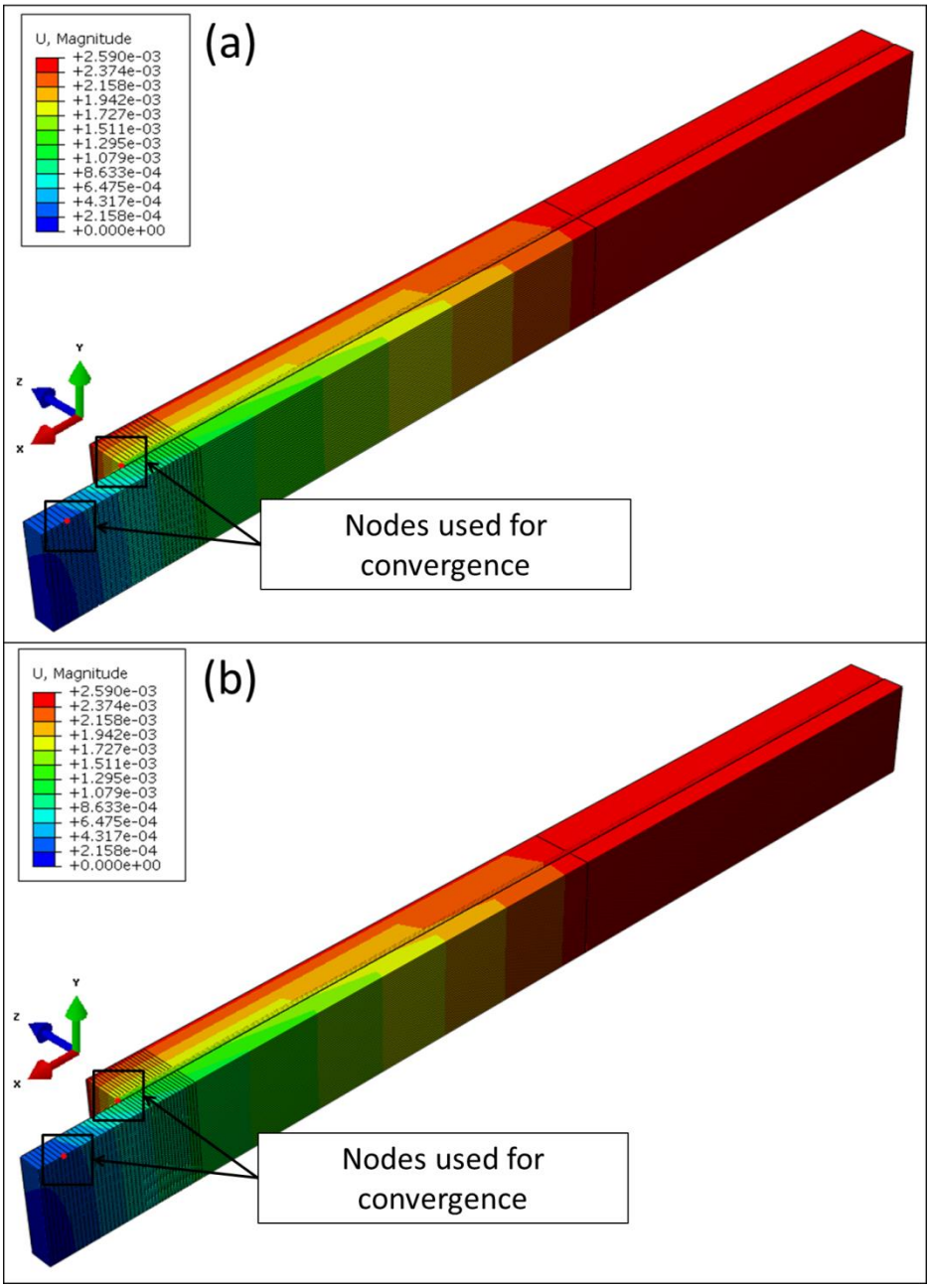

Figure 2-24: ASTM D6641 $[(0/\pm60)_s]_2$ laminate displacement contour plot comparison at Hashin fiber compression ULF between model with 14,147 elements (a) and model with 21,459 elements (b) to demonstrate convergence with C3D8I elements used in adhesive layer (Test fixture not shown)

Turon et al. discuss in [17] that the estimated stiffness and strength parameters used in cohesive zone models are mesh-size dependent. Therefore, convergence studies are not pursued

for the models using either a continuum response or traction separation response in the adhesive layer. Furthermore, this makes using a localized mesh-refinement inappropriate for both response types. Therefore, a minimum element to length ratio of 60 elements/inch (Except for the cohesive zone, which can only have one element through the thickness) is adhered to in all models using cohesive elements in order to gain a sense of each modeled test specimen's behavior. Ideally, it would be optimal to determine the correct mesh-dependent stiffness and strength parameters by constructing a double cantilever beam and end-notched flexure model for EA 9394, then use the same meshing dimensions, stiffness, and strength parameters in the ASTM D6641 and SACMA SRM 1R-94 adhesive layers. However, such an approach is resource intensive and was not practical.

2.2.4.7 ASTM D6641 Test Specimen Modeling Results

Figure 2-25 shows a free body diagram of the symmetry model, followed by a free body diagram of the UHM laminate. Figure 2-25 shows that the reaction forces in the 1-direction of the specimen are homogenous across the gage section. The strain must be calculated by dividing the average displacement across a plane parallel to the YZ-plane below the gage section, since the reaction forces are heterogeneous above the gage section. Using displacement data from where the forces are heterogeneous results in artificially high calculated compressive moduli.

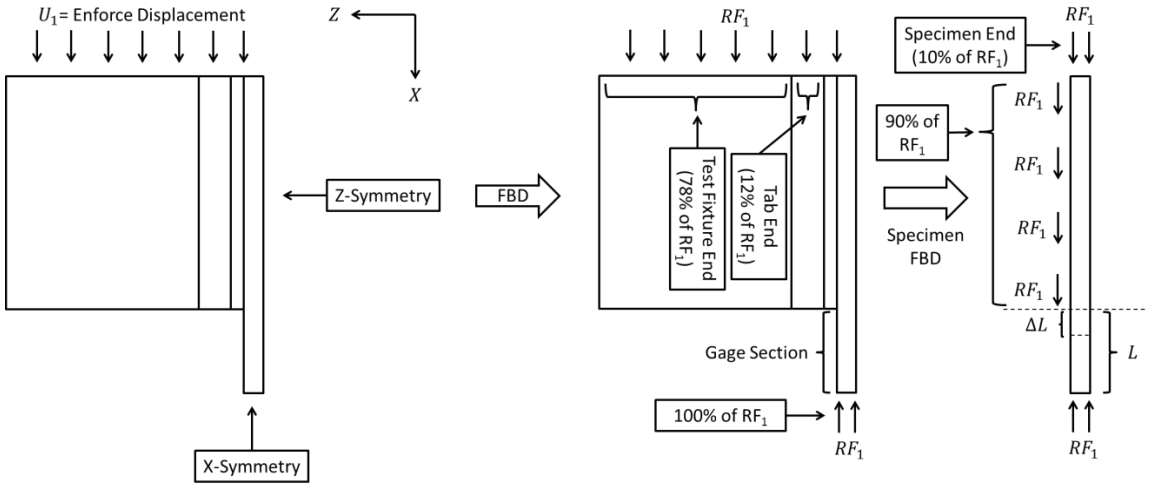

Figure 2-25: ASTM D6641 free body diagram and UHM laminate free body diagram with homogenous reaction forces in the 1-direction across the gage section for symmetry model

The model in Figure 2-24 (a) and lamina properties shown in Table 2-2 were used to predict the response of the stress versus strain for the $[(0/\pm60)_s]_2$ and the $[(+60/0/-60)_s]_2$ laminates. The stress versus strain responses for both laminates are plotted in Figures 2-26, 2-27, 2-28, and 2-29. Figure 2-26 shows the predicted FEA response of the $[(0/\pm60)_s]_2$ laminate and Figure 2-27 shows Figure 2-26's data plotted against experimental data. Figure 2-28 shows the predicted FEA response of the $[(+60/0/-60)_s]_2$ laminate and Figure 2-29 shows Figure 2-28's data plotted against experimental data. The corresponding predicted moduli and strengths are listed in Table 2-8. The first ply failure (FPF) occurred in the outermost 0° plies for both laminates with fiber compression as the failure mode. The strengths were determined when the Hashin fiber compression failure criteria, referred to herein as ultimate laminate failure (ULF), was equal to one across the width for all 0° plies. The moduli were calculated by using a linear trend with the intercept set equal to zero using Microsoft Excel up to the data point corresponding to first ply failure. Using the model with C3D8I elements in the adhesive layer, it was determined that approximately 10% of the compressive load (In the 1-direction) is transferred at the UHM

laminate end, approximately 12% of the load is transferred through the tab ends, and the remaining 78% of the load is transferred through the test fixture ends.

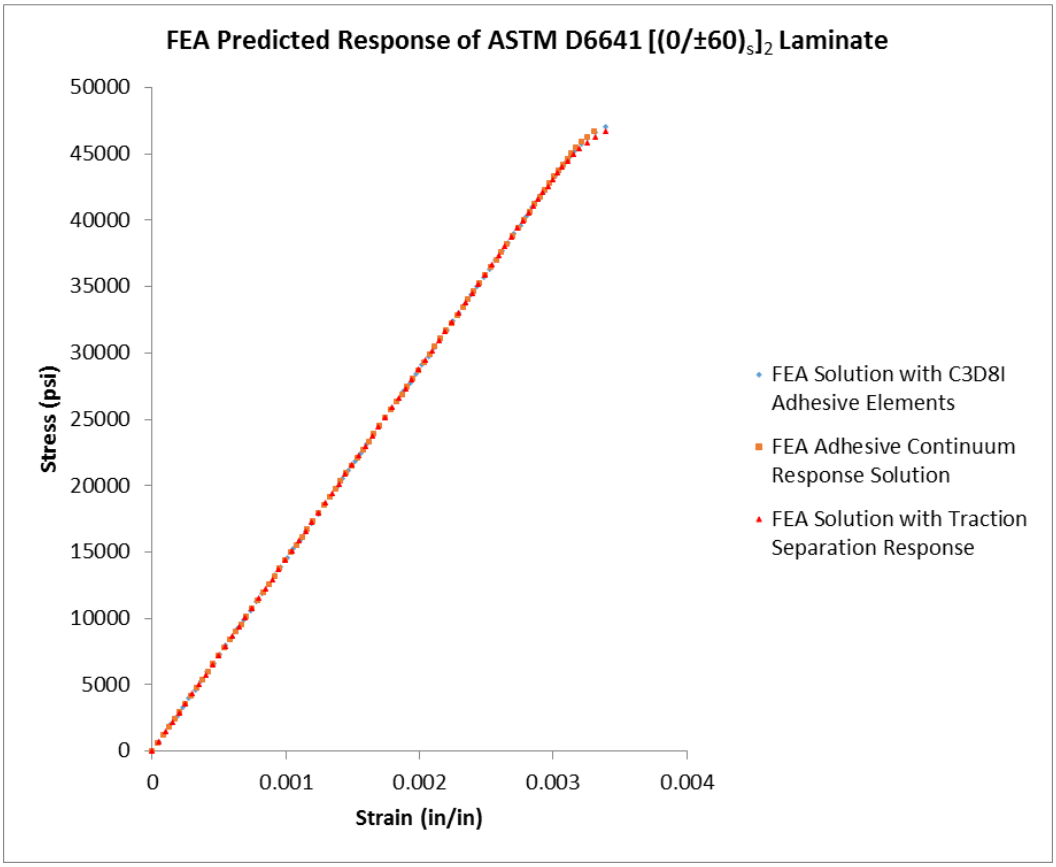

Figure 2-26: ASTM D6641 predicted stress versus strain response of $[(0/\pm60)_S]_2$ laminate

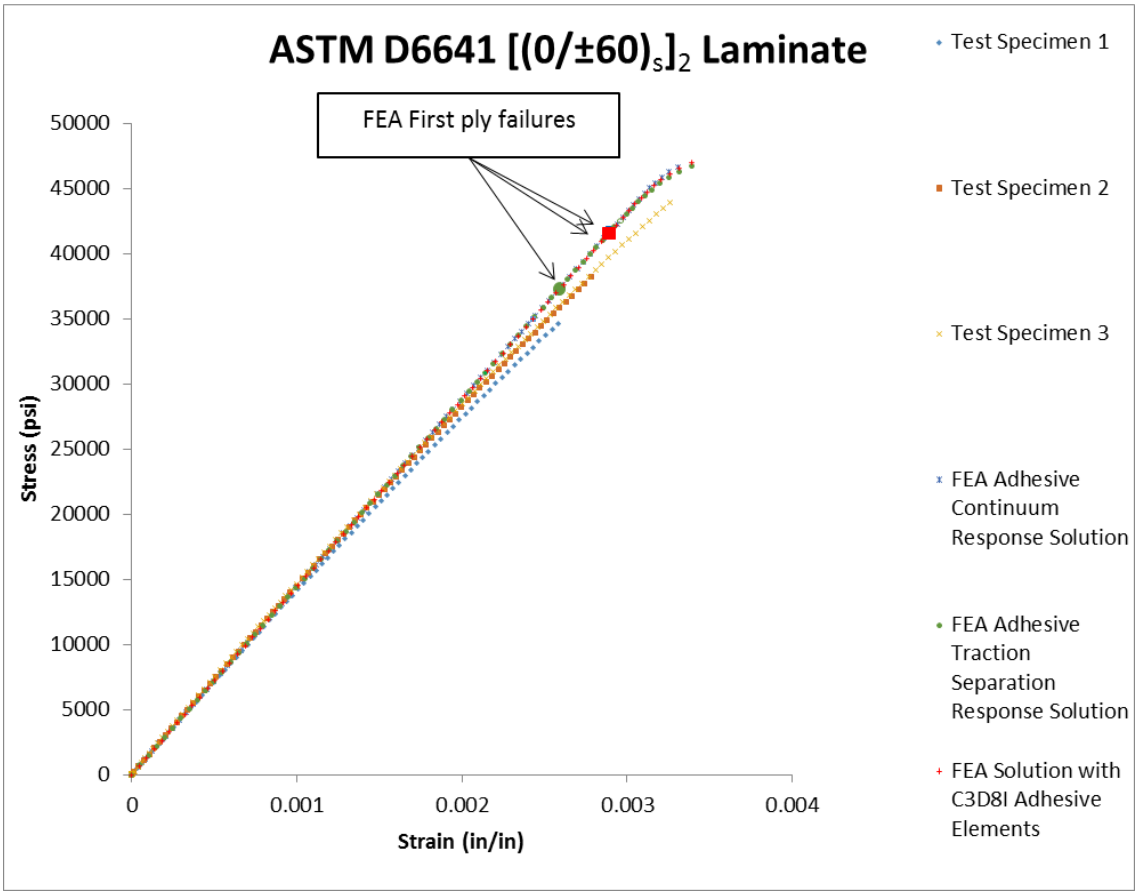

Figure 2-27: ASTM D6641 stress versus strain response of $[(0/\pm60)_S]_2$ laminate

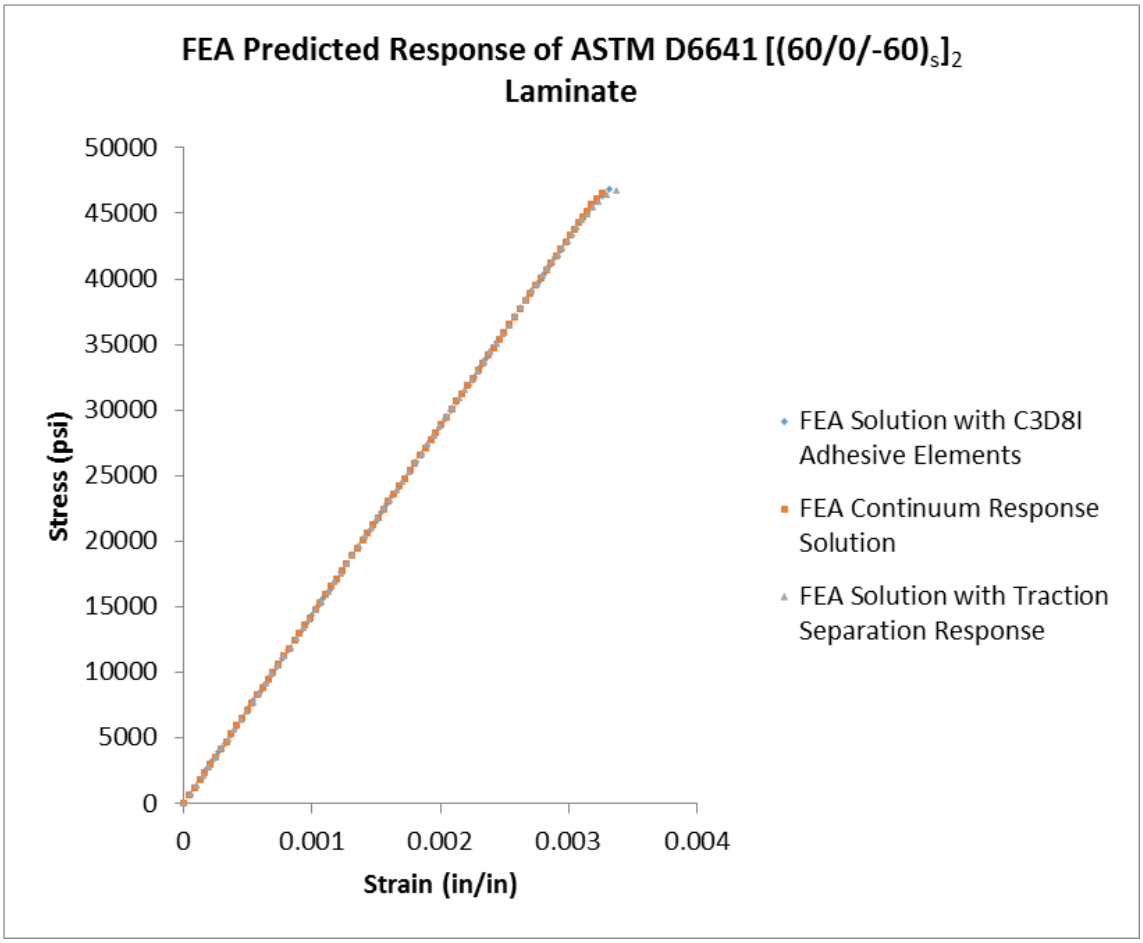

Figure 2-28: ASTM D6641 predicted stress versus strain response of $[(0/\pm 60)_S]_2$ laminate

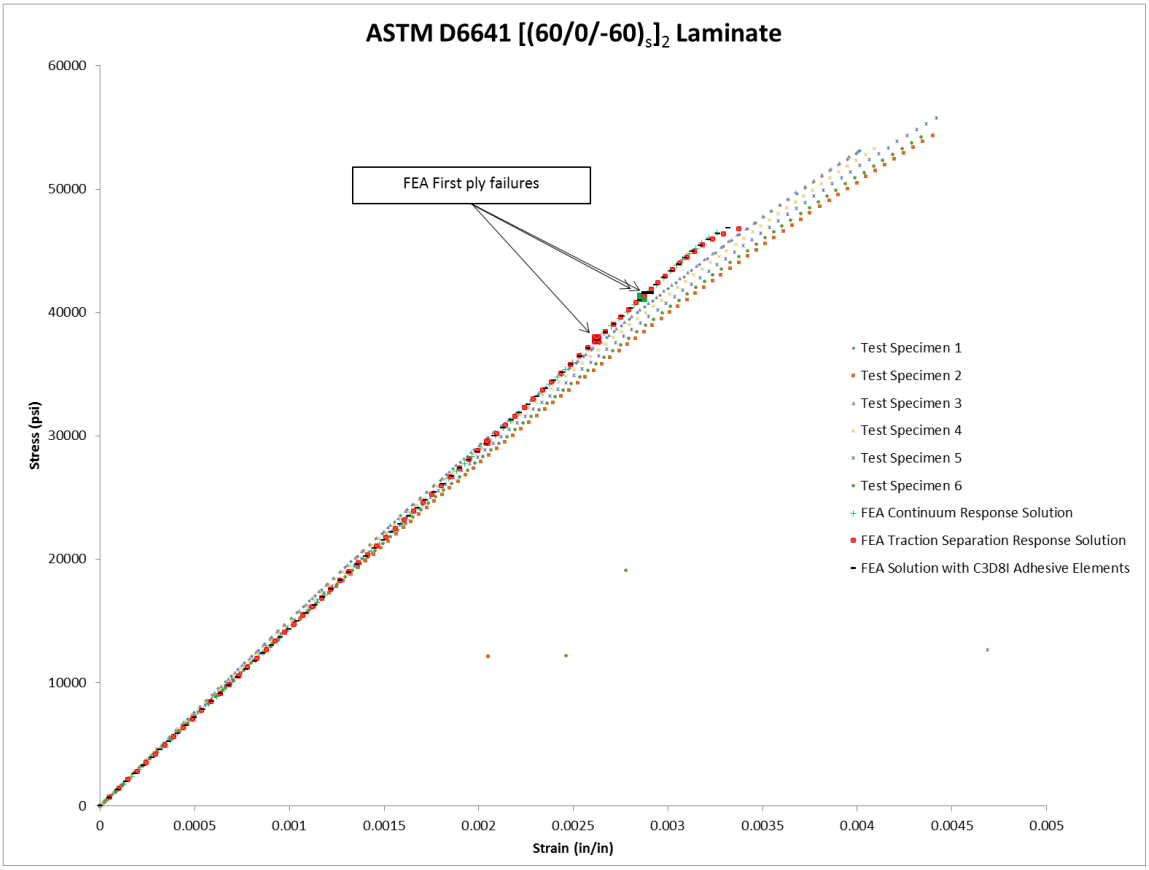

Figure 2-29: ASTM D6641 stress versus strain response of $[(+60/0/-60)_s]_2$ laminate

Table 2-8: ASTM D6641 finite element modulus and strength results

UHM Laminate	Response Type modeled in Adhesive Layer	Compression Strength (ksi)	Stress at FPF (ksi)	Compression Modulus (Msi) up to FPF
$[(0/\pm60)_s]_2$	Continuum	46.7	41.7	14.41
	Traction Separation	46.7	37.3	14.43
	C3D8I Elements	47.0	41.6	14.40
$[(+60/0/-60)_s]_2$	Continuum	46.5	41.2	14.40
	Traction Separation	46.8	37.2	14.43
	C3D8I Elements	46.8	41.6	14.40

Using element type C3D8I in the adhesive layer in order to examine the strain behavior, 16 elements were assigned through the thickness. The largest strains in the specimen at ULF occur in the adhesive layer. See Figure 2-30 for strain contour plots in the 13 plane and 1-direction. The largest strain in the 13 plane of the adhesive at ULF is 7.4 x 10^{-2} in/in.

The largest strain in the 1-direction of the adhesive at ULF is 2.17 x 10^{-2} in/in. The experimentally determined failure tensile strain of EA 9394 is 2.47 x 10^{-2} in/in. Assuming the failure tensile strain of EA 9394 is equal to the failure compressive strain, then no failure occurs purely in the 1-direction.

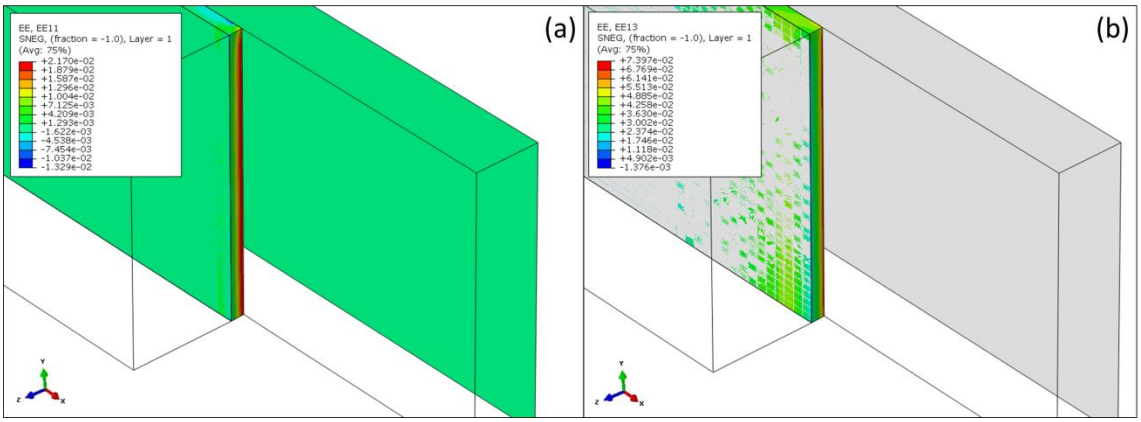

Figure 2-30: Strain contour plot in the 13 plane and 1-direction for one-eighth symmetry model of $[(0/\pm60)_S]_2$ ASTM D6641 specimen with C3D8I elements in the adhesive layer (Mesh hidden)

Overall, the largest strains in the plies occurred in the 1-direciton in the outermost 0° ply for the continuum response, traction separation response, and element type C3D8I used in the adhesive layer.

2.2.5 SACMA SRM 1R-94 Compressive Strength Specimen Modeling

A displacement convergence study for the SACMA SMR 1R-94 strength specimen is presented in Section 2.2.5.1. Section 2.2.5.2 presents the results of SACMA SRM 1R-94 coupon strength predictions and the predicted compressive modulus of the strength specimen.

A one-eighth symmetry model was developed for the strength specimen (Tabbed) with boundary conditions shown in Figure 2-31. The adhesive layer was made of EA 9394 with a modeled thickness of 0.013 in. The enforced displacement, u_1, was set equal to 4.5×10^{-3} in. The partitioned line to isolate the unconstrained region, labeled in Figure 2-31, is 0.1525 in from the end faces along the x-direction. This is because the test fixture support plates do not make contact with this region.

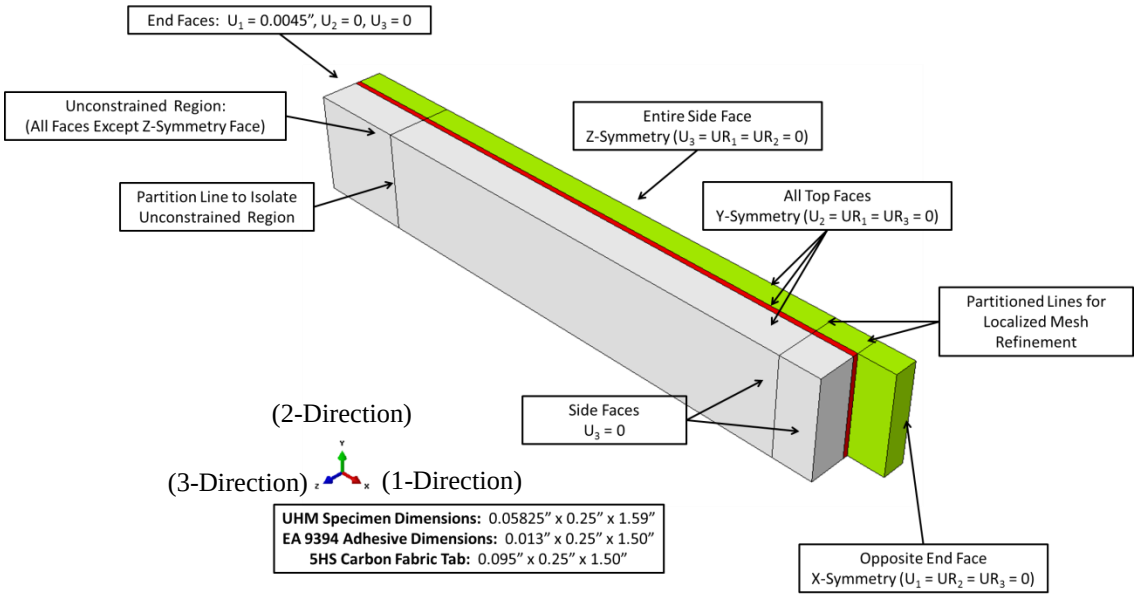

Figure 2-31: Isometric view of one-eighth symmetry model SACMA SRM 1R-94 strength specimen with boundary conditions

2.2.5.1 SACMA SRM 1R-94 Compressive Strength Specimen Convergence Study

A localized mesh-refinement was used in the model's gage section, labeled Region 1 in Figure 2-32 (a), and the part of the adhesive section, labeled Region 2 in Figure 2-32 (b). Region 2 has a length along the x-direction of 0.1 in.

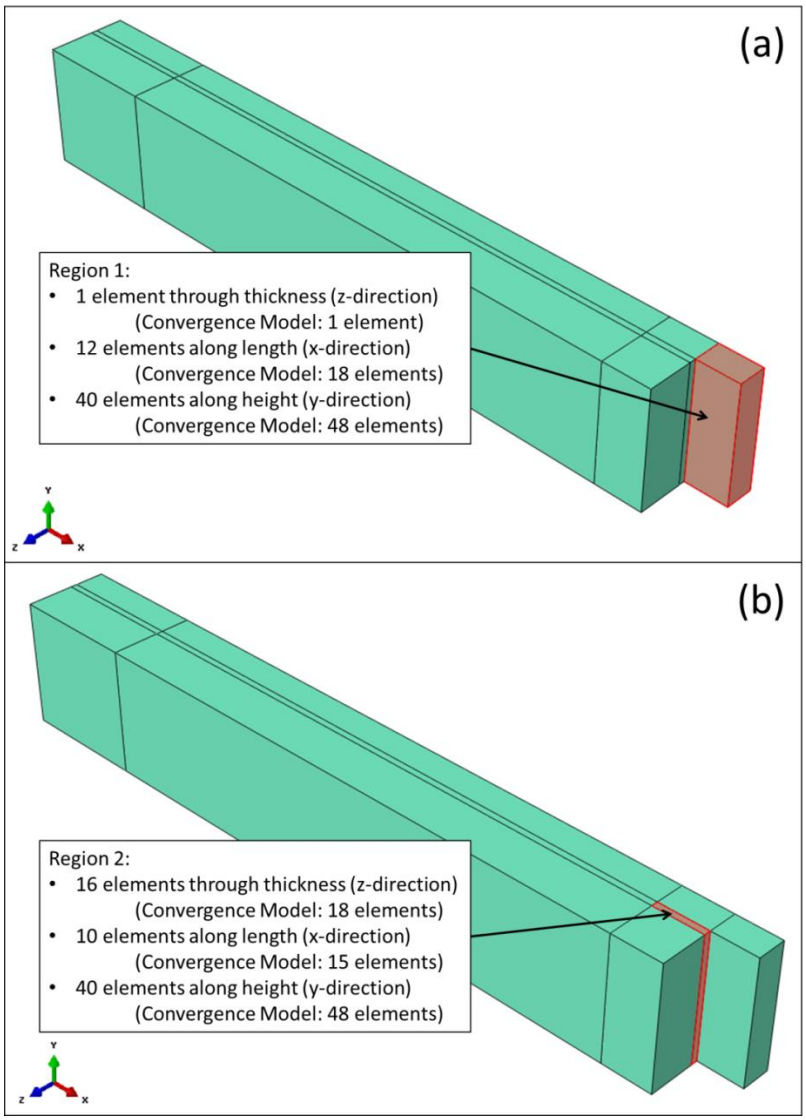

Figure 2-32: SACMA SRM 1R-94 test specimen with partitioned regions to utilize a localized mesh-refinement approach with 480 elements in region 1 (a) and 6,400 elements in region 2 (b) (Test fixture and mesh not shown)

C3D8I elements were used for the adhesive region in the convergence study. It was determined that the displacement convergence occurred with a minimum of 480 (12 x 40 x 1) elements in region 1 and 6,400 (10 x 40 x 16) elements in region 2. In total, the model consisted of 9,120 elements. The model used for a convergence comparison contained a total of 22,080 elements; Figure 2-32 (a) and (b) list the respective meshing dimensions used for the convergence model.

Figure 2-33 (a) shows the convergence displacement contour plot for the 9,120 element model and Figure 2-33 (b) shows the 22,080 element model's displacement contour plot. Table 2-8 shows the convergence comparison at the same nodal location within each specified region; the nodal locations used are labeled in Figure 2-33 (a) and (b). As shown in Table 2-9, the solution has converged with 9,120 elements as effectively no change in displacement was manifest for the more refined mesh.

Table 2-9: SACMA SRM 1R-94 specimen convergence comparison for $[(60/0/-60)_s]_2$ laminate at same nodes at ULF

9,120 Element Model		22,080 Element Model		
Region	Displacement, u_1 (in)	Region	Displacement, u_1 (in)	Difference between Displacements (%)
1	4.81×10^{-5}	1	4.83×10^{-5}	0.26
2	5.70×10^{-4}	2	5.70×10^{-4}	0.00

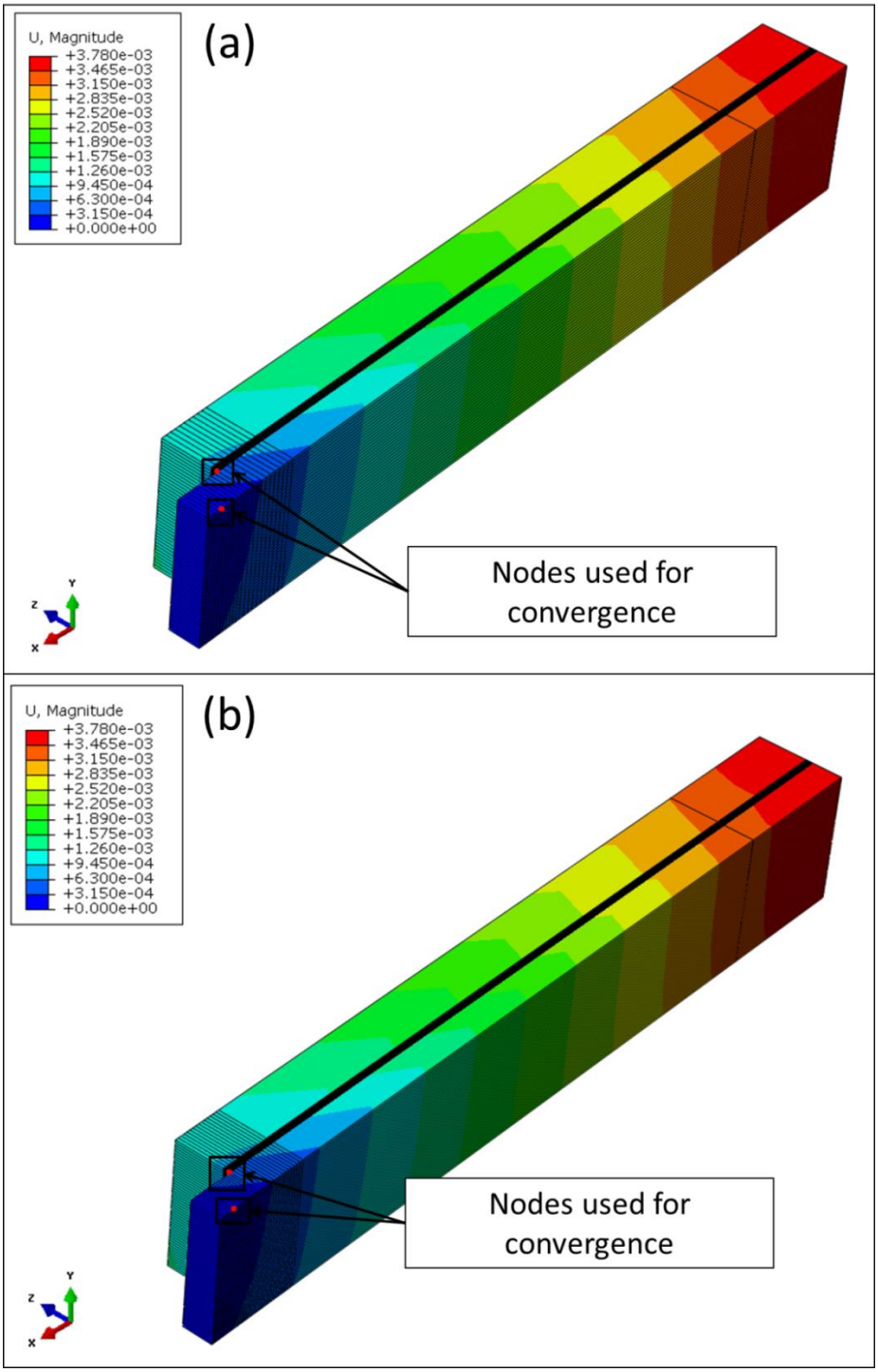

Figure 2-33: SACMA SRM 1R-94 $[(60/0/-60)_s]_2$ laminate displacement contour plot comparison at Hashin fiber compression ULF between model with 9,120 elements (a) and model with 22,080 elements (b) to demonstrate convergence with C3D8I elements used in the adhesive layer (Test fixture not shown)

A minimum element to length ratio of 60 elements/inch (Except for the cohesive zone, which can only have one element through the thickness) is adhered to in all models using cohesive elements in order to gain a sense of each modeled test specimen's behavior.

2.2.5.2 SACMA SRM 1R-94 Compressive Strength Specimen Modeling Results

The moduli and strengths are listed in Table 2-10. The FPF failure mode was fiber compression for all three response types and occurred in the laminate's second ply, which has a 0° orientation. The modeled response of the stress versus strain for the $[(+60/0/-60)_s]_2$ laminate is plotted in Figure 2-34; no experimental data exists to plot against the modeled data since the gage section is too small to fit strain gages. If the displacement data of the crosshead were to be used to extrapolate strain values, which the 2001 ASM handbook recommends against doing [12], then the compressive modulus would be calculated to be 10.24 Msi, which is too low. Using the crosshead displacement is not appropriate for tabbed specimens, since the reaction forces in the 1-direction are homogenous only at the gage section. Approximately 30 % of the SACMA SRM 1R-94 compressive load (In the 1-direction) is transferred by way of shear through the tabs when using C3D8I elements in the adhesive layer. The remaining 70 % of the compressive load is transferred through the laminate via end loading.

Table 2-10: SACMA SRM 1R-94 finite element modulus and strength results

UHM Laminate	Response Type modeled in Adhesive Layer	ULF (ksi)	Stress at FPF (ksi)	Compression Modulus (Msi) up to FPF
$[(+60/0/-60)_s]_2$	Traction Separation	49.7	35.0	14.68
	Continuum	47.8	41.9	14.49
	C3D8I Elements	47.9	42.2	14.51

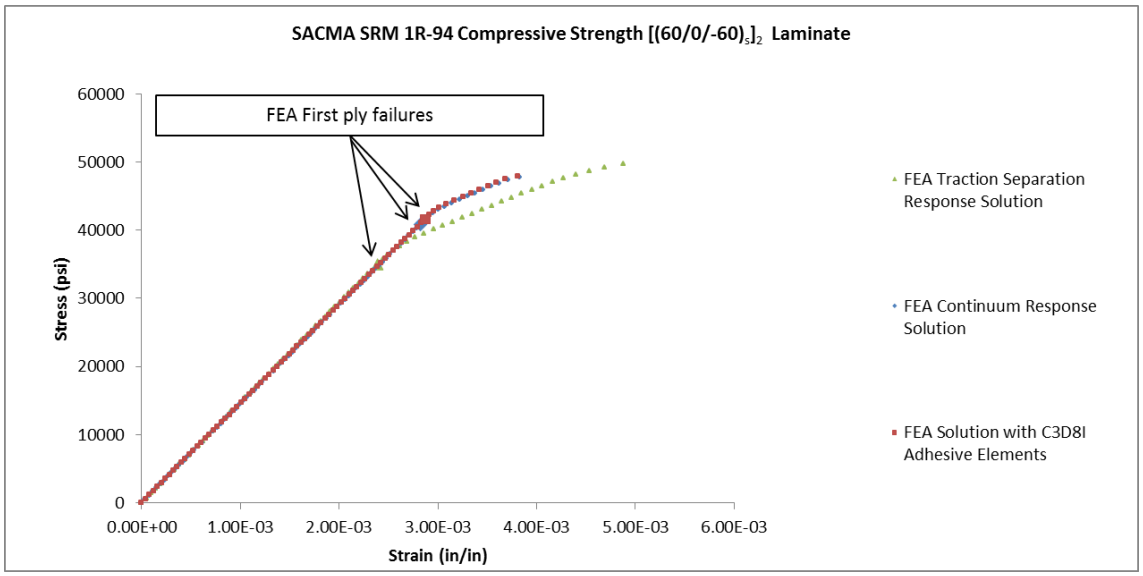

Figure 2-34: SACMA SRM 1R-94 compressive strength $[(60/0/60)_s]_2$ laminate stress versus strain response

Using element type C3D8I in the adhesive layer in order to examine the strain behavior, 16 elements were assigned through the thickness. The largest strains in the specimen at ULF occur in the adhesive layer. See Figure 2-35 for strain contour plot in the 13 plane. The largest strain in the 13 plane of the adhesive at ULF is 4.5×10^{-2} in/in.

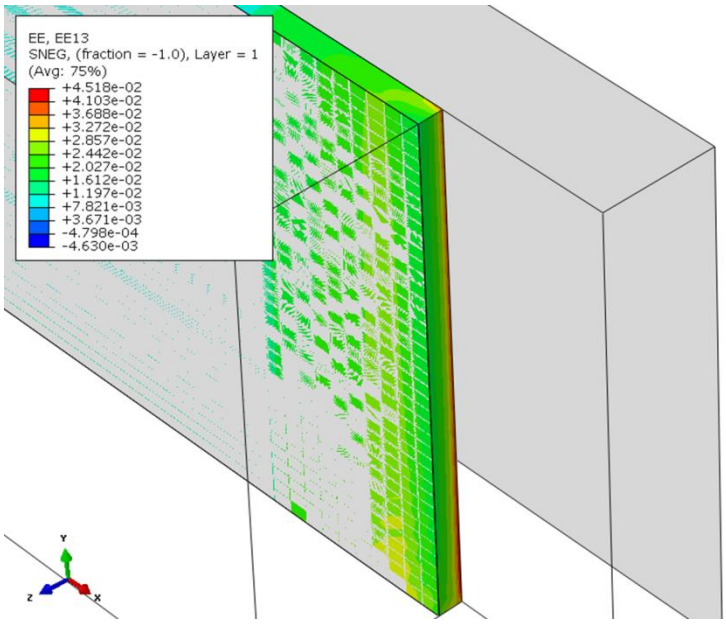

Figure 2-35: Strain contour plot in the 13 plane for one-eighth symmetry model of $[(60/0/-60)_S]_2$ SACMA SRM 1R-94 specimen with C3D8I elements in the adhesive layer (Mesh hidden)

An interesting occurrence was noted using the continuum response in the adhesive layer. For this model, the Hashin failure index at ULF at the specimen ends in the 0° plies was 0.98 in ply 2 and 0.93 in ply 5. This implies that end-crushing occurs almost immediately after ULF occurs. Figure 2-36 shows the Hashin failure index contour plot for ply 2; the bottom right hand corner of the figure is where the end-crushing nearly occurs.

The model with C3D8I elements in the adhesive layer also examined a mesh using 16 elements across the adhesive thickness. A minimum element to length ratio of 60 elements per inch was used, resulting in a total of 49,200 elements. The Hashin failure index was found to be 0.98 and 0.96 for plies 2 and 5, respectively.

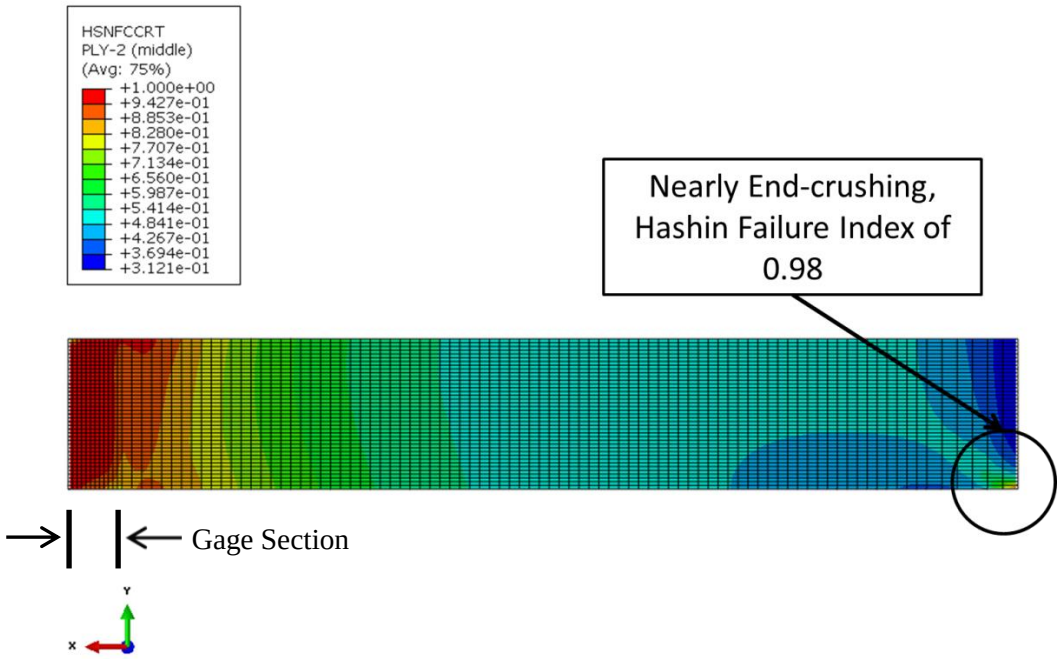

Figure 2-36: Hashin failure index contour plot for one-eighth symmetry model of $[(60/0/-60)_S]_2$ SACMA SRM 1R-94 specimen with continuum response in the adhesive layer

Overall, the largest strains in the plies occurred in the 1-direciton in the outermost 0° ply for the continuum response, traction separation response, and element type C3D8I used in the adhesive layer.

2.2.6 Classical Laminate Theory Using Matlab

It is known that the general behavior of a laminate is a function of the stacking sequence and properties of individual layers. *Classical laminate two-dimensional theory* is used to predict laminate behavior; however, governing assumptions of classical laminate theory are the laminate is thin with its lateral dimensions much larger than its thickness and is loaded in its plane only, that is, the laminate and its layers (except for their edges) are in a state of plane stress ($\sigma_z = \tau_{xz} = \tau_{yz} = 0$) [4].

Although no specific number is listed for such an assumption, such verbiage in engineering practices may call for an edge length to thickness ratio greater than 10:1. If this ratio were to be assumed for the dimensions of an elastic modulus or strength specimen for SACMA SRM 1R-94, then the *classical laminate theory* would not be appropriate for the $[(0/\pm60)_s]_2$ and $[(+60/0/60)_s]_2$ laminates, since the average width to thickness ratio is 4.29. Furthermore, it is not appropriate for ASTM D6641, since the average width to thickness ratio is 4.34.

However, granting some subjectivity, since the limitations of what is determined to be 'much larger' are not finitely defined, *classical laminate theory* is used as a benchmark to obtain a sense of the behavior of the laminates investigated. The calculated compression modulus using classical laminate theory with in-plane properties in Matlab was determined to be 14.46 Msi for both laminates. See Appendix A for Matlab code and input matrices.

2.3 Summary and Discussion

The experimental results of SACMA SRM 1R-94 and ASTM D6641 are discussed in Section 2.3.1. The results of the SACMA SRM 1R-94 compressive modulus finite element model are discussed in Section 2.3.2. The results of the ASTM D6641 finite element model using a continuum response, traction separation response, and C3D8I elements in the adhesive layer are discussed in Section 2.3.3. Section 2.3.4 presents the results of the SACMA SRM 1R-94 compression strength finite element model using the same modeling methodology from section 2.3.2. Section 2.3.5 compares and contrasts the similarities and differences between the experimental and computational results of SACMA SRM 1R-94 and ASTM D6641.

2.3.1 ASTM D6641 and SACMA SRM 1R-94 Experiments

Test results for the two angle-ply laminates $[(0/\pm60)_s]_2$ and $[(60/0/\text{-}60)_s]_2$ show that the moduli measured from both tests are statistically equivalent. Measured strengths are recorded to be significantly less for the $[(0/\pm60)_s]_2$ laminate than the $[(60/0/\text{-}60)_s]_2$ laminate, as expected from previous studies.

When using ASTM D6641, if the outermost plies of a laminate are oriented at 0°, the local stress concentrations at the ends of the specimen gage section may lead to premature failure of these primary load bearing plies, producing artificially low laminate strength results [28]. This is consistent with the $[(0/\pm60)_s]_2$ laminate experimental results from ASTM D6641.

2.3.2 Computational Results of SACMA SRM 1R-94 Compressive Modulus Specimen

For the SACMA SRM 1R-94 compressive modulus test specimens, the modeled end-crushing occurred at 2,210 με for both laminates investigated. Experimentally, the strain from 250 – 2000 με was used to determine the elastic modulus. Since the compressive modulus specimens are not to be loaded to failure, the chosen range of 250 – 2000 με was appropriate. If the more commonly used limits of 1000 – 3000 με were to be used, then the potential for end-crushing increases. Calculated modulus degradation was noted in the models for both laminates due to Poisson's effects, since the gage section is free to expand as the compressive load is increased. The predicted moduli of both laminates were within a plus or minus one standard deviation from the mean of the experimental data.

2.3.3 Computational Results of ASTM D6641

The predicted modulus for the $[(60/0/-60)_s]_2$ laminate was within one standard deviation from the mean of the experimental data. The predicted modulus for the $[(0/\pm60)_s]_2$ laminate was within two standard deviations from the mean of the experimental data. The modulus calculated using classical laminate theory in Matlab demonstrated the same trend, even though the specimen lateral dimension wasn't substantially larger than the thickness dimension as dictated by a governing assumption. The predicted strengths for the $[(60/0/-60)_s]_2$ laminate were under-predicted. The predicted compression modulus and strengths using a traction separation response, a continuum response, and C3D8I elements in the adhesive layer yielded statistically equivalent results for both laminates.

The modeled FPF occurred in the outermost 0^o ply due to fiber compression at the gage section where the adhesive and the tab meet the UHM laminate for both specimens. The modeled ULF occurred in the 0^o ply due to fiber compression closest to the laminate center near the x-symmetry boundary condition specified in Figure 2-18. This is consistent with the principle of superposition since a load path from the forces due to the bolt torqueing and forces due to the crosshead displacement on the tab vectorially add together. Figure 2-37 shows a generalized load path of the UHM laminate consistent with the modeled FPF and ULF seen throughout this investigation.

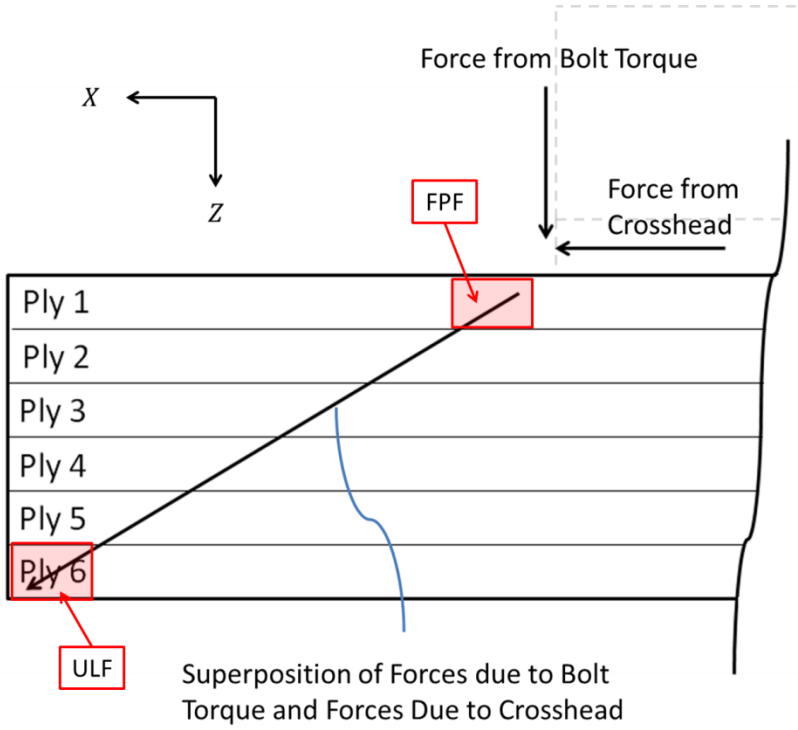

Figure 2-37: One eighth symmetry model's layup of UHM laminate with generalized load path for a $[(0/\pm 60)_s]_2$ laminate

It was determined that approximately 78% of the ASTM D6641 load is transferred through the test fixture end, 12% of the load is transferred through the tab ends, and 10% of the load is transferred through the UHM laminate when using C3D8I elements in the adhesive layer. This implies that during experimentation, assuming the tabs are flush with the UHM laminate and the test fixture, end-crushing is not likely to occur as a specimen failure mode.

ASTM D6641 [28] states that while tapered tabs would be potentially beneficial in reducing stress concentrations in the specimen at the tab ends, they increase the effective unsupported length (gage length) of the specimen, increasing the possibility of inducing specimen buckling. Thus, untapered (square-ended) tabs are recommended.

2.3.4 Computational Results of SACMA SRM 1R-94 Compressive Strength Specimen

The predicted moduli of the $[(60/0/-60)_s]_2$ laminate was within one standard deviation of the respective compressive modulus specimen's experimental data. The strength was under-predicted for all adhesive response types. The traction separation response predicted a lower FPF and a higher ULF than the continuum response and C3D8I elements in the adhesive layer. Approximately 30 % of the SACMA SRM 1R-94 specimen load is transferred through the tabs when using the traction separation response, while the remaining 70% is transferred through the UHM laminate. The failure index for end-crushing indicated that end-crushing almost occurs at the same time as ULF. This implies that for the laminates investigated, initiation of end-crushing could occur using SACMA SRM 1R-94.

The model using C3D8I elements in the adhesive layer had a nearly identical stress versus strain response as the model using a continuum response.

2.3.5 Similarities and Differences of SACMA SRM 1R-94 and ASTM D6641 Test Methods

The largest ply (in local material coordinate system) compressive strains for both compression tests occur in the 0° plies for both laminates. The mean of the experimental SACMA SRM 1R-94 compressive strength specimen demonstrated a strength 11.9 % greater than the experimental ASTM D6641 strength for the $[(60/0/60)_s]_2$ laminate. Notable differences between the two test standards, aside from loading methods (Shear and end), are the tab to gage section ratios and the clamping pressure due to bolt torque.

Based on the predicted failure modes investigated for both test methods, SACMA SRM 1R-94 likely predicts strength values closer to actual laminate strengths than ASTM D6641.

However, for the laminates investigated, SACMA SRM 1R-94 could incur the initiation of end-crushing.

Chapter 3

Experimental and Computational Procedures for Test Methods to Determine Fracture Toughness

In this chapter experimental and computation procedures for the fracture toughness of modes I and II are discussed in Sections 3.1 and 3.2, respectively. Section 3.1 summarizes ASTM D5528 and the end-notched flexure tests used to determine the fracture toughness of mode I and mode II, respectively. Section 3.2 summarizes FEA techniques used to model the fracture toughness of ASTM D5528 and the end-notched flexure test. Section 3.3 compares the experimental and computation results.

3.1 Test Methods – ASTM D5528 and Mode II End-Notched Flexure

Section 3.1.1 gives an overview of the three fracture modes and the tests used to determine the fracture toughness of a specific mode. Sections 3.1.2 and 3.1.3 discuss the experimental test methods used to determine the fracture toughness for modes I and II, respectively. Data reduction methods are discussed in Section 3.1.4.

3.1.1 Fracture Toughness Overview

Interlaminar delamination occurs in three modes; mode I exhibits peeling, mode II exhibits sliding through-the-thickness shear, and mode III exhibits out-of-plane tearing. Figure 3-1 shows fracture modes I, II, and III. The resistance to delamination growth is defined in terms of interlaminar fracture toughness. Interlaminar fracture toughness has three forms corresponding to

the three delamination modes and is measured by the strain energy release rate (G_I, G_{II}, G_{III}), which is the energy dissipated per unit area of delamination growth [4].

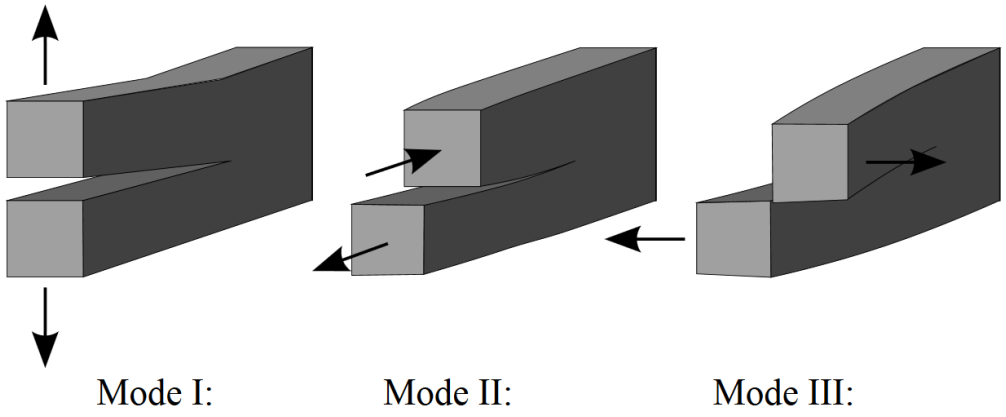

Figure 3-1: Fracture Modes I, II, and III. Mode I exhibits peeling, mode II exhibits through-the-thickness shear, and mode III exhibits out-of-plane tearing [39]

Tests to determine the mode I and mode II interlaminar fracture toughness were conducted on an intermediate modulus carbon fiber/epoxy composite. The specific material system investigated for this research is proprietary so further details cannot be presented at this time. The fracture toughness test methods employed include ASTM D5528 to determine G_I and a U.S. Government provided end-notched flexure (ENF) compliance calibration test method to determine G_{II}. ASTM D5528 makes use of a double cantilever beam (DCB) specimen under two different loading schemes; see Figure 3-2 (a) and (b) where,

h:	thickness of DCB specimen
a_o:	initial delamination length measured from the applied loads
b:	width of DCB specimen
L:	length of DCB specimen

In Figure 3-2 (a), opening forces are applied at the piano hinges and in Figure 3-2 (b), loading blocks are bonded to the specimen and opening forces are applied to the holes in the blocks. Piano hinges, as seen in Figure 3-2 (a), were used in this study. A generic test setup for piano hinges is shown in Figure 3-3.

The end notched flexure test makes use of a similarly constructed DCB specimen from ASTM D5528, but consists of different dimensions, loading conditions, and boundary conditions; see Figure 3-4 where,

t:	thickness of ENF specimen
a:	initial delamination length
B:	width of ENF specimen
P:	distributed load
L:	half the length between the reaction pins of the ENF specimen

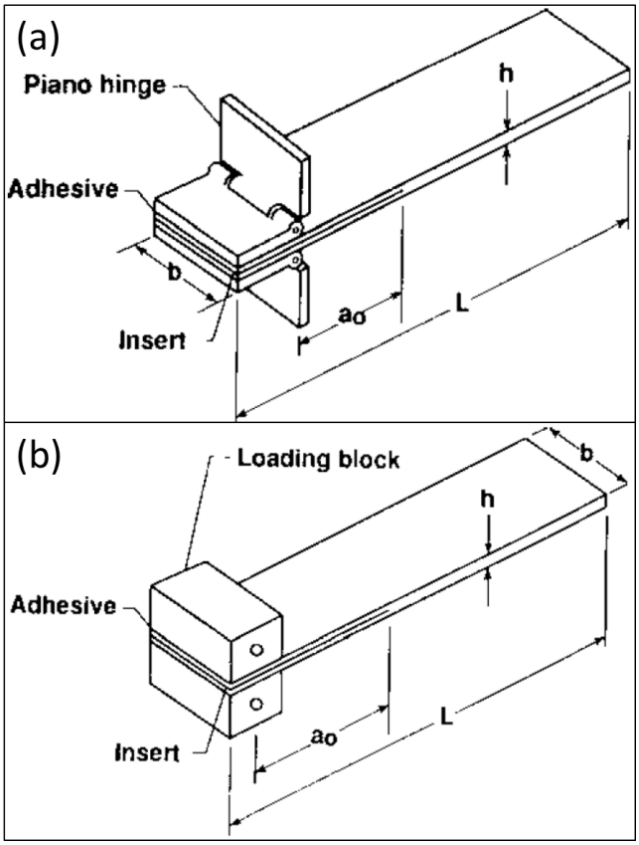

Figure 3-2: Double cantilever beam (DCB) specimen (a) with piano hinges, (b) with loading blocks specifying dimensions and boundary conditions [16]

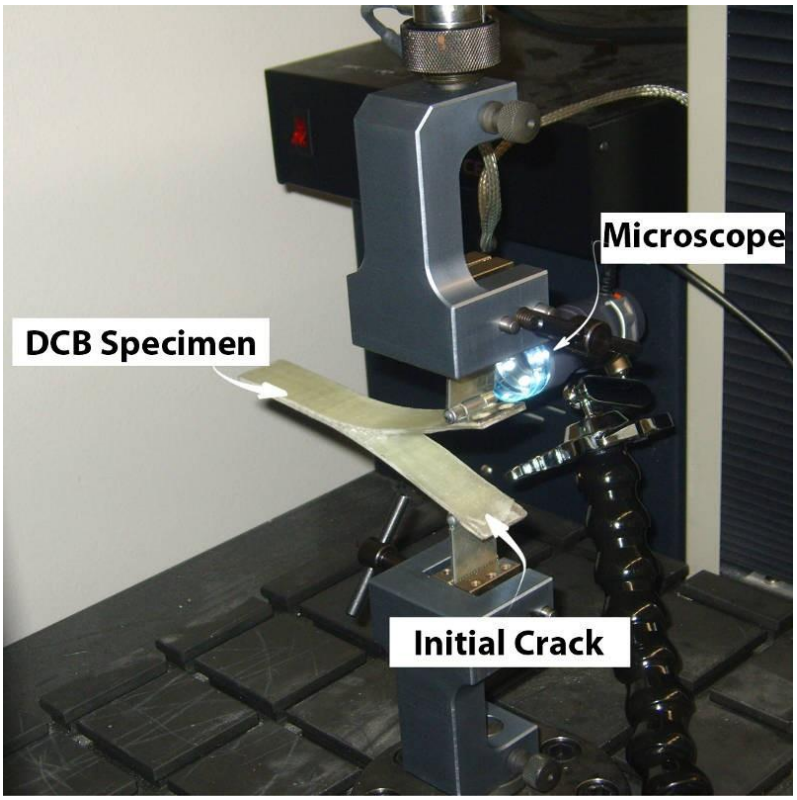

Figure 3-3: Generic test setup of ASTM D5528 showing the test specimen, initial crack, and the microscope used to detect the onset of delamination [40]

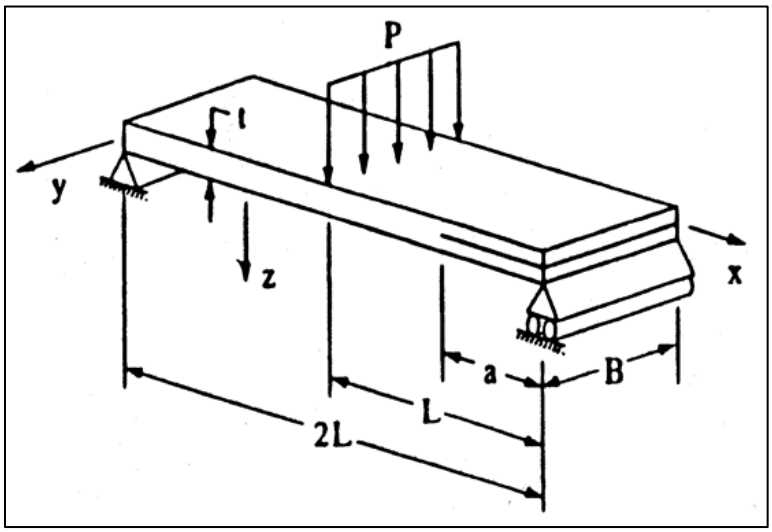

Figure 3-4: End notched flexure test method diagram specifying dimensions and boundary conditions [41]

3.1.2 Experimental Test Method – ASTM D5528

The use of ASTM D5528 is typically limited to unidirectional carbon and glass fiber tape laminates with brittle and tough single-phase polymer matrices. The strain energy release rate (SERR) is defined in equation (62)

$$G = -\frac{1}{b}\frac{dU}{da} \tag{62}$$

where,

G:	SERR
U:	total elastic energy in the test specimen
du:	differential increase in strain energy
b:	specimen width
da:	differential increase in delamination length

The DCB diagram in Figure 3-2 consists of a rectangular, uniform thickness, unidirectional laminated composite specimen containing a non-adhesive insert, polytetrafluoroethylene (PTFE), also known as Teflon, with a thickness no greater than 5.0×10^{-4} in, on the midplane that serves as a delamination initiator. The piano hinges are opened by controlling the crosshead movement while the load and delamination length are recorded. The hinges are bonded with a room-temperature cure adhesive; the hinge dimensions are 1 in wide x 1 in (Length by width). A record of the applied load versus opening displacement is recorded. Instantaneous delamination front locations are marked on the chart at intervals of delamination growth [16].

Test specimens must contain an even number of plies with delamination growth occurring in the 0° direction. In this study, 10-ply specimens were tested with an average ply thickness of 2.25×10^{-2} in. The specimen thickness variation cannot exceed 0.004 in. The specimens used were 6.0 in long and 1.0 in wide. The initial delamination length, measured from the load line to the end of the insert, is 2.0 in.

The specimen is loaded at 0.20 in/min**.** The load and deflection values corresponding to onset of delamination growth were assessed via visual detection as viewed with a 40X microscope and seen in Figure 3-3. The maximum load of the piano hinges seen in Figure 3-2 (a) can be estimated using equation (63):

$$P_{max} = \frac{b}{a}\sqrt{\frac{h^3 E_{11} G_{I_C}}{96}} \tag{63}$$

where G_{I_c} is the anticipated value of the interlaminar fracture toughness for mode I. The average load at the onset of G_{I_C} was calculated to be 32.25 lb using the initial insert crack length for *a*.

Three methods have been developed to calculate G_{I_c} values which differ by no more than 3.1 %. The modified beam theory, the method used to determine G_{I_c} in this study, yields the most conservative values of G_{I_c} [16]. The Modified Beam Theory Method uses equation (64)

$$G_I = \frac{3P\delta}{2ba} \tag{64}$$

where, δ is the load point displacement. δ is defined in Figure 3-5 as the distance between the top and bottom separations.

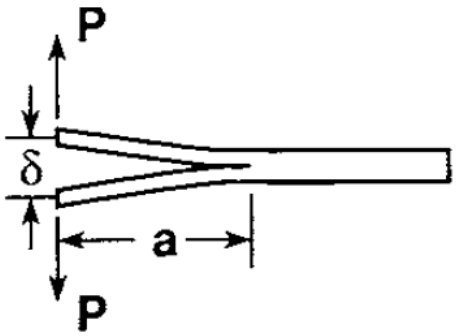

Figure 3-5: DCB test load displacement representation defining δ [16]

A correction factor, as listed in the appendices A1, A1.1, and A1.2.1 of ASTM D5528 was used to account for large deflections. This correction factor, *F*, is multiplied by G_I and is given as equation (65):

$$F = 1 - \left(\frac{3}{10}\right)\left(\frac{\delta}{a}\right)^2 - \left(\frac{3}{2}\right)\left(\frac{\delta t}{a^2}\right) \quad (65)$$

where *a* and *t* are defined in Figure 3-6.

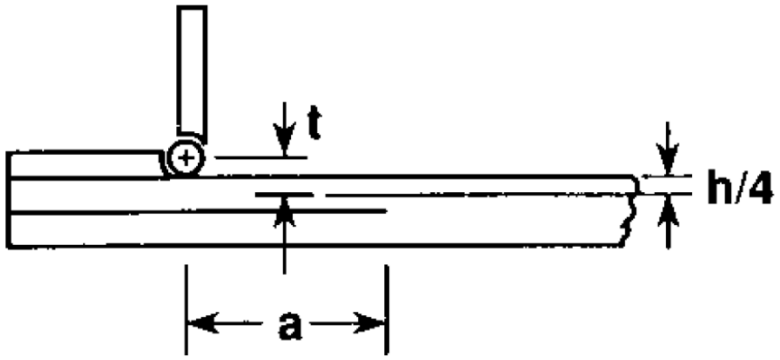

Figure 3-6: Parameters defined for use in the correction factor, *F*, equation (65) [16]

In this study, using the modified beam theory described in the previous paragraphs, G_{I_C} for propagation is calculated as the mean of all G_{I_C} values after the onset G_{I_C} value. Therefore, onset G_{I_C} is not included in mean propagation G_{I_C} value.

The Compliance Calibration Method uses equation (66)

$$G_I = \frac{nP\delta}{2ba} \quad (66)$$

The log ($\frac{\delta_i}{P_i}$) versus log (a_i) is plotted using visually observed delamination onset values and all the propagation values. A best least squares fit is generated for the plot, and n is equal to the slope of the best least squares fit.

The Modified Compliance Calibration Method uses equation (67)

$$G_I = \frac{3P^2C^{2/3}}{2A_1bh} \quad (67)$$

where,

C: $\frac{\delta}{P}$

A_1: the slope of a best least squares fit of a plot of $\frac{a}{h}$ versus $C^{1/3}$

For the experimental determination of mode I fracture energy, as the delamination grows from the insert, a fracture resistance develops when the calculated G_{I_c} first increases montonically, then stabilizes with further delamination growth. The reason for this observation is due to fiber bridging [16]. "Fiber bridging occurs when fibers are pulled from one side of the delamination plane to the other [42]." This occurs as a result of growing a delamination between two 0° unidirectional plies. Fiber bridging does not occur between most ply layups, since most composite layups consist of dissimilar consecutive ply orientations. Therefore, propagation values calculated beyond the end of the implanted insert are questionable [16].

3.1.3 Experimental Test Method – End-Notched Flexure

A three point end-notched flexure test specimen is used to characterize the interlaminar fracture energy for mode II, G_{II_c}. A similar specimen to that used in ASTM D5528 is used with several differences. The specimen length is 8.0 in and the width is nominally 1.0 in. No piano hinges are used and the same type of insert is used, except its length is 2.25 in. A 40X microscope is used to assess the load and deflection values corresponding to the onset of delamination growth. The span between the reaction supports in Figure 3-4, *2L*, is 5.0 in. The applied load at the span's midpoint is 0.2 in/min. The center load's point displacement is measured with a linear variable differential transformer or a deflectometer located on the bottom face of the test specimen.

An extra specimen that is not part of the statistical population is used to calibrate the load. The measured crack length from the reaction pin is 1.75 in. After the load is applied, the load at the onset of delamination growth is recorded. The crack is allowed to propagate 0.1 in,

and is then removed and examined for uniform crack growth. If crack growth is uniform, equation (68) is used as a calibration test load:

$$P_{cal} = 0.7P_{a=1.75in} \tag{68}$$

If the cracks are not uniform, then a second test specimen is used and inverted such that the bottom face is oriented to be the top face. If the cracks are uniform, equation (68) is used; if the cracks are not uniform, equation (69) is used:

$$P_{cal} = \left[\frac{0.7(P_{1st}+P_{2nd})}{2}\right]_{a=1.75in} \tag{69}$$

The first specimen of the statistical population is then loaded such that a_o, the initial crack length, is equal to 0.75 in. The load and deflection data are recorded until P_{cal} is reached. The specimen is then repositioned such that a_o is equal to 1.0 in. Again, the load and deflection data are recorded until P_{cal} is reached. This process is repeated for crack length increments of 0.25 in until a_o is equal to 1.75 in. Figure 3-7 shows the positional incrementation for calibration.

After the completion of the five calibrations, the specimen is repositioned such that a_o is equal to 1.25 in. The specimen is then loaded until failure while monitoring onset of delamination growth. The specimen has failed if the crack has reached the loading pin.

A compliance calibration approach, based on empirical data, is used to calculate G_{II_c} values. See equation (70) [41]:

$$G_{II_c} = \frac{3mP^2a^2}{2b} \tag{70}$$

where m is the slope of the compliance values versus the cube of the respective crack lengths.

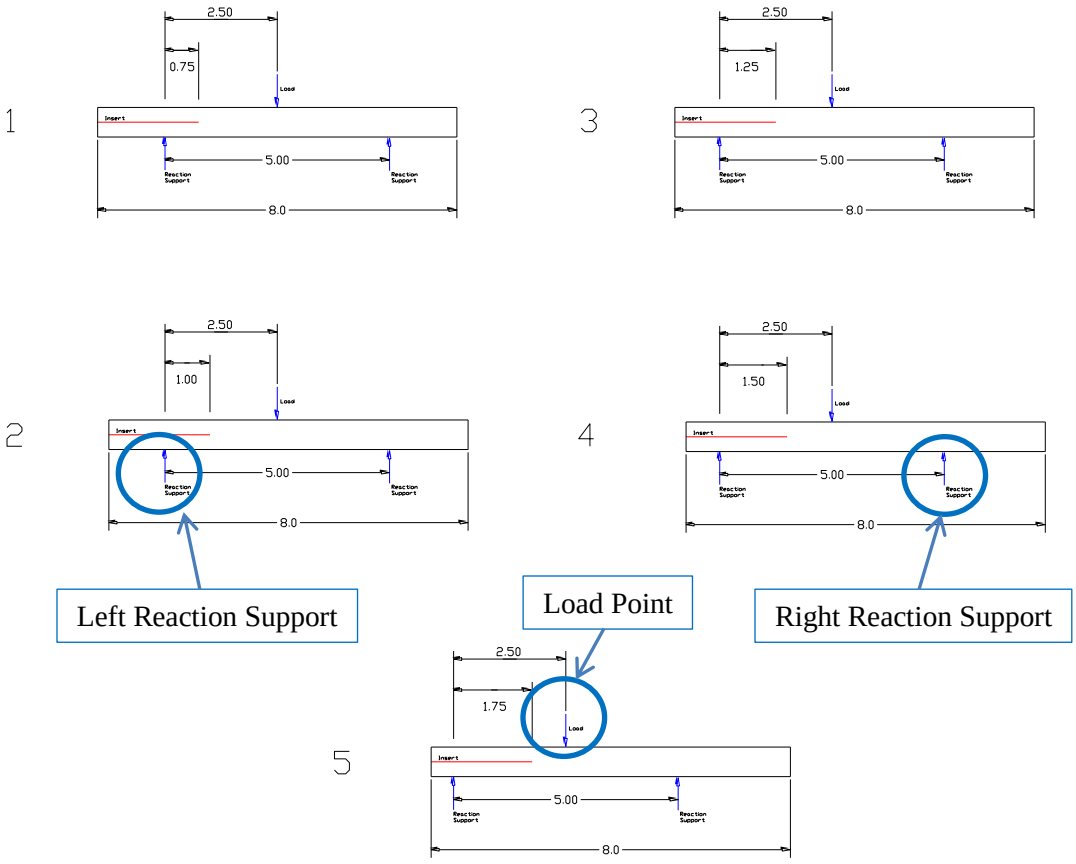

Figure 3-7: ENF compliance calibration specimen positioning [41]. Note insert designated with red line, loading occurs midway between reaction supports

3.1.4 Data Reduction Method for Analysis Comparison

Figures 3-8 and 3-9 show the experimental load versus displacement plots of the $[0]_{10}$ IM carbon/epoxy laminate for ASTM D5528 and the end-notched flexure test, respectively. Critical SERR results for the $[0]_{10}$ laminate for modes I and II are presented in Table 3-1.

The investigated material system displayed substantial fiber bridging, especially at the crack tip. There were no major "jumps" or "crack-runners" associated with major bridging spontaneously letting go; the bridged fibers gently pulled out of the surfaces after significant

crack growth beyond the initial bridge. Loose fibers from bridging were noted on the post-test crack plane.

The propagation fracture toughness is substantially greater than the onset fracture toughness for mode I. This is likely due to fiber bridging; the average onset load required for delamination is calculated to be 32.25 lb using equation (63) and is circled in Figure 3-8.

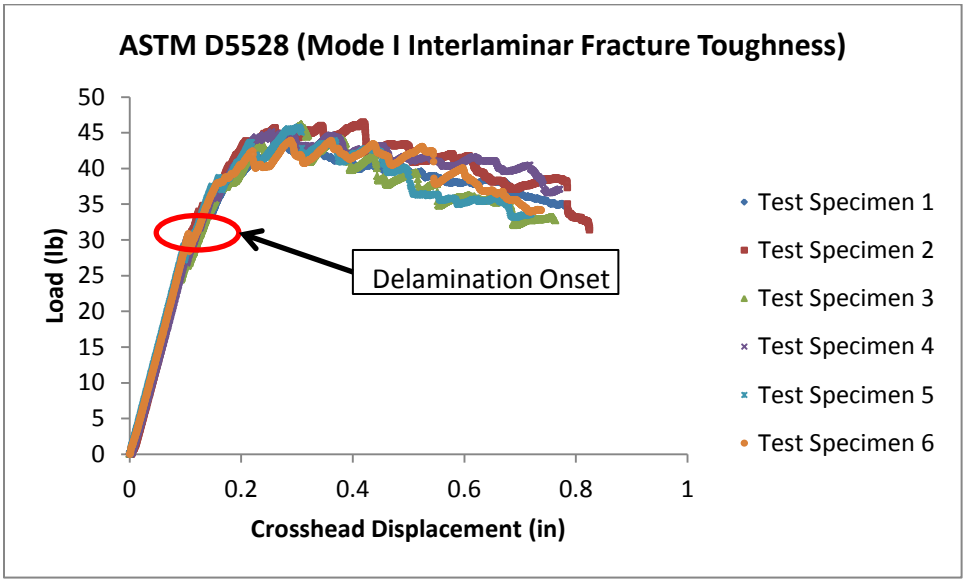

Figure 3-8: ASTM D5528 load versus displacement response of $[0]_{10}$ IM carbon/epoxy laminate

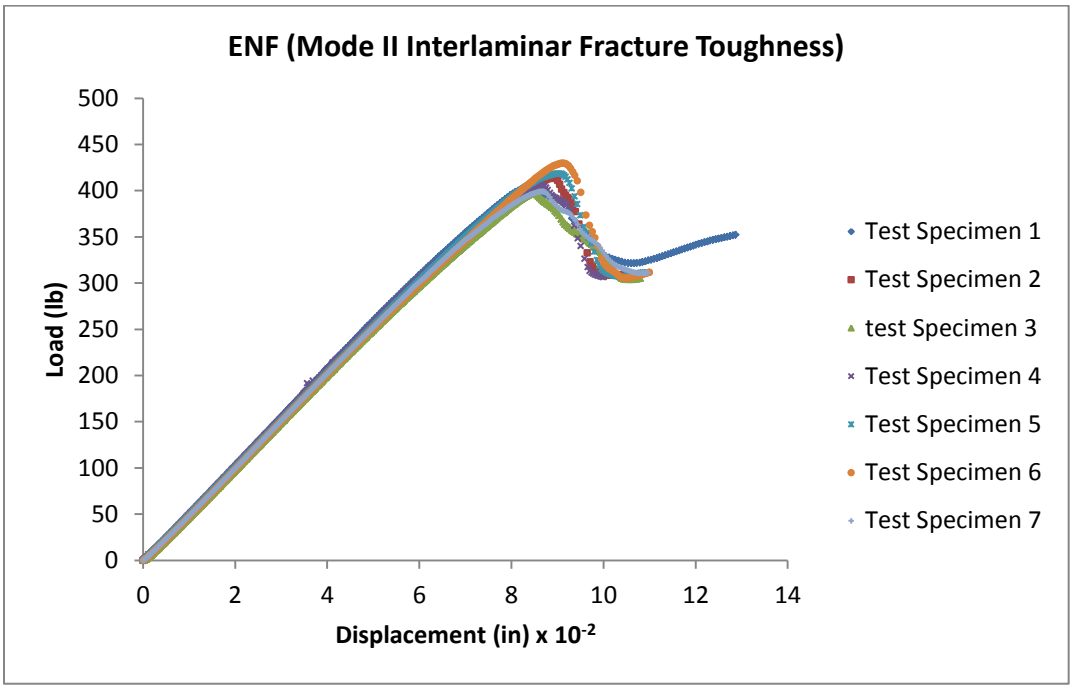

Figure 3-9: End-notched flexure load versus displacement response of $[0]_{10}$ IM carbon/epoxy laminate

Table 3-1: Interlaminar fracture toughness values for IM carbon/epoxy laminate

	G_{I_c} **Onset** $\left(\frac{in\ lb}{in^2}\right)$	G_{I_c} **Propagation** $\left(\frac{in\ lb}{in^2}\right)$	G_{II_c} **Onset** $\left(\frac{in\ lb}{in^2}\right)$	G_{II_c} **Pmax** $\left(\frac{in\ lb}{in^2}\right)$
Average	1.695	6.462	4.592	6.246
Standard Deviation	0.201	0.378	0.366	0.343

3.2 Computational Procedures – Finite Element Analysis

Section 3.2.1 defines the material properties used for the finite element analysis. The virtual crack closure technique, a feature built into Abaqus, is explained with an example in Section 3.2.2. Sections 3.2.3 and 3.2.4 describe the modeling methodology and predicted results of the ASTM D5528 and the ENF tests, respectively.

3.2.1 Material Properties

The $[0]_{10}$ laminate was investigated using Abaqus. The average elastic properties used in the analysis are listed in Table 3-2. The experimentally determined fracture toughness values are listed in Table 3-1 in Section 3.1.4.

Table 3-2: Average elastic lamina properties of IM carbon/epoxy material system

E_{11} = 20.69 Msi
E_{22} = 1.195 Msi
E_{33} = 1.195 Msi
ν_{12} = 0.37
ν_{13} = 0.37
ν_{23} = 0.37
G_{12} = 0.69 Msi
G_{13} = 0.69 Msi
G_{23} = 0.34 Msi

3.2.2 Virtual Crack Closure Technique

The virtual crack closure technique (VCCT) is a feature built into Abaqus that makes use of linear elastic fracture mechanics. The condition for crack propagation is based on Griffith's principle as shown in equation (71):

$$G \geq G_c \tag{71}$$

where G is an energy release rate term for a specific mode and G_c is an a critical energy release rate term for the same corresponding mode. During crack propagation, the elastic strain energy released, ΔU, used to create a new surface area can be calculated as the work required to close a crack and is defined in equation (72):

$$\Delta U = W_{closure} \tag{72}$$

"VCCT is based on the assumption that the strain energy released when a crack is extended by a certain amount is the same as the energy required to close the crack by the same amount [32]." Equation (72) is referred to as the Irwin principle. The condition for crack propagation can be defined using equation (73) [43]:

$$\frac{\frac{W_{closure}}{\Delta A}}{G_c} \geq 1 \tag{73}$$

where *A* is one half of the surface area created.

An example of how Abaqus utilizes the VCCT for mode I is presented in Figure 3-9; nodes 2 and 5 will start to release when equation (74) is met [32]:

$$\frac{G_I}{G_{Ic}} = \frac{1}{2}\left(\frac{v_{1,6}F_{v,2,5}}{bd}\right)\frac{1}{G_{Ic}} \geq 1 \tag{74}$$

where,

G_I:	energy release rate
G_{Ic}:	critical energy release rate
b:	width
d:	length of the elements at the crack front
$v_{1,6}$:	vertical displacement between nodes 1 and 6
$F_{v,2,5}$:	vertical force between nodes 2 and 5

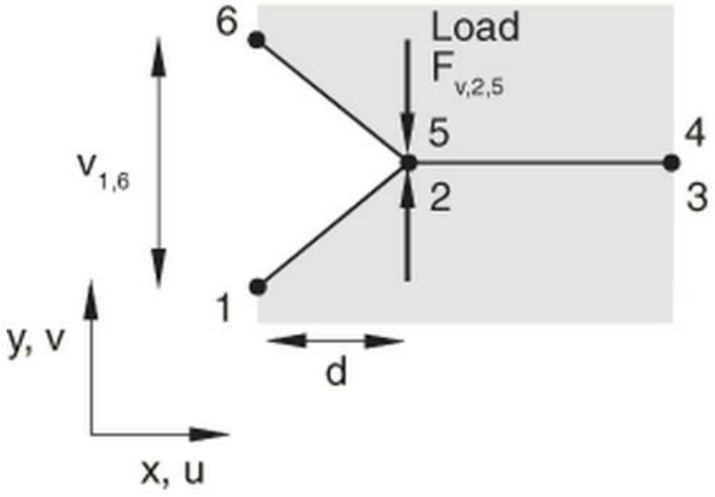

Figure 3-9: VCCT example used to demonstrate mode I fracture [32]

Using modes I, II, or III, a generalized equation can be used for fracture criterion as defined in equation (75) [32]:

$$\frac{G_{equiv}}{G_{equivC}} \geq 1.0 \qquad (75)$$

where,

G_{equiv}: equivalent SERR calculated at node
G_{equivC}: "critical equivalent SERR calculated based on the user-specified mode-mix criterion and the bond strength of the interface [32]"

3.2.3 ASTM D5528 FEA Modeling

The boundary conditions and dimensions used to model ASTM D5528 are shown in Figure 3-10. Four elements span the thickness in Figure 3-10, 75 elements span the length of the one inch region, 150 elements span the length of the two inch region, and 225 elements span the length of the three inch region in Figure 3-10. A total of 900 CPE4I elements were used in the model. The designation CPE4I represents a 4-node bilinear plane strain quadrilateral with incompatible modes. The bonded interface represents the region without a PTFE insert.

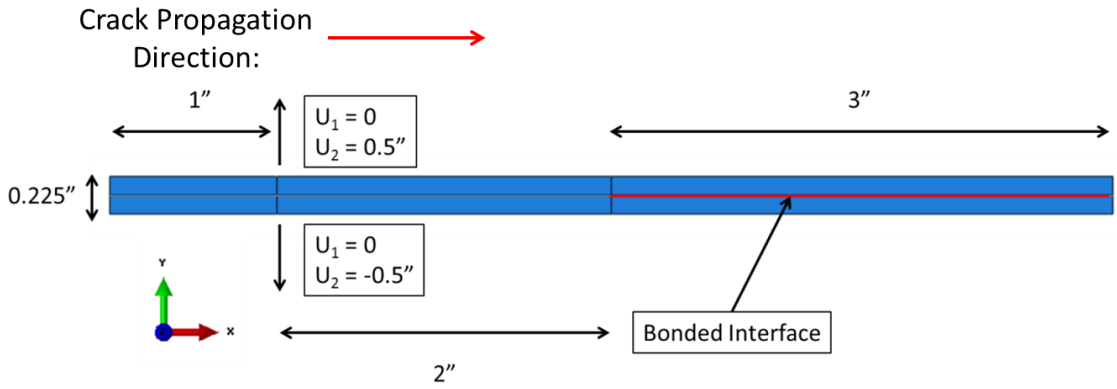

Figure 3-10: ASTM D5528 FEA boundary conditions and dimensions

The model was constructed as an assembly; a disassembled assembly is shown in Figure 3-11. Figure 3-11 defines the master surface as the top of the bottom section and the slave surface is defined as the bottom of the top section. An initial and maximum time increment size of 0.004 and a minimum increment size of 10^{-50} with a time period of 1 were used.

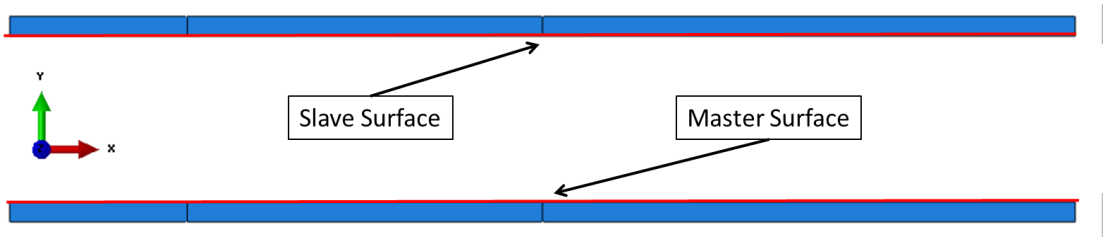

Figure 3-11: ASTM D5528 master surface and slave surface defined at the midplane

The modeled mode I responses of the load versus displacement for the $[0]_{10}$ IM carbon/epoxy laminate are shown in Figure 3-12 for the predicted FEA solutions plotted against the experimental data sets. Two FEA solutions were predicted. One solution used the mode I onset critical SERR. The second solution used the mode I propagation critical SERR. The author conjectures that all experimental data would fall between the bounds defined by the fracture energy propagation solution and the fracture energy onset solution for mode I if fiber bridging did not occur. However, a user modeling such behavior could add a standard deviation to the propagation G_{Ic} used in an FEA model to bound all expected behavior. Furthermore, if the piano hinges were modeled, the slope of the curve in Figure 3-12 would be even closer to the average slope of the experimental data.

A resistance curve "is a result of increased energy dissipation in the plastic zone that grows with crack extension [44]." A resistance curve, also referred to as an r-curve, is a plot of the fracture toughness versus the crack length. Figure 3-13 shows the predicted resistance curve using VCCT for G_{Ic} onset. Note that the specimen insert spans up to 3 in. Figure 3-14 shows an

enlarged view of the r-curve after crack propagation. Figure 3-15 shows an enlarged view of the predicted r-curve using VCCT for G_{Ic} propagation. Fiber bridging behavior is not captured in either Figure 3-14 or Figure 3-15, since both figures resemble step-function-like behavior.

Since fiber bridging does not occur in typical composite layups, assuming the stacking sequence does not consist of all zeros, VCCT is likely capable of capturing all fracture behavior for mode I if a boundary is created by using G_{Ic} onset and G_{Ic} propagation.

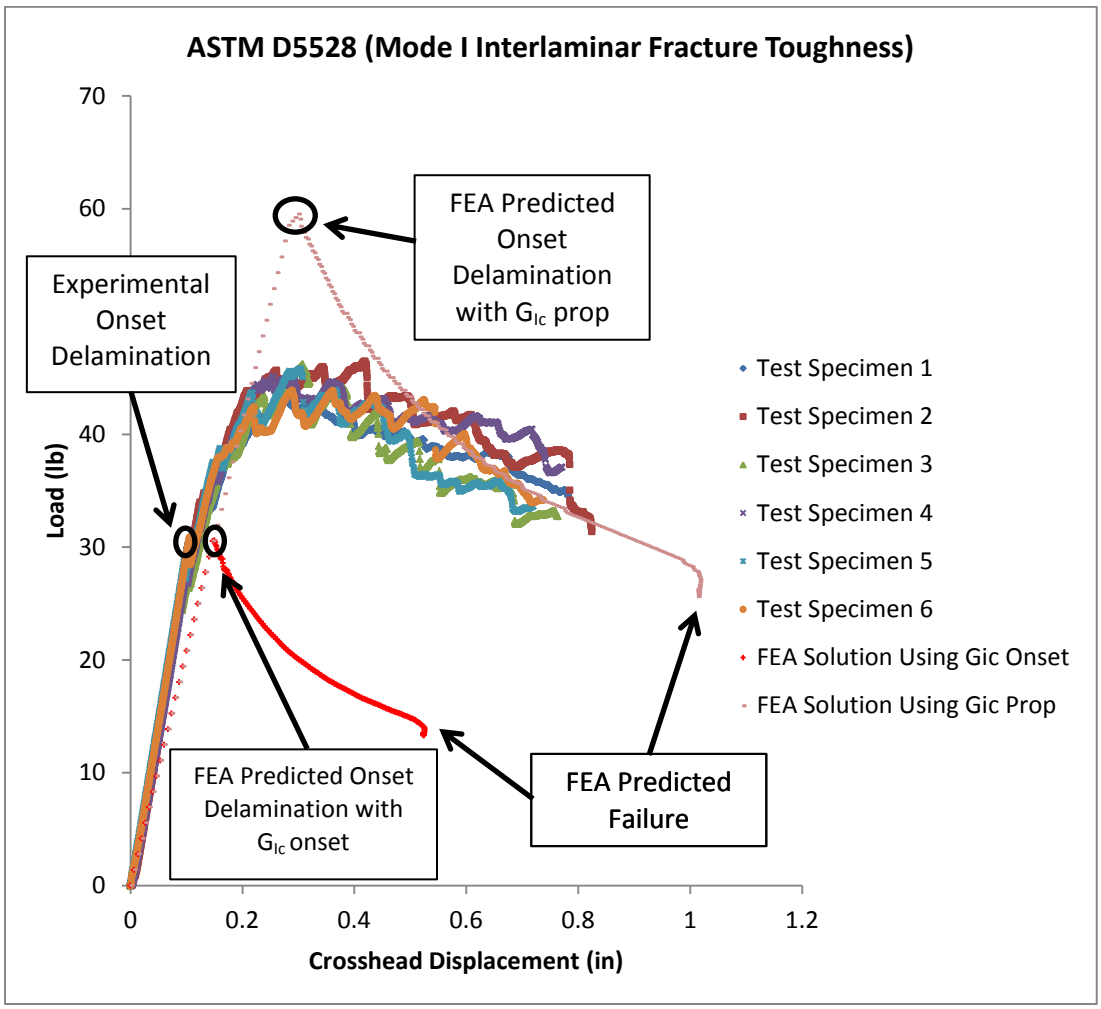

Figure 3-12: ASTM D5528 load versus displacement response of $[0]_{10}$ IM carbon/epoxy laminate for FEA solutions and experimental data

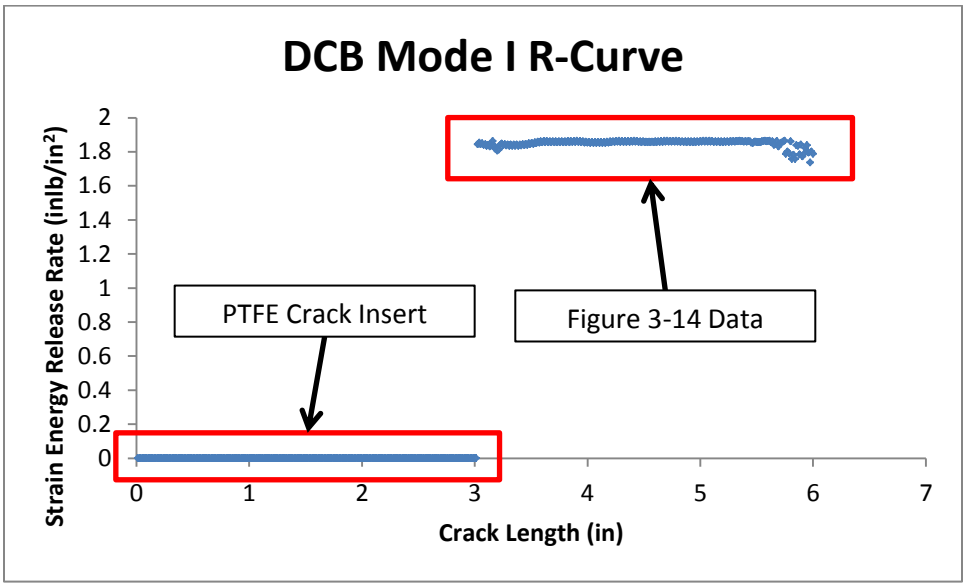

Figure 3-13: R-curve of DCB mode I for $[0]_{10}$ IM carbon/epoxy laminate using VCCT and G_{Ic} onset

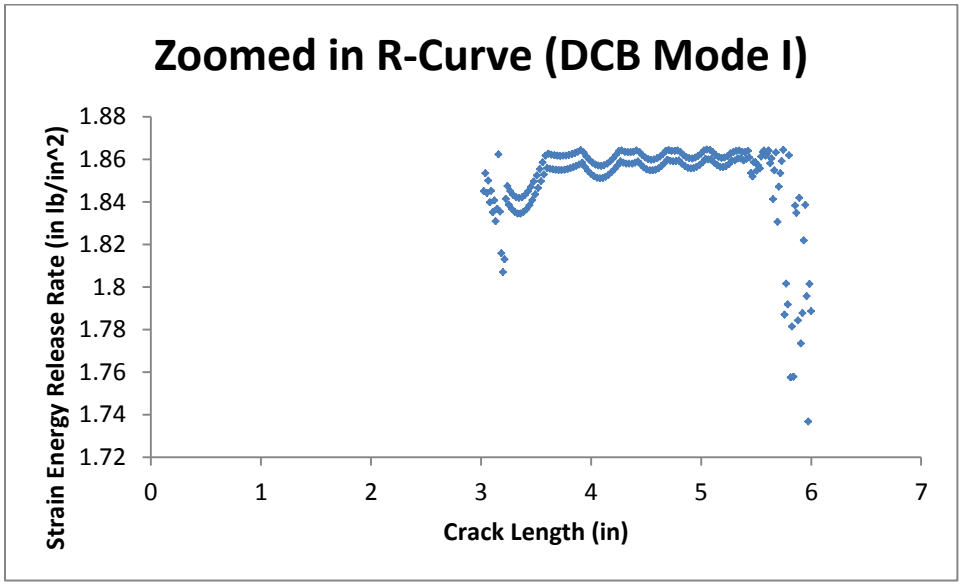

Figure 3-14: Zoomed in r-curve of DCB mode I for $[0]_{10}$ IM carbon/epoxy laminate using VCCT and G_{Ic} onset

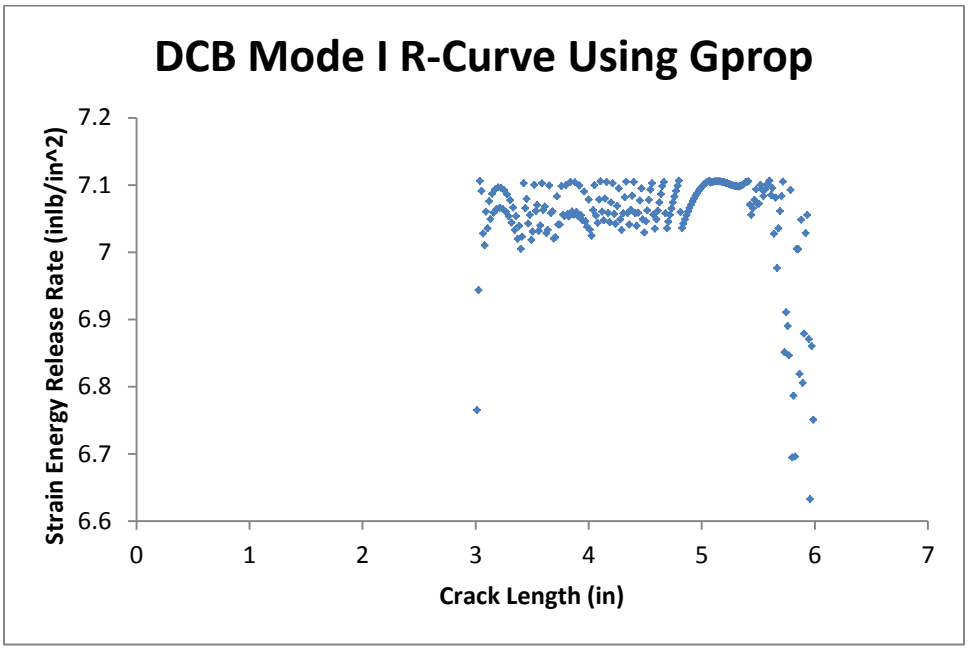

Figure 3-15: Zoomed in r-curve of DCB mode I for $[0]_{10}$ IM carbon/epoxy laminate using VCCT and G_{Ic} propagation (PTFE crack insert data points omitted)

3.2.4 ENF FEA Modeling

The boundary conditions and dimensions used to model the ENF test are shown in Figure 3-16. Four elements span the thickness in Figure 3-16, 100 elements span the length of the one inch region, 125 elements span the length of the 1.25 in regions, 250 elements span the length of the 2.5 in region, and 200 elements span the 2 in region in Figure 3-16. A total of 1,600 CPE4I elements were used in the model. The bonded interface represents the region without a PTFE insert.

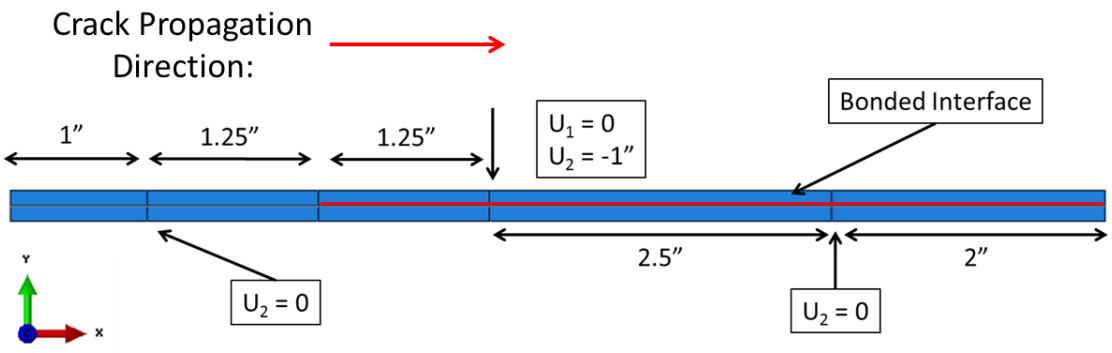

Figure 3-16: ENF FEA boundary conditions and dimensions

The master surface and slave surface were defined in the same manner as defined for mode I in Figure 3-11. An initial and maximum time increment size of 0.005 and a minimum increment size of 10^{-50} with a time period of 1 were used.

The modeled mode II response of the load versus displacement for the $[0]_{10}$ IM carbon/epoxy laminate are shown in Figure 3-17 for the predicted FEA solutions against the experimental data sets. Two FEA solutions were predicted. One solution used the critical SERR for mode II at onset. The second solution used the critical SERR for mode II at the maximum load. Both FEA solutions were stiffer than the experimental data for the linear region of the plot. However, the FEA model did not include the effects due to the 5 preloading calibrations denoted in Figure 3-7. These calibrations may have caused stiffness degradation in the test specimens.

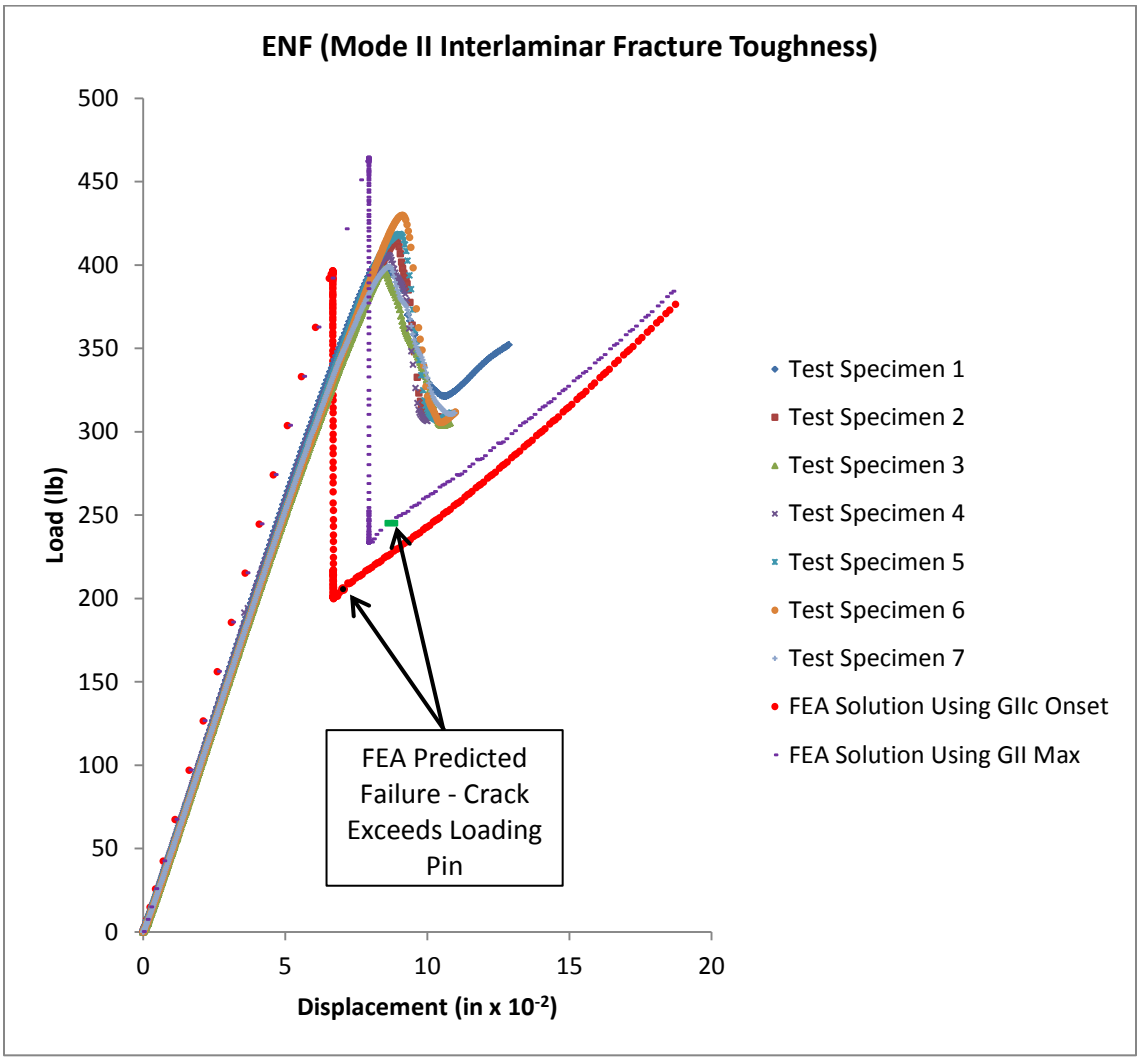

Figure 3-17: ENF load versus displacement response of $[0]_{10}$ IM carbon/epoxy laminate for FEA solutions and experimental data

3.3 Summary and Discussion of Experimental and Computational Results

Test results for the $[0]_{10}$ IM carbon/epoxy laminate show that G_{Ic} propagation is greater than G_{Ic} onset due to fiber bridging for mode I.

The predicted FEA response of mode I matched well with the experimental data. The boundary between the solution using G_{Ic} onset and G_{Ic} propagation accounted for most of the behavior experienced by the test specimens. However, visual fiber bridging, especially at the

crack tip was noted during experimentation. Excluding the behavior due to fiber bridging, the experimental load displacement response likely encompasses the boundaries between the solutions generated using G_{Ic} onset and G_{Ic} propagation.

Fiber bridging increases the stiffness-response of a material. R-curves for G_{Ic} onset and G_{Ic} propagation were generated to determine whether fiber bridging behavior was captured in Abaqus; fiber bridging behavior was not captured in Abaqus due to the step-function-like behavior noted in Figures 3-14 and 3-15.

The predicted FEA response of mode II was stiffer than the experimental data and the load drop prior to failure was steeper than the drop denoted in the experimental data. The FEA model did not include the effects due to the 5 preloading calibrations denoted in Figure 3-7. These calibrations may have caused stiffness degradation in the test specimens. If the initial slope of the predicted FEA solutions matched the average slope of the experimental data, and the FEA peak loads and failure loads remained the same, then the boundaries between the two predicted solutions would encompass all behavior experienced by the test specimens for mode II.

Chapter 4

Design of Experiments Using Numerical Simulations

In this chapter, a statistical sensitivity analysis (ANOVA) is used to vary parameters (also referred to as factors herein) suspected to influence the compression modulus, compression strength, and first ply failure of the UHM carbon/epoxy composite specimen using the FEA model developed in Chapter 2 for ASTM D6641 with C3D8I elements in the adhesive layer. The statistical sensitivity analysis and the rationale used to determine the levels for each factor are presented in Section 4.1. Section 4.2 discusses the results of the statistical sensitivity analysis.

4.1 Design of Experiments, Statistical Sensitivity Analysis

The requirements needed to perform a statistical sensitivity analysis are presented in Section 4.1.1 with the computed results. The orthogonal matrix used for the sensitivity analysis with its respective results is presented. The variance ratio, which is used to determine whether an objective function is sensitive to a factor, is calculated for each objective function listed in the orthogonal matrix. Section 4.1.2 discusses the factor and range of variation (level) used for the statistical sensitivity analysis.

4.1.1 Statistical Sensitivity Analysis

A statistical sensitivity analysis is performed using the previously developed finite element model in Chapter 2 for ASTM D6641 with C3D8I elements in the adhesive layer to determine the experimental test parameter(s) that most influences the predicted compressive

modulus, E_{xx} *(C)*, predicted compressive strength, S_{xx} *(C)*, and predicted first ply failure, FPF. The selection of parameters, is influenced from a previous work [8]:

> Such anomalies include the influence of tabs or adhesive bond lines of unequal thickness (resulting in loading eccentricities), fiber misalignment, nonuniform thickness along a tab, fixture fabrication inaccuracies, specimen machining errors, inaccurate specimen installation in the fixture, specimen/fixture/testing machine misalignments, etc. Such a sensitivity study may, in fact, be the principal factor in establishing a generally accepted standard.

The first step in developing a statistical sensitivity analysis is to determine the factors and their ranges of variation to be examined [23]. This step is subjective and is dependent on engineering judgment. The second step is to identify the analysis, finite element analysis in the present work, to be used which quantifies the selected factors. A factorial approach can be used to examine the total number of permutable combinations, 81 (three levels and four factors, 3^4) in this present work. However, the time required to compute 81 finite element analysis simulations can be quite large. In order to reduce the number of simulations, the orthogonal matrix method is used [21]. Each level of each factor appears the same number of times in an array for orthogonality. In the present work, the L_{18} (3^4) orthogonal matrix is chosen which defines 18 FEA simulations to be performed. The factors and associated levels for this present work are listed in Table 4-1; the selection of factors and their respective levels are further discussed in section 4.2.1.

Table 4-1: Statistical sensitivity analysis factors and levels in present work

Factors	Factor Description	Levels		
		1	2	3
A	Enforced Bolt Displacement (in)	7.71×10^{-4}	9.24×10^{-4}	3.20×10^{-4}
B	UHM Laminate Thickness (in)	1.165×10^{-1}	1.225×10^{-1}	1.105×10^{-1}
C	Adhesive Thickness (in)	1.30×10^{-2}	1.95×10^{-2}	8.67×10^{-3}
D	Fiber Misalignment (Laminate)	$[(0/\pm 60)_s]_2$	$[(0/55/-55)_s]_2$	$[(0/55/-65)_s]_2$

The relative magnitude of the factor effects is determined from the results presented in Table 4-2, which lists the averages of the objective functions, $E_{xx}(C)$, $S_{xx}(C)$, and FPF for each factor level.

Table 4-2: L_{18} (3^4) orthogonal matrix used in the statistical sensitivity analysis

Analysis Number	Levels				Objective Functions		
	Factor A	Factor B	Factor C	Factor D	E_{xx} (C) (Msi)	S_{xx} (C) (ksi)	FPF (ksi)
1	1	1	1	1	14.40	47.01	41.60
2	2	2	2	2	14.60	47.25	42.41
3	3	3	3	3	14.37	46.90	40.79
4	1	1	2	2	14.60	47.18	42.73
5	2	2	3	3	14.37	46.85	40.51
6	3	3	1	1	14.41	46.92	41.84
7	1	2	1	3	14.37	47.00	40.93
8	2	3	2	1	14.41	46.69	42.26
9	3	1	3	2	14.60	47.35	42.74
10	1	3	3	2	14.60	47.03	42.75
11	2	1	1	3	14.37	46.84	41.07
12	3	2	2	1	14.41	46.68	41.98
13	1	2	3	1	14.41	47.00	41.69
14	2	3	1	2	14.59	47.20	43.07
15	3	1	2	3	14.37	46.77	41.06
16	1	3	2	3	14.36	46.91	41.17
17	2	1	3	1	14.41	46.83	41.17
18	3	2	1	2	14.60	47.33	42.96
Overall Mean					14.46	46.99	41.82

A better metric for understanding the factor effects is by use of the decomposition of variance, commonly referred to as analysis of variance (ANOVA) [21]. The method used to compute the ANOVA makes use of the sum of squares technique. In this present work, the sum of squares is calculated as:

$$\eta = \eta_m + \eta_f + \eta_e \tag{76}$$

where,

η: total sum of squares
η_m: sum of squares due to mean
η_f: sum of squares due to factors

η_e: sum of squares due to error

The total sum of squares is equal to the sum of squares of the objective function values, column 6 of Table 4-3, Table 4-4, and Table 4-5 for all the analyses.

Table 4-3: Statistical sensitivity analysis of compressive modulus, E_{xx} *(C)*

Factor	Average E_{xx} *(C)* by Level (Msi)			Degree of Freedom	Sum of Squares $(Msi)^2$	Mean Square $(Msi)^2$	F ($F > 4$ is Significant)
	Level 1	Level 2	Level 3				
A	14.46	14.46	14.46	2	4.10×10^{-5}	2.05×10^{-5}	2.78
B	14.46	14.46	14.46	2	2.57×10^{-5}	1.28×10^{-5}	1.74
C	14.46	14.46	14.46	2	3.11×10^{-5}	1.56×10^{-5}	2.11
D	14.41	14.6	14.37	2	1.80×10^{-1}	9.01×10^{-2}	12,211
Error				9	6.64×10^{-5}	7.38×10^{-6}	
Total				17	1.80×10^{-1}	1.06×10^{-2}	

Table 4-4: Statistical sensitivity analysis of compressive strength, S_{xx} *(C)*

Factor	Average S_{xx} *(C)* by Level (ksi)			Degree of Freedom	Sum of Squares $(ksi)^2$	Mean Square $(ksi)^2$	F ($F > 4$ is Significant)
	Level 1	Level 2	Level 3				
A	47.02	46.94	46.99	2	1.91×10^{-2}	9.57×10^{-3}	0.75
B	47.00	47.02	46.94	2	1.90×10^{-2}	9.49×10^{-3}	0.74
C	47.05	46.91	46.99	2	5.63×10^{-2}	2.81×10^{-2}	2.2
D	46.86	47.22	46.88	2	5.09×10^{-1}	2.54×10^{-1}	19.92
Error				9	1.15×10^{-1}	1.28×10^{-2}	
Total				17	7.18×10^{-1}	4.23×10^{-2}	

Table 4-5: Statistical sensitivity analysis of FPF

Factor	Average FPF by Level (ksi)			Degree of Freedom	Sum of Squares $(ksi)^2$	Mean Square $(ksi)^2$	F ($F > 4$ is Significant)
	Level 1	Level 2	Level 3				
A	41.81	41.75	41.9	2	6.65×10^{-2}	3.32×10^{-2}	0.57
B	41.73	41.75	41.98	2	2.34×10^{-1}	1.17×10^{-1}	2
C	41.91	41.93	41.61	2	3.96×10^{-1}	1.98×10^{-1}	3.38
D	41.76	42.78	40.92	2	1.04 x 10	5.18	88.43
Error				9	5.28×10^{-1}	5.86×10^{-2}	
Total				17	1.16 x 10	6.82×10^{-1}	

The sum of squares due to the mean is the square of the mean of the objective function values multiplied by the number of analyses. The sum of squares due to factors is calculated using the following relation:

$$\eta_f = N(m_{f_1} - m)^2 + N(m_{f_2} - m)^2 + N(m_{f_3} - m)^2 + \cdots \quad (77)$$

where,

N: number of experiments at each level
m_{f_i}: mean of the objective function values by factor level
m: overall mean of the objective function

A sample calculation for the FPF objective function for the sum of squares due to Factor A, from Table 4-5, is:

$$\eta_f = 6(41.81 - 41.82)^2 + 6(41.75 - 41.82)^2 + 6(41.9 - 41.82)^2 = 6.65 \times 10^{-2} \quad (78)$$

A sample calculation for factor A, level 1, as listed in Table 4-5 is derived from the results shown in Table 4-2 and is given as:

$$m_{f_1} = \frac{41.6+42.73+40.93+42.75+41.69+41.17}{6} = 41.81 \quad (79)$$

The following relationship is used to determine the degrees of freedom within the matrix experiment:

$$DOF_{Tot} = DOF_{mean} + \sum DOF_{factor} + DOF_{error} \quad (80)$$

where,

DOF_{Tot}:	total degrees of freedom which is the number of analyses in this present work, 18
DOF_{Mean}:	degrees of freedom due to the mean, which is one in this present work
DOF_{factor}:	degrees of freedom due to factors which is the number of levels for that particular factor minus one
DOF_{error}:	degrees of freedom due to error

The following relation is used to calculate the mean square:

$$Mean\ square = \frac{\eta}{DOF} \quad (81)$$

The following relation is used to calculate the variance ratio, *F*:

$$F = \frac{Mean\ square_{factor}}{Mean\ square_{error}} \quad (82)$$

Values of *F* greater than four indicate that the objective function is sensitive to the factor [21, 28]. Factor D was the only factor to demonstrate a variance greater than four for the levels investigated. Factor D had a variance greater than four for all of the objective functions investigated in this study.

In certain instances, no degree of freedom may be left to estimate error variance and thus the error variance cannot be calculated. An approximate estimate of the error variance can be attained by pooling the sum of squares corresponding to the factors having the lowest mean

square. As a rule of thumb, Phadke [21] suggests that the sum of squares corresponding to the bottom half of factors (as defined by lower mean square) corresponding to about half of the degrees of freedom be used to estimate the error mean square or error variance. Phadke states that by the traditional statistical assumptions, pooling gives a biased estimate of error variance. To obtain a better estimate of error variance, a significantly larger number of experiments would be needed, the cost of which is usually not justifiable compared to the added benefit [21]. In the present work, the pooling of the sum of squares is not used since the degrees of freedom for the error is greater than one half of the total degrees of freedom. However, if the sum of squares corresponding to the factors having the lowest mean square is used, the same variance ratio values are still within their threshold ranges to be considered significant or insignificant for the factors analyzed in this study.

4.1.2 Factor and Level Determination

Four factors of interest and their corresponding levels, listed in Table 4-1, are chosen as the factors used in the orthogonal matrix in Table 4-2. Factors include the enforced bolt displacement, UHM laminate thickness, EA 9394 adhesive thickness, and fiber misalignment.

Equation (42) in Chapter 2, developed by Adams and Welsh [37], defines a relation between the clamping force per bolt and the applied torque. It is known that Adams was a lead-developer of the ASTM D6641 test fixture, which is why equation (42) is used as a benchmark. However, Shigley's machine design textbook [45] uses the bolt-torque relation:

$$T = KF_i d \tag{83}$$

where,

T:	bolt-torque
K:	torque coefficient, chosen as 0.2
F_i:	clamping force due to bolt tension (preload)
d:	bolt diameter

Using equation (83) with a torque value of 25 in-lb results in a preload of 500 lb and a displacement of 8.00 x 10^{-4} in, a substantial difference from the displacement of 1.54 x 10^{-3} in determined in Chapter 2 using equation (42). Due to potential operator error and torque wrench calibration inaccuracies, torque values for factor A are chosen as 20, 25, and 30 in-lb. Furthermore, the displacement value corresponding to 20 in-lb uses equation (83) and the displacement value corresponding to 30 in-lb uses equation (42) to generate a broader threshold.

The average and standard deviation for the thickness of the UHM carbon/epoxy composite specimen is typically not taken into account for ASTM D6641. However, these values were available from the SACMA SRM 1R-94 experimental data. The levels for factor B are chosen as the average and plus or minus one standard deviation of the SACMA SRM 1R-94 UHM laminate thickness, since the specimens are similar in geometry and are composed of the same material. The levels for factor C are chosen as the nominal adhesive thickness, 1.5 times the nominal thickness, and the nominal thickness divided by 1.5. The levels for factor D are the variation of stacking sequences of interest; the predicted moduli and strengths were determined to be statistically equivalent for the $[(0/\pm60)_s]_2$ and $[(+60/0/60)_s]_2$ laminates in Chapter 2. Therefore, the $[(0/\pm60)_s]_2$ laminate was chosen as a benchmark level and the $[(0/55/-55)_s]_2$ and $[(0/55/-65)_s]_2$ laminates were chosen as the other stacking sequences of interest.

4.2 Summary and Discussion

The laminate variations considered in factor D (Fiber misalignment) significantly affect results (i.e. calculated variance greater than four) for compression modulus, E_{xx} *(C)*, compression

strength, S_{xx} *(C)*, and first ply failure, FPF of the FEA model of ASTM D6641 with C3D8I elements in the adhesive layer as listed in Table 4-3, Table 4-4, and Table 4-5. The other factors investigated had a variance ratio less than 4; therefore, factors A (Enforced bolt displacement), B (UHM laminate thickness), and C (Adhesive thickness) do not significantly affect the FEA based results for E_{xx} *(C)*, S_{xx} *(C)*, and FPF.

The same statistical sensitivity analysis approach used in this chapter could be applied to examine parameters of interest for the SACMA SRM 1R-94 compressive modulus and compressive strength FEA models developed in Chapter 2 as well as the ASTM D5528 and ENF FEA models developed in Chapter 3.

Chapter 5

Conclusions and Recommendations

In this chapter, Section 5.1 discusses the conclusions from Chapters 2, 3, and 4. Section 5.2 discusses future experimental and modeling work based on the conclusions from section 5.1.

5.1 Conclusions

Based on the results of the previous investigations, the following conclusions are made:

- Test results for the two UHM angle-ply laminates $[(0/\pm60)_s]_2$ and $[(60/0/\text{-}60)_s]_2$ show that the moduli measured from both compression tests are statistically equivalent. Measured strengths are recorded to be significantly less for the $[(0/\pm60)_s]_2$ laminate than the $[(60/0/60)_s]_2$ laminate, as expected from previous studies.

- For the UHM SACMA SRM 1R-94 compressive modulus test specimens, the modeled end-crushing occurred at 2,210 με for both laminates investigated. Experimentally, the strain from 250 – 2000 με was used to determine the elastic modulus. Since the compressive modulus specimens are not to be loaded to failure, the chosen range of 250 – 2000 με was appropriate. Based on the compressive modulus model, the predicted SACMA SRM 1R-94 moduli of both UHM laminates were within a plus or minus one standard deviation span from the mean of the experimental data.

- For the SACMA SRM 1R-94 compressive strength specimen, the compressive strength was under-predicted for all adhesive response types. Approximately 30 % of the

SACMA SRM 1R-94 specimen load is transferred through the tabs when using the traction separation response, while the remaining 70% is transferred directly through the UHM laminate. The failure index for end-crushing indicated that end-crushing almost occurs at the same time as ULF. This implies that for the UHM laminates investigated, the initiation of end-crushing could occur. In addition, the predicted moduli of the $[(60/0/60)_s]_2$ laminate strength specimen was within one standard deviation of the respective compressive modulus specimen's experimental data.

- For the ASTM D6641 test specimens, the predicted modulus for the $[(60/0/\text{-}60)_s]_2$ laminate was within one standard deviation from the mean of the experimental data. The predicted modulus for the $[(0/\pm60)_s]_2$ laminate was within two standard deviations from the mean of the experimental data. The predicted strengths for the $[(60/0/\text{-}60)_s]_2$ laminate were under-predicted. The predicted compression modulus and strengths using a traction separation response, a continuum response, and C3D8I elements in the adhesive layer yielded statistically equivalent results for both laminates. The modeled FPF occurred in the outermost 0^o ply due to fiber compression at the gage section where the adhesive and the tab meet the UHM laminate for both specimens. The modeled ULF occurred in the 0^o ply due to Hashin fiber compression closest to the laminate center near the x-symmetry boundary condition specified in Figure 2-18.

- It was determined that approximately 78% of the ASTM D6641 load is transferred through the test fixture end, 12% of the load is transferred through the tab ends, and 10% of the load is transferred through the UHM laminate when using C3D8I elements in the adhesive layer. This means that 90% of the load is transferred via shear through the adhesive while the remaining 10% of the load is transferred directly through the UHM

laminate end load. This implies that during experimentation, assuming the tabs are flush with the UHM laminate and the test fixture, end-crushing is not likely to occur as a specimen failure mode.

- The largest ply (in local material coordinate system) compressive strains for both compression tests occur in the 0° plies for both laminates. The mean of the experimental SACMA SRM 1R-94 compressive strength specimen is 11.9 % greater than the experimental ASTM D6641 strength for the $[(60/0/60)_s]_2$ laminate. Notable differences between the two test standards, aside from loading methods (Shear and end), are the tab to gage section ratios and the clamping pressure due to bolt torque. The SACMA SRM 1R-94 predicted strength using FEA is greater than the strength predicted by ASTM D6641 possibly due to a longer unsupported gage length.

- For mode I, test results for the $[0]_{10}$ IM carbon/epoxy laminate show that G_{Ic} propagation is greater than G_{Ic} onset due to fiber bridging.

- For ASTM D5528, the predicted FEA response of mode I matched well with the experimental data. The boundary between the solution using G_{Ic} onset and G_{Ic} propagation accounted for most of the behavior experienced by the test specimens. However, visual fiber bridging, especially at the crack tip was noted during experimentation.

- Fiber bridging increases the stiffness-response of a material. R-curves for G_{Ic} onset and G_{Ic} propagation were generated for the $[0]_{10}$ IM carbon/epoxy laminate to determine

whether fiber bridging behavior was captured in Abaqus; fiber bridging behavior was not captured in Abaqus due to the step-function-like behavior noted in Figures 3-14 and 3-15.

- For the ENF test, the predicted FEA response of mode II was stiffer than the experimental data and the load drop prior to failure was steeper than the drop indicted by the experimental data. The FEA model did not include the effects due to the 5 preloading calibrations denoted in Figure 3-7. These calibrations may have caused stiffness degradation in the test specimens. If the initial slope of the predicted FEA solutions matched the average slope of the experimental data, and the FEA peak loads and failure loads remained the same, then the boundaries between the two predicted solutions would encompass all behavior experienced by the test specimens for mode II.

- For the computational design of experiments approach, factor D, the fiber misalignment, significantly affected (i.e. calculated variance greater than four) the UHM laminate compression modulus, E_{xx} *(C)*, compression strength, S_{xx} *(C)*, and first ply failure, FPF predicted by the ASTM D6641 FEA model with C3D8I elements in the adhesive layer as shown in Table 4-3, Table 4-4, and Table 4-5. The other factors investigated had a variance ratio less than 4; therefore, factors A (Enforced bolt displacement), B (UHM laminate thickness), and C (Adhesive thickness) do not significantly affect the FEA predicted results for E_{xx} *(C)*, S_{xx} *(C)*, and FPF.

5.2 Future Work

Future work should focus on experimental and computational aspects for SACMA SRM 1R-94, ASTM D6641, ASTM D5528, and the ENF tests.

A model that better captures the behavior of ASTM D6641 and SACMA SRM 1R-94 should be developed by individually modeling each ply within a laminate. The VCCT method should be used to define surfaces at every interface including the tabs and adhesive layers. Ply failure and damage evolution should be incorporated using SC8R elements for each ply. Such an approach is computationally expensive, but feasible using the techniques presented in Chapters 2 and 3. This approach would show the status of whether an interface is bonded or debonded as opposed to using a 'cohesive' approach which would require a visual inspection of the graphical user interface. Furthermore, stiffness degradation was noted before ply failure in the experimental specimens, based on the point-by-point change in modulus. The onset of matrix microcracking may have induced the non-linear behavior. For future modeling, stress-strain curves should be evaluated to determine when onset of matrix microcracking initiates which would lead to softening of the laminate. This behavior could be incorporated into a model by writing a user material subroutine in Abaqus that applies material softening behavior. A non-linear material model with appropriate failure and damage evolution criteria should be defined for the adhesive in order to better characterize EA 9394's stress versus strain response. A sensitivity assessment should be conducted to determine the effect, if any, on the stress versus strain response after damage initiation for $G_{ft,c}$ and $G_{fc,c}$ defined in Section 2.2.2.1. If the stress versus strain response after damage initiation is determined to be sensitive to variations in $G_{ft,c}$ and $G_{fc,c}$, then experimental compact tension and compact compression tests should be carried out on the UHM carbon/epoxy material system.

Experimentally, strain gages now exist such as one made by Vishay Precision Group [46], that are small enough to fit in the SACMA SRM 1R-94 test fixture for strength specimens. The dimensions listed in reference [46] are 0.042 in (Overall length) by 0.140 in (Overall width). If test data can be proven to be reliable using such a small strain gage, then these strain gages may allow the use of only one specimen type for SACMA SRM 1R-94. Furthermore, the same strain

gage could be used for ASTM D6641, and tapered tabs could extend further into the gage section, reducing stress concentrations at the adhesive-laminate interface, without substantially decreasing the effective unsupported length of the specimen, which would reduce the possibility of inducing specimen buckling.

The model developed in Chapter 2 for the SACMA SRM 1R-94 strength specimen suggests that end-crushing could occur in the 0° plies for the laminates investigated. UHM laminates with 0° plies tested using SACMA SRM 1R-94 should be interpreted with caution. The correct span of the stress-strain curve should be chosen such that stiffness degradation due to end-crushing damage is not included in the modulus calculation. The commonly used 0.1-0.3% strain range may not be an appropriate range for UHM laminates containing 0° outer plies. Further investigation is warranted.

For the model of ASTM D5528, cohesive surfaces and cohesive elements could be used to benchmark the response of the VCCT solution. A superposition model, as described in [47], could be used with cohesive elements or cohesive surfaces to incorporate fiber bridging effects.

For the ENF test, a model could be developed to examine the damage accumulation effects, if any, from the 5 preload calibrations in the experiment. Incorporating the damage accumulation may cause stiffness degradation when the model is loaded to failure such that the initial slope, as seen in Figure 3-17, more closely matches the average initial slope of the test specimens. Furthermore, the effects due to friction along the contact interfaces at the loading nose and both supports for the ENF model, if any, should be further investigated.

References

[1] Bunsell, Anthony Roland, ed. *Handbook of tensile properties of textile and technical fibres*. Elsevier, 2009.

[2] Baral, N., P. Davies, C. Baley, and B. Bigourdan. 2008. "Delamination behaviour of very high modulus carbon/epoxy marine composites," *Composites Science and Technology*, *68* (3): 995-1007.

[3] Pinho, S. T., R. Darvizeh, P. Robinson, C. Schuecker, and P. P. Camanho. 2012. "Material and structural response of polymer-matrix fibre-reinforced composites," *Journal of Composite Materials*, 46 (19-20): 2313-2341.

[4] Daniel, Isaac M., et al. *Engineering mechanics of composite materials*. Vol. 3. New York: Oxford university press, 1994.

[5] Hashin, Z., "Failure criteria for unidirectional fiber composites," *Journal of Applied Mechanics*, vol. 47, pp. 329–334, 1980

[6] Hashin, Z., and A. Rotem, "A fatigue criterion for fiber-reinforced materials," *Journal of Composite Materials*, vol. 7, pp. 448–464, 1973.

[7] Tsai, S. W. and Wu, E. M. (1971). "A general theory of strength for anisotropic materials," *Journal of Composite Materials*. vol. 5, pp. 58–80

[8] Chaterjee, S., D. Adams, and D. W. Oplinger. June 1993. “Test Methods for Composites a Status Report, Volume II: Compression Test Methods,” Department of Transportation and Federal Aviation Association, DOT/FAA/CT-92/17.

[9] Lackey, E. Spring 2009. “Identification, Selection, and Development of Composite Test Standards – A Case Study from the Development of a Design Standard for Composites,” The University of Mississippi. Web. 20 Aug. 2012. http://speautomotive.com/SPEA_CD/SPEA2009/pdf/VPT/VPT-08.pdf

[10] Xie, M., and D. Adams. 1995. “Effect of loading method on compression testing of composite materials,” *Journal of Composite Materials*, 29 (12): 1581-1600.

[11] Adams, Donald. *Testing Tech: Why Standardization? :* Composites World, 1 May 2007. Web. 04 Apr. 2014. http://www.compositesworld.com/articles/testing-tech-why-standardization

[12] Miracle, Daniel B., Steven L. Donaldson, and George F. Vander Voort. *ASM handbook.* ASM International (2001), Materials Park, OH

[13] Joyce, Peter J., Melanie G. Violette, and Tess J. Moon, 2002, "Finite element analysis of unidirectional composite compression test specimens: A parametric study." ASTM Special Technical Publication 1416: 30-68. West Conshohocken, PA.

[14] Adams, Donald F., 2002, "Tabbed versus untabbed fiber-reinforced composite compression specimens." ASTM Special Technical Publication 1416: 3-16. West Conshohocken, PA.

[15] ASTM D3410 – 08, *Standard Test Method for Compressive Properties of Polymer Matrix Composite Materials with Unsupported Gage Section by Shear Loading 1.* ASTM International, West Conshohocken, PA.

[16] ASTM D5528 – 02, *Standard Test Method for Mode I Interlaminar Fracture Toughness of Unidirectional Fiber-Reinforced Polymer Matrix Composites1.* ASTM International, West Conshohocken, PA.

[17] Turon, Albert, et al. "An engineering solution for mesh size effects in the simulation of delamination using cohesive zone models." *Engineering Fracture Mechanics* 74.10 (2007): 1665-1682.

[18] Xie, De, and Anthony M. Waas. "Discrete cohesive zone model for mixed-mode fracture using finite element analysis." *Engineering Fracture Mechanics* 73.13 (2006): 1783-1796.

[19] Camanho, Pedro Ponces, C. G. Davila, and M. F. De Moura. "Numerical simulation of mixed-mode progressive delamination in composite materials." *Journal of Composite Materials* 37.16 (2003): 1415-1438.

[20] Bonhomme, J., et al. "Computational models for mode I composite fracture failure: the virtual crack closure technique versus the two-step extension method." *Meccanica* 45.3 (2010): 297-304.

[21] Phadke, Madhav S. 1989. *Quality Engineering Using Robust Design*, Prentice Hall

[22] Grujicic, M., and K. M. Chittajallu. "Optimization of the cathode geometry in polymer electrolyte membrane (PEM) fuel cells." *Chemical Engineering Science* 59.24 (2004): 5883-5895.

[23] Grujicic, M., B. Pandurangan, D. C. Angstadt, K. L. Koudela and B. A. Cheeseman. 2007. "Ballistic-performance optimization of a hybrid carbon-nanotube/e-glass reinforced poly-vinyl-ester-epoxy-matrix composite armor," *Journal of Materials Science*, 42 (14): 5347-5359.

[24] Dar, Fazilat H., Judith R. Meakin, and Richard M. Aspden. "Statistical methods in finite element analysis." *Journal of Biomechanics* 35.9 (2002): 1155-1161.

[25] Nader, Jacques W., Dagher, H. J., El Chiti, F., & Lopez-Anido, R. "Probabilistic finite element analysis of ASTM D6641 compression test for marine grade polymer matrix composites." *Journal of Reinforced Plastics and Composites* 28.8 (2009): 897-911.

[26] *Wyoming*. Web. 17 June 2013. http://www.wyomingtestfixtures.com/

[27] Makeev, A. February 26, 2013. "Advanced Materials Technology," VLC/NRTC Year-End Review Presentation, Moffett Field, CA, WBS #: 2012-B-12-T6.1-A10.

[28] ASTM Standard D6641/D 6641M – 09, 2008. *"Standard Test Method for Compressive Properties of Polymer Matrix Composite Materials Using a Combined Loading Compression (CLC) Test Fixture,"* ASTM International, West Conshohocken, PA.

[29] SACMA SRM 1R-94, 1994. *"Compressive Properties of Oriented Fiber-Resin Composites,"* Suppliers of Advanced Composite Materials Association.

[30] Glath, M., Koudela, K., Strauch, E., September 10, 2013. "Compression Behavior of Ultra-High Modulus Carbon/Epoxy Composites," 2013 American Society for Composites (ASC): 28th Technical Conference, Destech Publications, Inc., University Park, PA.

[31] Lapczyk, Ireneusz, and Juan A. Hurtado. "Progressive damage modeling in fiber-reinforced materials." *Composites Part A: Applied Science and Manufacturing* 38.11 (2007): 2333-2341.

[32] "ABAQUS 6.12 User Documentation" Simulia. Web. 02 Dec. 2013.

[33] Camanho, Pedro M. "*Progressive Failure Analysis of Advanced Composites*," Document Reference: FR-FA8655-06-1-3072, Porto University (Portugal) Department of Mechanical Engineering, 2008.

[34] Pinho S.T., Robinson P., Iannucci L., “Fracture toughness of the tensile and compressive fibre failure modes in laminated composites,” *Composites Science and Technology*, 2006; 66: 2069-2079

[35] Maimi P., Camanho P.P., Mayugo J.A., Davila C.G., “A continuum damage model for composite laminates: Part II – Computational implementation and validation”, *Mechanics of Materials*, 2007; 39: 909-919

[36] Pinho, Silvestre T., Paul Robinson, and Lorenzo Iannucci. "Fracture toughness of the tensile and compressive fibre failure modes in laminated composites." *Composites Science and Technology* 66.13 (2006): 2069-2079.

[37] Adams, D., and J. S. Welsh. 1997. "The Wyoming Combined Loading Compression (CLC) Test Method," *Journal of Composites Technology & Research*, 19 (3): 123-133.

[38] Camanho, P. P., and C. G. Davila, “Mixed-Mode Decohesion Finite Elements for the Simulation of Delamination in Composite Materials,” NASA/TM-2002–211737, pp. 1–37, 2002

[39] Wikipedia. 2014. “Fracture Mechanics,” Web. 15 Feb. 2014. http://en.wikipedia.org/wiki/Fracture_mechanics#Griffith.27s_criterion_2

[40] *Test Resources*. Tech. Web. 28 March 2014 . http://www.testresources.net/media/reviews/photos/original/4a/71/3e/astm-d5528-dcb32.jpg

[41] U.S. Government end-notched flexure report

[42] Johnson, W. Steven, and P. D. Mangalgiri. *Investigation of Fiber Bridging in Double Cantilever Beam Specimens*. No. NASA-TM-87716. National Aeronautics and Space Administration Hampton Va Langley Research Center, 1986.

[43] Barbero, Ever J. *Finite element analysis of composite materials using Abaqus*. CRC press, 2013.

[44] Sun, C. T., and Z.-H Jin. *Fracture Mechanics*. Waltham, MA: Academic, 2012. Print.

[45] Shigley, Joseph Edward. *Shigley's mechanical engineering design*. Tata McGraw-Hill Education, 2011.

[46] Vishay Precision Group. 2014. "General Purpose Strain Gages – Linear Pattern," Web. 31 March 2014. http://www.vishaypg.com/docs/11073/031ec.pdf

[47] Chiminelli, A., et al. "Application of cohesive element simulation techniques to model delamination and fiber-bridging in composite materials." *Anales De Mecánica De La Fractura* 2 (2011): 523-27.

Appendix A

Matlab Code: Modulus Calculation

Classical laminate theory was used to calculate the compression modulus of the UHM $[(0/\pm60)_s]_2$ and $[(60/0/60)_S]_2$ laminates using the property inputs listed in Tables A-1 and A-2.

Table A-1: Excel input file for $[(0/\pm60)_s]_2$ laminate

Ply ID Number	Ply Angle (Deg)	E1 (psi)	E2 (psi)	Nu12	G12 (psi)	Thickness (in)
1	0	40390000	922000	0.303	818000	0.009708333
2	60	40390000	922000	0.303	818000	0.009708333
3	-60	40390000	922000	0.303	818000	0.009708333
4	-60	40390000	922000	0.303	818000	0.009708333
5	60	40390000	922000	0.303	818000	0.009708333
6	0	40390000	922000	0.303	818000	0.009708333
7	0	40390000	922000	0.303	818000	0.009708333
8	60	40390000	922000	0.303	818000	0.009708333
9	-60	40390000	922000	0.303	818000	0.009708333
10	-60	40390000	922000	0.303	818000	0.009708333
11	60	40390000	922000	0.303	818000	0.009708333
12	0	40390000	922000	0.303	818000	0.009708333

Table A-2: Excel input file for $[(60/0/-60)_S]_2$ laminate

Ply ID Number	Ply Angle (Deg)	E1 (psi)	E2 (psi)	Nu12	G12 (psi)	Thickness (in)	Material
1	60	40390000	922000	0.303	818000	0.009708333	c/ep
2	0	40390000	922000	0.303	818000	0.009708333	c/ep
3	-60	40390000	922000	0.303	818000	0.009708333	c/ep
4	-60	40390000	922000	0.303	818000	0.009708333	c/ep
5	0	40390000	922000	0.303	818000	0.009708333	c/ep
6	60	40390000	922000	0.303	818000	0.009708333	c/ep
7	60	40390000	922000	0.303	818000	0.009708333	c/ep
8	0	40390000	922000	0.303	818000	0.009708333	c/ep
9	-60	40390000	922000	0.303	818000	0.009708333	c/ep
10	-60	40390000	922000	0.303	818000	0.009708333	c/ep
11	0	40390000	922000	0.303	818000	0.009708333	c/ep
12	60	40390000	922000	0.303	818000	0.009708333	c/ep

The Matlab code used to calculate the modulus of both laminates is listed below:

```
A = xlsread('Modulus_Calculation');%Import Excel File
B=A(:,7);%Thickness Column
C=[0;B]; tavg=sum(C)/2; yprevious=0;
n=size(C,1);
i=1;
for i=1:n
ynew=C(i)+yprevious; yprevious=ynew;
z=ynew-tavg; Z(:,i)=z;
G=[i, z];
end
R=[1,0,0;0,1,0;0,0,2]; %Residual matrix
E=A(:,2);%Ply Layup
M=size(E,1);
AMatrixprevious=0; BMatrixprevious=0; DMatrixprevious=0;
for i=1:M
theta=E(i)*(pi/180);
m=cos(theta); n=sin(theta);
T=[m*m,n*n,2*m*n;n*n,m*m,-2*m*n;-m*n,m*n,m*m-n*n];
s=[1/A(i,3),-A(i,5)/A(i,3),0;-A(i,5)/A(i,3),1/A(i,4),0;0,0,1/A(i,6)];
S(:,:,i)=s; Sbar=R*T^-1*R^-1*s*T; SBAR(:,:,i)=Sbar;
q=s^-1; Q(:,:,i)=q; Qbar=T^-1*q*R*T*R^-1; QBAR(:,:,i)=Qbar;
end
M=size(E,1);
AMatrixprevious=0; BMatrixprevious=0; DMatrixprevious=0;
for i=1:M
AMatrix=QBAR(:,:,i)*(Z(i+1)-Z(i))+ AMatrixprevious; AMatrixprevious=AMatrix;
BMatrix=0.5*QBAR(:,:,i)*((Z(i+1))^2-(Z(i))^2)+BMatrixprevious; BMatrixprevious=BMatrix;
DMatrix=0.333333*QBAR(:,:,i)*((Z(i+1))^3-(Z(i))^3)+DMatrixprevious;
DMatrixprevious=DMatrix;
end
ABDMatrix=[AMatrixprevious,BMatrixprevious;BMatrixprevious,DMatrixprevious];
abcdMatrix=ABDMatrix^-1;
Ex=1/(abcdMatrix(1,1)*sum(C));
disp('Ex (psi)');
fprintf('%3.4e \n', Ex);
```

Appendix B

Non-Technical Abstract

The compression strength of carbon fiber composites can be considerably lower than the tensile strength. In this study, two compression test methods, SACMA SRM 1R-94 and ASTM D6641, were used to determine the compression strength and compression modulus of two ultra-high modulus (UHM, >350 GPa) carbon/epoxy laminates. One laminate had a 60° outer ply and the other had a 0° outer ply. The moduli of both laminates were experimentally shown to be statistically equivalent while the strength was shown to be significantly less for the laminate with a 0° outer ply. A finite element model was developed to predict the ways each test specimen fails for both compression test methods. Predicted stress versus strain curves were generated from the finite element model and correlated relatively well with the experimental data. Failure was underpredicted for the laminate with the 60° outer ply and overpredicted for the laminate with the 0° outer ply.

Fracture toughness is a resistance to crack growth. Two test methods, ASTM D5528 and a proprietary end-notched flexure test, were used to experimentally determine the fracture toughness of a laminate consisting of 10 plies all oriented at 0°. A finite element model was developed for each fracture toughness test method. A boundary was developed for the modeled load-displacement plot to encompass the experimental behavior of the test specimens for both test methods. The predicted boundary agreed well with experimental data from the ASTM D5528 test specimens. The predicted load-displacement response of the proprietary end-notched flexure test demonstrated stiffer behavior than the experimental data.

A statistical sensitivity analysis (ANOVA), based on the previously developed finite element model of ASTM D6641, was used to vary parameters assumed to influence the compression modulus, compression strength, and first ply failure of ASTM D6641. Of the

chosen parameters, fiber misalignment was predicted to significantly affect the results, based on the finite element data, of the compression modulus, compression strength, and first ply failure for the chosen levels of variation. The laminate thickness, adhesive thickness, and enforced bolt displacement were predicted to not significantly affect the results, based on the finite element data, of the compression modulus, compression strength, and first ply failure for the chosen levels of variation.